



Norwegian University of
Science and Technology

Investigation of Raman scattering phenomena in the development of mid-IR ultra-short laser pulses

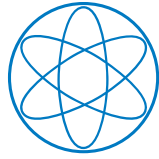
Roland Axel Richter

MSc in Physics

Submission date: December 2015

Supervisor: Irina T Sorokina, IFY

Norwegian University of Science and Technology
Department of Physics



Technische Universität München
Fakultät für Physik
Norges teknisk-naturvitenskapelige universitet
Fakultet for naturvitenskap og teknologi
Institutt for fysikk

Master thesis in the master course of physics

Nonlinear phenomena in ultra-short, mid-infrared laser pulses in optical glass fibers

Richter, Roland

Trondheim, Dec 2015

Contents

1 Abstract	1
2 Introduction	3
2.1 Objectives	3
3 Literature overview	5
3.1 Raman scattering	5
3.1.1 Raman scattering in fibers	5
3.2 Simulation and generation of a supercontinuum in fibers	6
4 Theory	7
4.1 Nonlinear pulse propagation in fibers	7
4.1.1 Basic mathematic	7
4.1.2 The generalized nonlinear schrödinger equation (GNLSE)	9
4.1.3 Dispersion	11
4.1.4 Self-phase modulation	13
4.1.5 Solitons	15
4.1.6 Four-Wave Mixing (FWM)	16
4.1.7 Raman Scattering	17
4.2 Numerical simulation methods	25
4.2.1 ODE-solving	25
4.2.2 Split-Step solving approach	26
4.3 Summary	28
5 Experimental Setup	29
5.1 Raman spectrometer	29
5.1.1 Redesign of the used hardware	30
5.1.2 Redesign of the used software	32
5.1.3 Scattering geometries	35
5.1.4 Calibration	36
5.1.5 Test measurements	37
5.2 Automatisatation of the dispersion measurement setup	40
5.2.1 Setup	40
5.2.2 Calculation of the dispersion	41

5.3	Summary	42
6	Practical applications and results	43
6.1	Measurement of the dispersion of a fiber	43
6.2	Measurement of the Raman shift in a fiber	44
6.2.1	Calculation of the Raman response function of the silica fiber	48
6.2.2	Calculation of the Raman response function of the germanate fiber	53
6.3	Fiber simulations	54
6.3.1	Simulation program	54
6.3.2	Fiber simulations	56
6.3.3	Comparison of the simulation results with the measured data	59
6.3.4	Comparison of both solving approaches (ODE and SSFM)	61
6.4	Summary	62
7	Design of a laser using SPM	63
7.1	Packaging of the laser	67
7.2	Summary	67
8	Summary	69
A	Appendix	73
A.1	Code Listing	73
A.1.1	Python script for solving the GNLSE	73
A.1.2	Code for the controller boards	73
A.1.3	Controller program - GUI	73
A.1.4	Controller program - remote	73
A.1.5	Controller for the dispersion setup	73
A.2	Circuits	74
A.2.1	Cape, Ver. I	74
A.2.2	Cape, Ver. III	75
A.2.3	Stepper Controller, Ver. I	78
A.2.4	Amplifier, Ver. I	81
A.3	Case requirements	84
A.4	Data sheets	85
A.4.1	Spectrometer 14018	85
A.4.2	Photo multiplier C31034	90
A.5	Design of the case for the laser described in chapter 7	94
A.5.1	Requirements for the case	94
A.5.2	General module description	94
A.5.3	First design	94

A.6 Assembled model	96
A.6.1 Heat- and airflow calculation	97
A.6.2 Improvements of the package	113
A.6.3 Further build options	117
A.7 Derivation of the differential equation for the thermic network	118
A.7.1 General calculation	118
A.7.2 Steady state calculation	119
A.7.3 Derivation of the thermic formula	120
A.7.4 Derivation of heat flow from the inside to the outside of a fiber	121
A.7.5 Increasing the thermal situation for the coupler mount	123
A.7.6 Derivation of basic pressure difference function	128
A.7.7 Calculation of the air flow velocity	128
A.8 Spectra	130
A.8.1 Supercontinuum spectrum, measurement	130
A.9 Images	131
A.9.1 Cape I	131
A.9.2 Original ISA card	131
Bibliography	133
Acknowledgements	147

List of Figures

4.1	Fiber schematic	12
4.2	Frequency shift for a sech-pulse, function from eq. (4.49)	15
4.3	Comparison of Raman spectra between glass and crystals, [38]	19
4.4	Processes in Raman scattering shown as Feynman diagram, [39]	21
4.5	Comparison of the different Raman approximation functions	24
5.1	Spectrometer scheme	29
5.2	Main part of the control cape	31
5.3	Basic structure of the control program. The symbols used in this figure are explained in table 5.1	33
5.4	Used scattering geometries	35
5.5	Laser guidance optics	36
5.6	Fluorescence test measurement with GSGG:Cr	37
5.7	Raman measurement on diamond substrate, full spectrum	38
5.8	Raman measurement on diamond substrate, small spectrum	39
5.9	Raman measurement on silicon	40
5.10	Schematic of the dispersion measurement setup [57]	41
6.1	Position curves of the interference pattern of the dispersion setup	43
6.2	Measured and fitted data for the dispersion curve measurement	44
6.3	Proof of concept of the dispersion measurement setup	45
6.4	Raman gain of a silica fiber	46
6.5	Comparison of the Raman scattering in a silica fiber vs the Raman scattering in silica glass	47
6.6	Raman gain of a germanate fiber	48
6.7	Raman gain of a silica and germanate fiber in comparison	49
6.8	Comparison of fitted data of the Raman gain of a silica fiber vs the original data	50
6.9	Comparison of fitted data of the Raman gain of a silica fiber vs. the original data without the Rayleigh peak	51
6.10	Calculated Raman response in comparison with an approximative formula	52
6.11	Raman gain of a germanate fiber, processed	53

6.12	Calculated Raman response in comparison with an approximative formula	54
6.13	Blow-Wood-function, implemented in python	55
6.14	Formula for calculating the right hand side of the equation 4.85, written in python	56
6.15	Simple soliton calculation	57
6.16	Raman shift of a soliton	57
6.17	Comparison of the influence of different β -values towards the supercontinuum in a fiber	58
6.18	Comparison of the influence of different n_2 -values towards the supercontinuum in a fiber	59
6.19	Comparison of the simulation results using the β -values from table 6.3	61
7.1	Basic layout of the laser, including distances in [mm]. Description of the parts is in table 7.1	63
7.2	Pulse spectrum of laser L1	65
7.3	Pulse spectrum of laser L2 and L3	65
7.4	Pulse spectrum of the whole fiber laser	66
A.1	3D-model of the designed laser case, I. generation, without cover . .	97
A.2	Air flow in the laser case for the first generation	98
A.3	Simplified thermic resistor network for the laser assembly	101
A.4	Simplified air flow network for the laser assembly, symbol explanations in table A.6	108
A.5	Proposal for an improved build for the laser packaging, view including the laser compartment	114
A.6	Laser module assembly for the packaging, 2 nd generation	115
A.7	Proposal for an improved build for the laser packaging, view including the electronic compartment	116
A.8	3d-model of the laser packaging, 2 nd generation, including the electronic compartment	117
A.9	Replacement circuit for simple thermal problem	119
A.10	Replacement circuit for simple thermal problem in steady state . . .	120
A.11	Replacement circuit for coupler mount with attached fins	123
A.12	Transported energy per time in dependance of the air flow	125
A.13	Temperature difference of the radiator in comparison with the air flow	126
A.14	Replacement circuit for coupler mount with attached radiator . . .	127
A.15	Supercontinuum measurement of different fibers	130
A.16	Cape I, mounted onto the BeagleBone Black	131
A.17	Originally used ISA card	132

Chapter 1

Abstract

In this thesis several different nonlinear phenomena were examined, such as the Raman scattering of light in fibers and solid bodies and the nonlinear dispersion of fibers. Furthermore the influence of different parameters such as the dispersion coefficients β_i and the pulse intensity was examined. In order to measure both the Raman response and the dispersion of materials, two new setups had to be designed, programmed and tested. Finally the obtained data was used for testing an existing fiber laser which uses the self-phase-modulation-effect to obtain shorter pulse lengths. Furthermore a packaging for this laser was designed and calculated.

Chapter 2

Introduction

Since the development of the laser in 1960 many new application methods have been developed. Among others scientists discovered that light not only generates linear effects in materials, but also nonlinear effects. The importance of those nonlinear effects increases with every year, and with it the broadness of their possible applications. Nonlinear effects can not only be used in fibers necessary for data transport, the nutriment of today's world, but also for example in illumination applications, for range finding, for detection systems and many options more. In order to improve the understanding of those nonlinear effects this thesis provides an overlook over two main nonlinear effects which are already used in real-world applications, and furthermore names several other nonlinear effects.

2.1 Objectives

The goals in this thesis can be divided up into three main parts. One task was it to automate and improve a setup used for measuring the dispersion of fibers, such that it can be remotely operated. The second task was to reequip an existing Raman spectrometer with the necessary control and measurement instruments in order to be able to measure the Raman signal both from fibers and bulk materials in two different scattering configurations. Furthermore this setup should also be remotely operable designed. With the second setup several fibers and bulk materials should be measured afterwards in order to prove the functionality of the setup and to get new data useful for future research.

The results of the measurements of both setups should be afterwards used to calculate the influence of several different nonlinear phenomena onto a pulse propagating through a fiber, and compare the results of the calculation with the result of former experiments. For this a simulation program should be designed, in order to calculate the GNLSE while taking the influence of all parameters into account.

Chapter 3

Literature overview

In this chapter an overview of the literature covering the nonlinear optics phenomena as far as it relates to supercontinuum generation both in simulations and in real experiments will be provided, and furthermore an overview of the literature covering the Raman scattering phenomena both in general and a second deeper look at the Raman scattering in fibers.

3.1 Raman scattering

One of the first theories towards light scattering (brillouin scattering) was created already in 1922 by Brillouin [1] predicting the inelastic scattering of light by long wavelength sound waves. One year later Smekal developed the theory of light scattering by a system of quantized energy levels [2] which already contained the characteristics of the phenomena discovered later by Raman [3]. But due to the relatively small scattering cross section the research in that field did not spread until the development of the first laser. In 1962 Porto and Wood used a ruby laser for measuring the Raman spectrum of CCL_4 and C_6H_6 [4]. Since that as one of the first measurements the Raman research field drastically increased due to the increasing amount of different lasers resulting in a large amount of different excitation methods.

3.1.1 Raman scattering in fibers

Two of the most important nonlinear processes happening in fibers are self-phase-modulation [5] and stimulated Raman scattering [6]. While the self-phase-modulation is used in ultra-short-pulse-lasers by pulse compression [7], is the stimulated Raman scattering mostly used for both frequency shifting of incoming pulses [8] and supercontinuum generation [9][10]. Nevertheless it also competes with the self-phase modulation (SPM), and furthermore limits the maximum power in the fiber. Due to the material properties the Raman response in the fiber looks quite similar to glass, which will be covered in 4.1.7.

3.2 Simulation and generation of a supercontinuum in fibers

When short narrow-band laser pulses enter a nonlinear optical medium, they may experience spectral broadening and convert into a broadband output, a process known as supercontinuum generation. The first supercontinuum experiments in optical fibers were done by (inter alia) Lin and Stolen [11] who produced a supercontinuum over a spectral range of $\approx 200\text{THz}$ in a standard silica-based fiber. This effect was attributed to cascaded stimulated Raman scattering (IRS, refer to section 4.1.7) and self-phase modulation (SPM, refer to section 4.1.4). These studies clarified the importance of the mutual interaction between Raman scattering, self-phase modulation as well as the role of cross-phase modulation and various four-wave-mixing (FWM, refer to section 4.1.6) processes. These processes lead also to a merge of discrete generated frequencies to produce a smooth spectral output [12]. This broadening mentioned above was observed for the case of normal GVD pumping. When pumping in the anomalous GVD regime spectral broadening arises from soliton-related dynamics. The possibility of soliton propagation in the anomalous GVD regime was first suggested by [13] in 1973 by analysing the nonlinear Schrödinger Equation (NLSE), but the lack of ultrashort pulses at wavelengths $> 1.3\mu\text{m}$ made the verification of this thesis impossible until 1980, when [14] used $\approx 7\text{ps}$ -pulses with a wavelength at around $1.55\mu\text{m}$ to excite both a non-broadening stable fundamental soliton and higher-order solitons. These higher-order solitons are according to [15] and [16] a particular solution of the NLSE representing a bound state of N fundamental solitons. By now, the comparison between experiments and numerical simulations based not only on the NLSE as mentioned above, but also on the generalized nonlinear Schrödinger equation (GNLSE) opened the way to a better understanding of the physical background of the supercontinuum generation, as stated in [17]. As a result a good agreement can be observed between experiments and simulations in selected cases, such as the single-mode pulse propagation in silica fibers, which is good enough for this thesis.

Chapter 4

Theory

4.1 Nonlinear pulse propagation in fibers

In this section the mathematics of a pulse both moving in a fiber and a crystal shall be covered. While in the first section 4.1.1 the basics will be covered and the general formula will be derived, the following sections will be used to take a deeper look into several specific phenomena which happen both in the linear and the non-linear regime in the material.

4.1.1 Basic mathematic

In order to model any classical electrodynamical phenomenon one has to start with Maxwell's equations. These are

$$\nabla \times \mathbf{E} = -\frac{\partial \mathbf{B}}{\partial t} \quad (4.1)$$

$$\nabla \times \mathbf{H} = \mathbf{J} + \frac{\partial \mathbf{D}}{\partial t} \quad (4.2)$$

$$\nabla \cdot \mathbf{D} = \rho_f \quad (4.3)$$

$$\nabla \cdot \mathbf{B} = 0 \quad (4.4)$$

with

\mathbf{E} = electric field, \mathbf{B} = magnetic flux intensity

\mathbf{H} = magnetic field, \mathbf{J} = current density

\mathbf{D} = electric displacement field, ρ_f = free charge density

Furthermore \mathbf{D} , \mathbf{E} , \mathbf{B} and \mathbf{H} are coupled to each other by using the electric polarization \mathbf{P} , μ_0 as the free space permeability and the magnetization \mathbf{M} in the

following way:

$$\mathbf{D} = \varepsilon_0 \mathbf{E} + \mathbf{P} \quad (4.5)$$

$$= \varepsilon_0 \mathbf{E} + \varepsilon_0 \chi^{(1)} \mathbf{E} \quad (4.6)$$

$$= \varepsilon (1 + \chi^{(1)}) \mathbf{E} \quad (4.7)$$

$$= \varepsilon \mathbf{E} \quad (4.8)$$

$$\mathbf{B} = \mu_0 \mathbf{H} + \mathbf{M} \quad (4.9)$$

$$= \mu \mathbf{H} \quad (4.10)$$

Here $\chi^{(1)}$ is the first-order (linear) susceptibility, and $1 + \chi^{(1)} = \varepsilon_r$ is the relative permittivity. Note that this equation is only valid for lower field strengths, after higher field strengths will generate also nonlinear effects, which will be covered in section 4.1.4 and the following sections. When the electric field is large enough, the formula changes to

$$\mathbf{D} = \varepsilon_0 \mathbf{E} + \mathbf{P} \quad (4.11)$$

$$= \varepsilon_0 (1 + \chi^{(1)} + \chi^{(2)} \mathbf{E} + \chi^{(3)} \mathbf{E} \mathbf{E} + \dots) \mathbf{E} \quad (4.12)$$

Here $\chi^{(n)}$, $n \in \{1, 2, \dots\}$ is the n^{th} order susceptibility tensor. Generally this tensor is time-dependent [18]. n_2 will be quite significant as the *nonlinear refraction index* later on, and therefore the dependance for it is:

$$n_2 = \frac{3}{8n} \text{Re}(\chi_{xxxx}^{(3)}) \quad (4.13)$$

If n_2 should be used to calculate this tensor, one can use the formula

$$\chi^{(3)} = \frac{4 \cdot \varepsilon_0 \cdot c \cdot n^2}{3} \cdot n_2 [19] \quad (4.14)$$

After optical fibers are in general dielectric waveguides which can neither conduct electricity nor can be magnetized (for low magnetic and electric field strengths) one can also set

$$\mathbf{J} = \mathbf{M} = 0$$

By using the Maxwell equation (4.1), applying a $\nabla \times$ to the first one and mixing it with the equations (4.2), (4.3) and (4.4), we can eliminate \mathbf{B} and \mathbf{D} and obtain as a result:

$$\nabla \times \nabla \times \mathbf{E} = -\frac{1}{c^2} \frac{\partial^2 \mathbf{E}}{\partial t^2} - \mu_0 \frac{\partial^2 \mathbf{P}}{\partial t^2} \quad (4.15)$$

Here c is the speed of light, and the relation $\frac{1}{c^2} = \mu_0 \varepsilon_0$ was used.

The polarization \mathbf{P} (which is already defined as $\varepsilon_0 \chi \mathbf{E}$ in equation (4.12)) can be separated into two parts, the nonlinear and the linear part.

$$\mathbf{P}(\mathbf{r}, t) = \mathbf{P}_L(\mathbf{r}, t) + \mathbf{P}_{NL}(\mathbf{r}, t) \quad (4.16)$$

Generally the evaluation of \mathbf{P} requires a quantum-mechanical approach, but according to [20] for wavelengths in fibers of around $0.5 - 2\mu\text{m}$ we only have to include the first and the third order by using a phenomenological approach. This approach can only be used if \mathbf{P} and \mathbf{E} are far away located from medium resonances (which is the case for the mentioned wavelengths in optical fibers). Therefore the polarization parts can be expressed as:

$$\mathbf{P}_L(\mathbf{r}, t) = \varepsilon_0 \int_{-\infty}^t \chi^{(1)}(t-t') \cdot \mathbf{E}(\mathbf{r}, t') dt' \quad (4.17)$$

$$\begin{aligned} \mathbf{P}_{NL}(\mathbf{r}, t) = \varepsilon_0 \int_{-\infty}^t dt_1 \int_{-\infty}^t dt_2 \int_{-\infty}^t dt_3 \\ \times \chi^{(3)}(t-t_1, t-t_2, t-t_3) : \mathbf{E}(\mathbf{r}, t_1) \mathbf{E}(\mathbf{r}, t_2) \mathbf{E}(\mathbf{r}, t_3) \end{aligned} \quad (4.18)$$

If we put the equations 4.17 and 4.18 together into the equation 4.16 and the result into the shortened maxwell equation 4.15 we receive a nonlinear equation.

According to [18] we can divide the resulting equation into two different equations under the assumption that light propagates in a single linearly polarized mode of the electric field, for example in the basic mode of an optical fiber. One part is responsible for the properties of the radial field distribution in the specific mode in the fiber, while the other part is responsible for the longitudinal dynamical development of the electric field envelope in the fiber in the direction of the propagation of the light (which will be written as C in the following thesis). These two parts can be solved separately, and are coupled together by the frequency dependend propagation constant $\beta(\omega)$ and the effective area $A_{eff}(\omega)$. These two variables are outputs of the first part, and inputs for the second part of the equation. A_{eff} is in [18] defined as

$$A_{eff} = \frac{\left(\int |\mathbf{E}(x, y)|^2 dx \cdot dy \right)^2}{\int |\mathbf{E}(x, y)|^4 dx \cdot dy} \quad (4.19)$$

4.1.2 The generalized nonlinear schrödinger equation (GNLSE)

For deriving the GNLSE several approaches are made, but in this thesis the approach of [21] will be used due to its relative simplicity. Here the electric field which is linearly polarized along \mathbf{x} is defined as

$$\mathbf{E}(\mathbf{r}, t) = \frac{1}{2} \mathbf{x} \{ E(x, y, z, t) \exp(-i\omega_0 t) \} \quad (4.20)$$

$$\tilde{E}(x, y, z, \omega) = F(x, y, \omega) \tilde{A}(z, \omega - \omega_0) \exp(i\beta_0 z) \quad (4.21)$$

with $\tilde{E}(x, y, z, \omega)$ as the Fourier transformation of $E(x, y, z, t)$, $F(x, y, \omega)$ the transverse modal distribution and $\tilde{A}(z, \omega)$ as the complex spectral envelope. ω_0 is a

reference frequency (often the central frequency of the input pulse) and β_0 the wave number at that frequency. To calculate $A(z, t)$ as the time-domain envelope the inverse Fourier transformation is used:

$$\begin{aligned} A(z, t) &= \mathcal{F}^{-1} \left\{ \tilde{A}(z, \omega - \omega_0) \right\} \\ &= \frac{1}{2\pi} \int_{-\infty}^{\infty} \tilde{A}(z, \omega - \omega_0) \exp(-i(\omega - \omega_0)t) d\omega \end{aligned} \quad (4.22)$$

By using the support variable $T = t - \beta_1 \cdot z$ to transform the time variable into a co-moving frame at the envelope group velocity β_1^{-1} , we obtain the time-domain GNLSE for $A(z, t)$:

$$\underbrace{\frac{\partial A}{\partial z} + \frac{\alpha}{2} A - \sum_{k \geq 2} \frac{i^{k+1}}{k!} \beta_k \frac{\partial^k A}{\partial T^k}}_{\text{linear propagation effects}} = i\gamma \left(1 + i\tau_{shock} \frac{\partial}{\partial T} \right) \times \underbrace{\left(A(z, T) \cdot \int_{-\infty}^{\infty} R(T') |A(z, T - T')|^2 dT' \right)}_{\text{nonlinear propagation effects}} \quad (4.23)$$

with the definition of the shock-term

$$\begin{aligned} H(\omega) &= \frac{1}{n_{eff}(\omega) \cdot A_{eff}(\omega)} \\ \tau_{shock} &= \frac{1}{\omega_0} + \frac{d}{d\omega} \ln [H(\omega)] |_{\omega_0} [22] \end{aligned} \quad (4.24)$$

The most decisive element of the nonlinear side of the equation is the variable γ . It describes the nonlinear effects by combining the nonlinear variables in the equation

$$\gamma(\omega) = \frac{\omega \cdot n_2(\omega)}{c \cdot A_{eff}(\omega)} \quad (4.25)$$

Usually one can approximate $\gamma(\omega)$ as $\gamma(\omega_0)$ by neglecting the frequency dependance of γ , but this approach is risky according to [23] after it is possible that pulse components can shift far away from ω_0 during the calculation.

By adding the Raman contribution (which is described in section 4.1.7.3) and converting it into the frequency domain, we obtain the GNLSE in a more usable form [24]:

$$\frac{\partial \tilde{A}'}{\partial z} = i\bar{\gamma}(\omega) \exp(-\hat{L}(\omega)z) \mathcal{F} \left\{ \bar{A}(z, T) \int_{-\infty}^{\infty} R(T') |\bar{A}(z, T - T')|^2 dT' \right\} \quad (4.26)$$

with the frequency dependent nonlinear coefficient $\gamma(\omega)$ defined as

$$\bar{\gamma}(\omega) = \frac{n_2 \cdot n_0 \cdot \omega}{c \cdot n_{eff}(\omega) \cdot A_{eff}^{\frac{1}{4}}(\omega)} \quad (4.27)$$

and

$$\bar{A}(z, T) = \mathcal{F}^{-1} \left\{ \frac{\tilde{A}(z, \omega)}{A_{eff}^{\frac{1}{4}}(\omega)} \right\} \quad (4.28)$$

Furthermore we are replacing \tilde{A} with

$$\tilde{A}'(z, \omega) = \tilde{A}(z, \omega) \exp\left(-\hat{L}(\omega)z\right) \quad (4.29)$$

with \hat{L} as the linear operator, defined as

$$\hat{L}(\omega) = i(\beta(\omega) - \beta(\omega_0) - \beta_1(\omega_0)[\omega - \omega_0]) - \frac{\alpha(\omega)}{2} \quad (4.30)$$

n_{eff} is the frequency dependent effective refraction index, while n_0 the linear refractive index used when determining n_2 . By replacing some parts of the equation by using

$$\mathcal{F}\{C(z, t)\} = \left[\frac{A_{eff}(\omega)}{A_{eff}(\omega_0)} \right]^{-\frac{1}{4}} \tilde{A}(z, \omega) \quad (4.31)$$

and

$$\gamma(\omega) = \frac{n_2 n_0 \omega_0}{c n_{eff}(\omega) \sqrt{A_{eff}(\omega) A_{eff}(\omega_0)}} \quad (4.32)$$

we obtain as „final“ GNLSE

$$\begin{aligned} & \frac{\partial \tilde{C}}{\partial z} - i[\beta(\omega) - \beta(\omega_0) - \beta_1(\omega_0)[\omega - \omega_0]] \tilde{C}(z, \omega) + \frac{\alpha(\omega)}{2} \tilde{C}(z, \omega) \\ & = i\gamma(\omega) \left[1 + \frac{\omega - \omega_0}{\omega_0} \right] \mathcal{F} \left\{ C(z, t) \int_{-\infty}^{\infty} R(T') |C(z, T - T')|^2 dT' \right\} \end{aligned} \quad (4.33)$$

4.1.3 Dispersion

The first optical effect to be described here is the dispersion of light in materials. This is the phenomenon when the phase velocity v_p is depending on the wavelength of the light ($\Rightarrow v_p = v_p(\lambda)$). Furthermore it is a linear effect, but nevertheless plays an important role in influencing the character of nonlinear interactions in the optical material. When taking a special look at the supercontinuum it is important to

note that dispersion influences both the phase velocity and the group velocity in the propagation of the signal. Therefore phasematching plays a significant role in the fiber when determining nonlinear frequency conversion processes, according to [25], and so both linear and nonlinear contributions to the phase mismatch must be considered. Due to the close relation with section 5.2 the dispersion in fibers will be covered separately in section 4.1.3.1.

4.1.3.1 Dispersion in fibers

Usually a fiber consists out of three materials with a different refraction coefficient, the core with the radius a , the cladding with the radius b and the jacket/buffer with the radius c (schematic shown in figure 4.1).

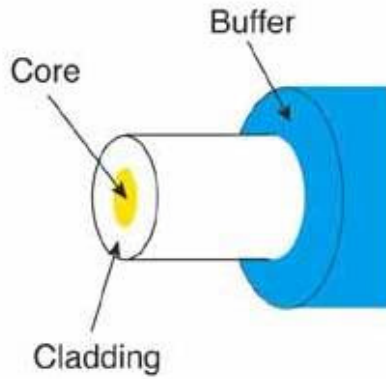


Figure 4.1: Fiber schematic

While the core and the cladding are responsible for the light guidance, the jacket is only for protection purposes. Therefore only the radius and the refraction index of the core ($n_1(\omega)$) and the cladding ($n_2(\omega)$) will be taken in consideration. For light guidance purpose the refraction index of the cladding has to be lower than the refraction index of the core ($n_2 < n_1$) in SIF (step-index fibers). Except the SIF there exists also some other fiber types, such as the graded-index fibers and the photonic crystal fibers. In this

master thesis only SIF will be described. The values mentioned above (radii and refraction indices) define the typical SIF by the numeric aperture

$$NA = \sqrt{n_1^2 - n_2^2} \approx n_1 \sqrt{2 - 2\frac{n_2}{n_1}} \quad (4.34)$$

and the normalized frequency

$$V = 2\frac{\pi \cdot a}{\lambda} \cdot NA \quad [26] \quad (4.35)$$

The numerical aperture determines the maximum angle of incidence of the incoming light beam the laser will support.

$$\alpha_{max} = \arcsin(NA) \quad (4.36)$$

Below $V \approx 2.045$ it can be shown that the fiber only supports a single mode for a specific a , λ and NA according to [27]. In [27] it is also stated that the dispersion

properties of a fiber is typically divided into two contributions, one contribution from the waveguide structure, and the second contribution from the material itself. Typically the refractive index of a fiber is given by the following formula (eq. (4.37)) called „Sellmeier-equation“. In this equation A_j and a_j are the so-called „Sellmeier-coefficients“ [27]:

$$n^2(\lambda) = 1 + \sum_j \frac{A_j \cdot \lambda^2}{\lambda^2 - a_j^2} \quad (4.37)$$

With the refractive index from equation 4.37 one can calculate the propagation constant $\beta(\lambda)$:

$$\begin{aligned} n_{eff}(\lambda) &= \frac{2\pi \cdot \beta(\lambda)}{\lambda} \\ \Rightarrow \beta(\lambda) &= \frac{n_{eff}(\lambda) \cdot \lambda}{2\pi} \end{aligned} \quad (4.38)$$

For getting the GVD(= β_2) one has to Taylor-expand $\beta(\lambda)$ around a specific λ_0 resp. ω_0 :

$$\beta(\omega) = \beta(\omega_0) + \sum_{i=1}^{\infty} \frac{1}{i!} \left. \frac{\partial^i \beta}{\partial \omega^i} \right|_{\omega=\omega_0} (\omega - \omega_0)^i \quad (4.39)$$

While β_2 as the second derivative of β represents the GVD and therefore the most important dispersion value, β_1 respective the first derivative of β is the inverse of the group velocity:

$$\beta_1 = \frac{1}{v_g} \quad (4.40)$$

Furthermore the dispersion of a fiber can be expressed as the dispersion parameter D , with

$$D = -\frac{2\pi \cdot \beta_2 \cdot c}{\lambda^2} = -\frac{c}{\lambda} \frac{\partial^2 n_{eff}}{\partial \lambda^2} \quad (4.41)$$

Also an noticeable value of the fiber is the ZDW, where $\beta_2(\omega) = D(\omega) = 0$. This marks the boundary to the soliton regime (see also 4.1.5). With $D > 0$ resp. $\beta_2 < 0$ the fiber is in the anomalous mode, while with $D < 0$ resp. $\beta_2 > 0$ the fiber is in the normal dispersion mode.

4.1.4 Self-phase modulation

The second effect to describe is the self-phase modulation (SPM). This effect describes the modification of the phase of a pulse because of its own propagation through the material due to the refractive index n_2 . Its phase can be obtained by

$$\Phi = \left(n + n_2 \cdot |E|^2 \right) k_0 \cdot L \quad (4.42)$$

with $k_0 = \frac{2\pi}{\lambda_0}$, L as the fiber length, and n_2 as the nonlinear refraction index (which is derived in 4.13). In the GNLSE this effect is covered by the part

$$\partial_z A = i\gamma|A|^2 A \quad (4.43)$$

This equation can be obtained from 4.23 by neglecting the wavelength dependence of n_{eff} and A_{eff} , the delayed Raman response and the optical shock. One solution to equation 4.43 is

$$A(z, t) = A(0, t) \cdot \exp\left(i\gamma|A(0, t)|^2 z\right) \quad (4.44)$$

Here one can clearly see that the pulse itself influences the resulting phase shape, while the power distribution stays the same. This result is known as „chirp“, where the frequency at the beginning of the pulse is reduced, while the frequency at the end of the pulse is increased.

This effect can also be used for spectral narrowing [28], which will be used in a real-world application later in this thesis (chapter 7). To calculate this effect, one has to start with the intensity per time:

$$I(t) = I_0 \operatorname{sech}\left(\frac{t}{\tau}\right) \quad (4.45)$$

Furthermore the refraction index is:

$$n = n_0 + n_2 \cdot I(t) \quad (4.46)$$

When the pulse is moving through the fiber, the intensity changes, and therefore the refraction index:

$$\begin{aligned} \frac{dn}{dt} &= \frac{dn_0}{dt} + \frac{dn_2}{dt} \cdot I(t) + \frac{dI(t)}{dt} \cdot n_2 \\ &= \frac{dI(t)}{dt} \cdot n_2 \\ &= -\frac{\tanh\left(\frac{t}{\tau}\right) \cdot \operatorname{sech}\left(\frac{t}{\tau}\right)}{\tau} \cdot n_2 \end{aligned} \quad (4.47)$$

The change in the refraction index also changes the phase of the light:

$$\begin{aligned} \varphi(t) &= \omega_0 \cdot t - k \cdot z \\ &= \omega_0 \cdot t - \frac{2\pi}{\lambda_0} \cdot n(I) \cdot L \end{aligned} \quad (4.48)$$

With this result, we get the current frequency $\omega(t)$ by deriving $\varphi(t)$:

$$\begin{aligned} \frac{d\varphi(t)}{dt} &= \omega(t) \\ &= \omega_0 + \frac{2\pi}{\lambda_0} \cdot L \cdot \frac{dn(t)}{dt} \\ &= \omega_0 + \frac{2\pi}{\lambda_0} \cdot L \cdot -\frac{\tanh\left(\frac{t}{\tau}\right) \cdot \operatorname{sech}\left(\frac{t}{\tau}\right)}{\tau} \cdot n_2 \end{aligned} \quad (4.49)$$

This frequency shift is displayed in fig. 4.2

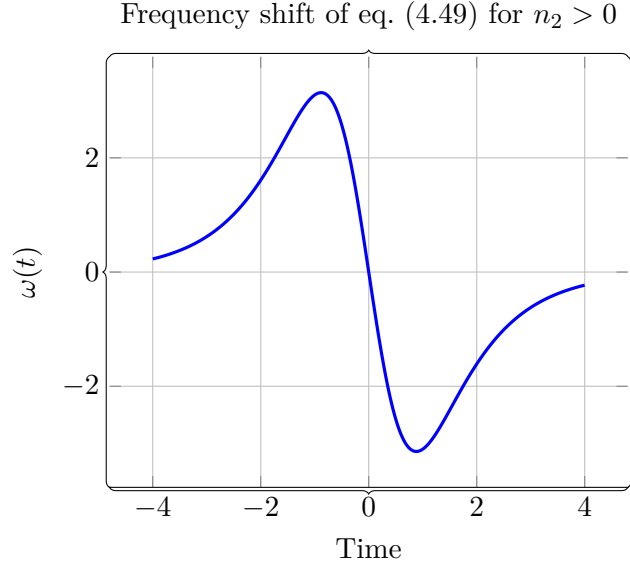


Figure 4.2: Frequency shift for a sech-pulse, function from eq. (4.49)

In this figure one can see that (if $n_2 > 0$) the lower frequencies accumulate at the front of the pulse, while the higher frequencies remain at the rear part of the pulse. Thus, if a soliton should be obtained, negative group velocity dispersion must be applied, which delays the lower frequencies and accelerates the higher frequencies of the pulse. This results in a soliton (see also section 4.1.5).

4.1.5 Solitons

In the anomalous regime of an optical fiber the induced chirps of the incoming pulse can combine to form either a stable or an oscillating soliton [25]. Solitons are an analytical solution to the GNLSE (4.26 or 4.23) without higher order dispersion, the optical shock term and the Raman term. This results in the reduced form of the GNLSE:

$$\partial_z A = -i \frac{\beta_2}{2} \frac{\partial^2 A}{\partial t^2} + i \gamma |A|^2 A \quad (4.50)$$

One of the possible solutions of this formula is

$$A(z, t) = \sqrt[2]{P_0} \operatorname{sech} \left(\frac{t}{t_0} \right) \exp \left(-i \frac{|\beta_2| z}{2 t_0^2} \right) \quad (4.51)$$

The (in this case) relevant Fourier transformation of this result is

$$\tilde{A}(z, \omega) = \pi t_0 \sqrt[2]{P_0} \operatorname{sech} \left(\frac{\omega \pi t_0}{2} \right) \exp \left(-i \frac{|\beta_2|^2 z}{2t_0^2} \right) \quad (4.52)$$

This result of the Fourier transformation is only valid if the peak power P_0 and the pulse width t_0 correlate such that

$$P_0 = \frac{|\beta_2|}{(\gamma t_0)^2}$$

This result and the transformation are obtained from [29]. The soliton which belongs to the resulting formula 4.51 is one of the infinite possible solutions characterized by the soliton order N . N can be calculated by using the characteristic dispersive length scale

$$L_D = \frac{t_0^2}{|\beta_2|} \quad (4.53)$$

and the characteristic nonlinear length scale

$$L_{NL} = \frac{1}{\gamma P_0} \quad (4.54)$$

by the formula

$$N = \sqrt{\frac{L_D}{L_{NL}}} = \sqrt{\frac{\gamma P_0 t_0^2}{|\beta_2|}} = \sqrt{\frac{n_2 \omega}{c A_{eff}(\omega)} \frac{P_0 t_0^2}{|\beta_2|}} \quad (4.55)$$

The soliton with the order $N = 1$ is called the fundamental soliton.

4.1.6 Four-Wave Mixing (FWM)

When the first supercontinuum was generated, the process of FWM was the process which contributed the most to the generation [30]. In this process two additional light frequencies are created by a refractive index modulation in the used material. This process is either called „non-degenerate four-wave mixing“ if the effect creates four different light frequencies at the output of the fiber, or „degenerate four-wave mixing“ if two frequencies of the light coincide. The two new frequencies which are generated are (for two different input frequencies ν_1 and ν_2):

$$\nu_3 = \nu_1 - (\nu_2 - \nu_1) = 2\nu_1 - \nu_2 \quad (4.56)$$

and

$$\nu_4 = \nu_2 - (\nu_1 - \nu_2) = 2\nu_2 - \nu_1 \quad (4.57)$$

Without initial seeding FWM corresponds to an instability of the propagating CW pump and the growth from noise of sidebands symmetric in frequency about the

pump (i.e. only three resulting frequencies). The high-frequency band is called anti-Stokes band, while the low-frequency band is called Stokes-band. If there is already a signal at either ν_3 or ν_4 , this signal is amplified. This effect is called „parametric amplification“ [31]. Another application of the FWM is the frequency-shifting of light [32]. Assuming an undepleted pump of power P_0 , the growth of the sidebands is exponential with the amplitude gain g , given by

$$g = \left[(\gamma \cdot P_0)^2 - \left(\frac{\kappa}{2} \right)^2 \right]^{\frac{1}{2}} \quad [25] \quad (4.58)$$

For single mode fibers the phase mismatch κ is defined by

$$\kappa = 2 \cdot \gamma \cdot P_0 + 2 \sum_{m=1}^{\infty} \left(\frac{\beta_{2 \cdot m}}{(2 \cdot m)!} \right) \cdot \Omega^{2 \cdot m} \quad [25] \quad (4.59)$$

The maximum growth rate is at frequencies satisfying $\kappa = 0$ with an amplitude gain of $g = \gamma \cdot P_0$. This leads to a temporal modulation in the time domain, which is referred to as a modulation instability (MI). That means that FWM and MI are describing the same phenomenon, but in different domains. According to [17] a typical feature of degenerate FWM is that if the pump light is in the anomalous dispersion regime of the pumped material, the gain bands are wide and continuously connected to the pump frequency, while they are separated from the pump frequency and narrow when the pump light is in the normal dispersion regime.

4.1.7 Raman Scattering

Raman scattering is usually associated with the (inelastic) scattering of light by optical phonons. Sometimes also long-wave acoustic phonons and acoustic magnons, which are also referred as Brillouin scattering. Inelastic scattering processes are two-photon events that involve both the annihilation of the incoming photon and the creation of the scattered photon simultaneously [33]. If the frequency of the scattered phonon (defined as ω_s) is smaller than the frequency of the incoming phonon (defined as ω_i), the energy lost

$$\Delta E_P = |\hbar(\omega_i - \omega_s)| \quad (4.60)$$

is added to the material. This process is called *Stokes*-process. If energy is added to the scattered phonon, i.e. $\omega_s > \omega_i$ the process is called *Anti-Stokes*-process. This process is heavily depending on the temperature of the scattering material, assuming it is in thermal equilibrium, after these *Anti-Stokes*-processes can only occur if the material is not in the ground state and is therefore able to „emit“ energy. The process described above is also valid if more than one phonon is emitted, leading

to higher-order Raman scattering. To describe that situation mathematically the formula 4.60 has to be changed to

$$\Delta E_G = |\hbar(\omega_i - \omega_s)| \quad (4.61)$$

by using the definition of E_G as

$$\Delta E_G = \sum_N \Delta E_{P_N} \quad (4.62)$$

with N the amount of generated phonons. Formula 4.61 is also valid for both the *Stokes-* and *Anti-Stokes-*process. The Raman scattering process has to follow the conservation laws for energy and momentum. This will be proven first in a crystal, and afterwards extended to both glass and fiber materials.

First we consider an incoming monochromatic light beam with the frequency ω_i and the propagation vector $|\mathbf{k}_i| = \omega_i \cdot n(\omega_i) \cdot \frac{1}{c}$ with $n(\omega_i)$ as the propagation index and c as the speed of light. Furthermore we define the scattering frequency as

$$\omega = \omega_i - \omega_s \quad (4.63)$$

and the scattering wave vector as

$$\mathbf{k} = \mathbf{k}_i - \mathbf{k}_s \quad (4.64)$$

According to [34] the elementary excitations can be labeled by the wave vector \mathbf{q} , also known as the crystal momentum. These modes can be represented by a dispersion relation that connects a frequency ω_q to each value of \mathbf{q} . For first-order processes only one elementary excitation participates in the process, and thereby the momentum conservation directly translates into the requirement that the scattering wave vector equals the excitation wave vector:

$$\mathbf{q} = \mathbf{k} \quad (4.65)$$

The same process leads to

$$\omega = \omega_q \quad (4.66)$$

For higher-order processes equation 4.65 has to be written as

$$\mathbf{k} = \sum_i \mathbf{q}_i \quad (4.67)$$

This wave vector conservation as stated in 4.65 and 4.65 is not possible to be written in this form anymore if the scattering material has no translation symmetry, even if the linear momentum is still conserved. That means that the Bloch theorem does not apply anymore, and therefore the wave vectors are not good quantum numbers

for labeling modes [34]. This applies both for crystals with a small imperfection as well as alloys, fibers and glasses (amorphous solids). While the Raman spectrum of crystals in general consists out of one or several sharp peaks, the Raman spectrum of glasses or other amorphous materials consists out of several broad peaks due to the wider variation of possible vibrational excitations. This also leads to a specific peak near the central frequency, called the *Boson Peak*. Until today the origin of the boson peak remains not completely solved [35], but there are several explanations for it. On the one hand, there is the possibility that the modes giving rise to the boson peak are (quasi)-localized and distinct from sound waves [36] and arise from peculiarities of the interatomic forces in amorphous materials. On the other hand the density of states of the amorphous material leading to the boson peak could only be the modification of the crystalline density of states due to the random fluctuation of force constants [37]. An example of this broadening can be seen in fig. 4.3.

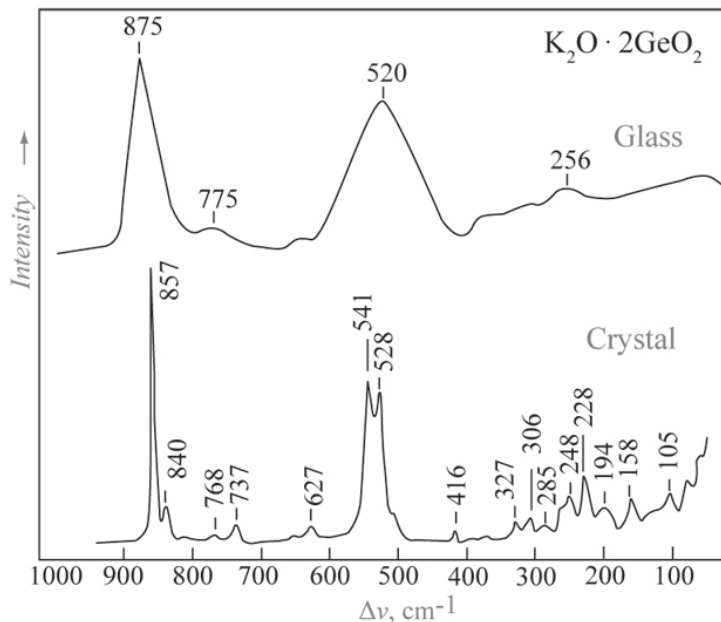


Figure 4.3: Comparison of Raman spectra between glass and crystals, [38]

Additionally Raman scattering can be separated into two domains, the spontaneous Raman scattering (SRS) and the induced Raman scattering (IRS). SRS is rather the „normal“ Raman scattering. It describes the process if an incoming photon excites a phonon in the material, and thereby its energy gets lowered. This process happens randomly, and is non-determinable (Refer for this also to 4.1.7.1). The IRS is even more random, after it is based on precedent SRS-scattering of atoms or molecules. A further look in this area will be taken in section 4.1.7.2.

4.1.7.1 Stokes- and Anti-Stokes-Scattering

In inelastic light scattering processes a quantum of the incident radiation is annihilated and a quantum of the scattered radiation is created (refer for that also to fig. 4.4) while emitting a phonon. The scattering might occur randomly depending on the scattering cross section of the sample material. The incoming light excites molecules or atoms in the solid. This combined with the polarization of the light results in the induced polarization \mathbf{P} . This polarization is represented by a modulation of the electric susceptibility of the sample. Thus we can introduce a modulated Raman susceptibility $\delta_{\chi_{ij}}$:

$$P_i(\omega_S) = \sum_j \delta_{\chi_{ij}} E_j(\omega_L) \quad [39] \quad (4.68)$$

with $\mathbf{E}(\omega_L)$ the electric field of the incoming light. This susceptibility $\delta_{\chi_{ij}}$ influences the Raman intensity by

$$I(\omega_L, \omega_S, \mathbf{k}) = |\hat{\mathbf{e}}_s \cdot \delta_{\chi_{ij}} \cdot \hat{\mathbf{e}}_L|^2 \quad [34] \quad (4.69)$$

with $\hat{\mathbf{e}}_n$ as the unit polarization vectors. Furthermore, $\delta_{\chi_{ij}}$ can be written as

$$\delta_{\chi_{ij}} = \sum_m R_{ij}^{(m)} Q_m(\mathbf{0}) + \sum_{mn, \mathbf{q}\mathbf{p}} R_{ij}^{(mn)} Q_m(\mathbf{q}) Q_n(\mathbf{p}) + \dots \quad [40] \quad (4.70)$$

with Q_j as the phonon coordinate, $R_{ij}^{(m)}$ as the first-order Raman tensor and $R_{ij}^{(mn)}$ as the second-order Raman tensor. The first-order Raman tensor represents the case for scattering with only one phonon, while the second-order tensor represents the case for scattering with two phonons. Now, with eq. (4.61) and eq. (4.70) we can calculate the scattering intensity for both the Stokes and anti-Stokes process:

$$I_{ij} \propto |R_{ij}^{(m)}|^2 |\langle n+1 | Q_m | n \rangle|^2 \quad (4.71)$$

with the Bose factor

$$n(\omega, T) = \frac{1}{\exp\left(\frac{\hbar \cdot \omega}{k_B \cdot T}\right) - 1} \quad (4.72)$$

To add a phonon to the crystal the matrix element is

$$\langle n | Q_m | n+1 \rangle \approx (n+1)^{\frac{1}{2}} \quad [41] \quad (4.73)$$

and to remove a photon the element is

$$\langle n | Q_m | n-1 \rangle \approx \sqrt{n} \quad [41] \quad (4.74)$$

Thus we get the intensity ratio between Stokes and anti-Stokes:

$$\frac{I_S}{I_{AS}} = \exp\left(\frac{\hbar \cdot \omega}{k_B \cdot T}\right) \quad (4.75)$$

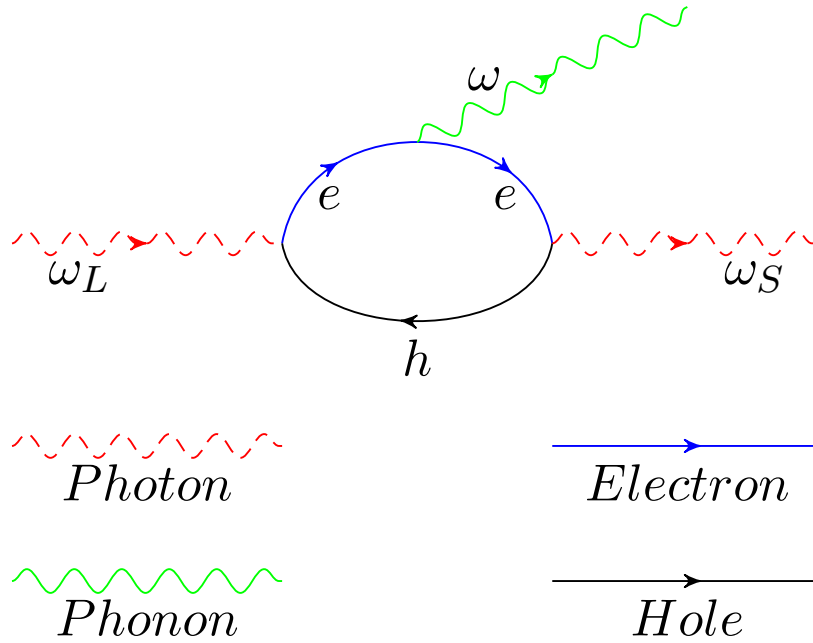


Figure 4.4: Processes in Raman scattering shown as Feynman diagram, [39]

As stated above and in eq. (4.68) the electric susceptibility is mostly dependant on the coupling of the light to the electric moment of the electronic excitations [39]. This process is only visible if the incident light is resonant with lattice vibration excitations, which is particularly described in [39], and thus it will not be repeated in this thesis.

4.1.7.2 Induced Raman Scattering

Compared to the spontaneous Raman the induced Raman scattering only happens on very high power levels, due to the necessity of having already excited Stokes photons which are still trapped in the material. Those Raman photons can then be used to amplify a second signal at their wavelength. Those photons can also result from an external pumping light, i.e. if the material is pumped by a laser, and then a signal laser gets injected. This property makes the induced Raman scattering a valuable effect for being created in fiber amplifiers. If this amplification happens in glasses or fibers, the affected frequencies are significantly broader than in crystals, resulting in a possible broad-band amplifier.

4.1.7.3 Contribution of Raman scattering in the GNLSE

The Raman scattering contributes to the general light modulation both immediately and delayed. The immediate response is the electronic response of the material to the incoming light, arising from the nonresonant virtual electronic transitions with a timescale of a femtosecond or less [42], while the delayed response is the nuclear response of the material, and the timescale is largely given by the phonon lifetime (approximately 100 femtoseconds) [42]. In general the contribution is therefore formulated as

$$R(T) = (1 - f_R) \underbrace{\delta(t)}_{\text{electronic response}} + f_R \underbrace{h_R(T)}_{\text{nuclear response}} \quad (4.76)$$

In this equation the first term is the immediate response function resulting from the Kerr effect [43], and the second term is the delayed Raman response function. f_R is dependant on which delayed response function is used. During my research I found three different response functions in [42], [44] and [19]. In this model the function from [44] is used, with f_R set to 0.18. The form of the Raman response function $h_R(T)$ is also dependant on the material. The two more noticeable functions for the Raman response are

- „Blow-Wood“, [42]:

$$h_R(t) = \frac{\tau_1^2 + \tau_2^2}{\tau_1 \tau_2^2} \exp\left(-\frac{t}{\tau_2}\right) \sin\left(\frac{t}{\tau_1}\right) \quad (4.77)$$

with $\tau_1 = 12.2\text{fs}$ and $\tau_2 = 32\text{fs}$ [43][44]

- „Lin-Aggrawal“, [44]:

$$h_R(t) = (1 - f_R) \delta(\tau) + f_R [(f_a + f_b) h_a(\tau) + f_b h_b(\tau)] \quad (4.78)$$

with

$$\tau_1 = 12.2\text{fs}$$

$$\tau_2 = 32\text{fs}$$

$$\tau_b = 96\text{fs}$$

$$f_a = 0.75$$

$$f_b = 0.21$$

$$f_c = 0.04$$

$$h_a(\tau) = \tau_1 (\tau_1^{-2} + \tau_2^{-2}) \exp\left(-\frac{\tau}{\tau_2}\right) \sin\left(\frac{\tau}{\tau_1}\right)$$

$$h_b(\tau) = \left[\frac{(2\tau_b - \tau)}{\tau_b^2} \right] \exp\left(-\frac{\tau}{\tau_b}\right)$$

- „Hollenbeck“, [19] (which will be used in section 6.2)

$$h_R(t) = \sum_{i=1}^1 3 \frac{A'_i}{\omega_{v,i}} \cdot \exp(-\gamma_i \cdot t) \cdot \exp\left(-\frac{\Gamma_i^2 \cdot t^2}{4}\right) \sin(\omega_{v,i} \cdot t) \cdot \Theta(t) \quad (4.79)$$

with

$$\Theta(x) = \begin{cases} 0 & \forall x < 0 \\ 1 & \forall x \geq 0 \end{cases}$$

and

$$\begin{aligned} A'_i &= A_i \cdot \omega_{v,i} \\ \Gamma_i &= \pi \cdot c \cdot G_i \\ \gamma_i &= \pi \cdot c \cdot L_i \\ \omega_{v,i} &= 2 \cdot \pi \cdot c \cdot P_i \end{aligned}$$

and A_i , G_i , L_i and P_i taken from table 4.1.

i	$P_i([\text{cm}^{-1}])$	A_i	$G_i([\text{cm}^{-1}])$	$L_i([\text{cm}^{-1}])$
1	56.25	1	52.10	17.37
2	100	11.40	110.42	38.81
3	231.25	36.67	175	58.33
4	362.5	67.67	162.50	54.17
5	463	74	135.33	45.11
6	497	4.5	24.50	8.17
7	611.50	6.8	41.50	13.83
8	691.67	4.6	155	51.67
9	793.67	4.2	59.50	19.83
10	835.5	4.5	64.3	21.43
11	930	2.70	150	50
12	1080	3.1	91.00	30.33
13	1215	3	160	53.33

Table 4.1: Parameters for the Hollenbeck Raman response approximation

One possibility to determine the function is that the Raman gain function and the Raman response function are linked by

$$g_r(\Delta\omega) = \frac{\omega_0}{cn\omega_0} f_R \chi_{\lambda\lambda\lambda\lambda}^{(3)} \text{Im} \left(\tilde{h}_r(\delta\omega) \right) \quad [19] \quad (4.80)$$

This function will also be used later during the actual Raman gain measurements in section 6.2. For silica fibers the best approximation for h_R is the function from Blow-Wood, displayed in 4.77. To compare the functions graphically they are displayed in fig. 4.5.

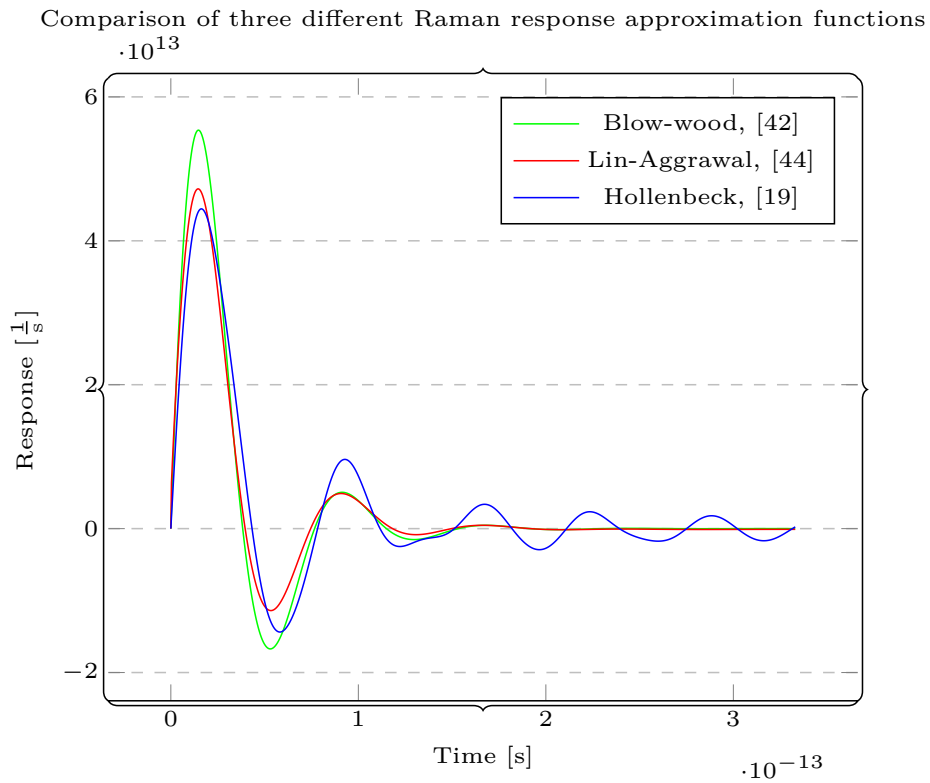


Figure 4.5: Comparison of the different Raman approximation functions

In order to calculate those functions, one has to measure the Raman gain of the material to be measured. With this measurement one can obtain the Raman response function by using eq. (4.80). Here \tilde{h}_R is the Fourier transformation of the response functions mentioned above, n_0 the refraction index and $\chi^{(3)}$ the third-order susceptibility of the material. The exact calculation of the Raman response function by using a measured signal will be done in section 6.2. For getting the Raman response function from the Raman gain function, one has to invert eq. (4.80):

$$h_R(\tau) = \frac{4 \cdot n(\omega_P) \cdot c}{3\omega_P \cdot \chi^{(3)} \cdot f_R} \int_{-\infty}^{\infty} g_R(\Omega) e^{-i\Omega \cdot \tau} d\Omega \quad [45] \quad (4.81)$$

4.2 Numerical simulation methods

In general there are two approaches to solve the GNLSE numerically. The first approach is the Split-Step-Method which is based on dividing the GNLSE into two parts, the linear part and the nonlinear part (further explained in section 4.2.2, [46], [47] and [48]). This approach was more complicated to implement, thus the second possible approach using an ODE-solver was mainly used. This approach will be explained in part 4.2.1. The advantages and disadvantages of both approaches will be further explained in section 6.3.4.

4.2.1 ODE-solving

The way to solve the GNLSE which is used in this thesis is to use an ODE-solver, implemented in several programming languages. For this thesis the ODE-solver from the scipy-package in python was used, while the algorithm itself was based on a proposal written in matlab [49]. For being able to solve the GNLSE with an ODE-solver, it had to be rearranged:

$$\frac{\partial \tilde{A}}{\partial z} = i \frac{\gamma \omega}{\omega_0} \exp(-\hat{L}z) \mathcal{F} \left\{ A(z, t) \int_{-\infty}^{\infty} R(t') |A(z, t - t')|^2 dt' \right\} \quad (4.82)$$

In this formula the frequency dependency of n_2 , A_{eff} and n_2 compared to 4.33 was ignored. Furthermore to be able to solve the integral

$$\int_{-\infty}^{\infty} R(t') |A(z, t - t')|^2 dt'$$

it had to be reformulated. After the Raman formula 4.76 with the delayed response from [44] will be used (shown in equation 4.77), the equation can be rewritten as:

$$\begin{aligned} \int_{-\infty}^{\infty} R(t')|A(z, t - t')|^2 dt' &= \int_{-\infty}^{\infty} [(1 - f_R)\delta(t') + f_R h_R(t')] |A(z, t - t')|^2 dt' \\ &= \underbrace{(1 - f_R)|A(z, t)|^2}_{\text{Kerr-effect}} + f_R \underbrace{\int_{-\infty}^{\infty} h_R(t')|A(z, t - t')|^2 dt'}_{\text{stimulated Raman scattering}} \end{aligned}$$

The second part of the result is a convolution integral which can be calculated according to the convolution theorem by using both the Fourier- and inverse Fourier-transformation. This results in (according to [25])

$$\int_{-\infty}^{\infty} h_R(t')|A(z, t - t')|^2 dt' = \Delta t \mathcal{F}^{-1} \left[\mathcal{F}(h_R(t)) \mathcal{F}(|A(z, t)|^2) \right] \quad (4.83)$$

Therefore one can write the integral mentioned above as

$$\begin{aligned} \int_{-\infty}^{\infty} R(t')|A(z, t - t')|^2 dt' &= (1 - f_R)|A(z, t)|^2 + \\ &f_R \Delta t \mathcal{F}^{-1} \left[\mathcal{F}(h_R(t)) \mathcal{F}(|A(z, t)|^2) \right] \end{aligned} \quad (4.84)$$

Thus the implementable rewritten formula for equation 4.82 is

$$\begin{aligned} \frac{\partial \tilde{A}}{\partial z} &= i \frac{\gamma \omega}{\omega_0} \exp(-\hat{L}z) \cdot \\ &\mathcal{F} \left\{ A(z, t) \cdot \left((1 - f_R)|A(z, t)|^2 + f_R \Delta t \mathcal{F}^{-1} \left[\mathcal{F}(h_R(t)) \mathcal{F}(|A(z, t)|^2) \right] \right) \right\} \end{aligned} \quad (4.85)$$

This rewritten formula is implemented in python in section 6.3.1.

4.2.2 Split-Step solving approach

A second way to solve the GNLSE is splitting it up into the linear part and the nonlinear part. This approach is called the „split-step“ approach. Written in formula

it is:

$$\begin{aligned} \frac{\partial \tilde{A}'}{\partial z} &= i\bar{\gamma}(\omega) \exp(-\hat{L}(\omega)z) \cdot \\ &\mathcal{F} \left\{ \bar{A}(z, T) \int_{-\infty}^{\infty} R(T') |\bar{A}(z, T - T')|^2 dT' \right\} \text{ from eq. (4.26)} \\ \frac{\partial \tilde{A}}{\partial z} &= \begin{cases} DA + NA & \forall t \in \mathbb{R}, \forall z \in L \setminus \{0\} \\ a_0 & \forall t \in \mathbb{R}, z = 0 \end{cases} \end{aligned} \quad (4.86)$$

$$D = -\frac{1}{2}\alpha - \sum_{n=2} \beta_n \frac{i^{n-1}}{n!} \partial_t^n \quad (4.87)$$

$$N = -i\gamma \left(1 + \frac{1}{\omega_0} \partial_t \right) \left[(1 - f_R) |A|^2 + f_R (h_R * |A|^2) \right] \quad (4.88)$$

This equation has to be solved step-wise and numerically. There are several different possibilities to do that, for example the symmetric split-step method [50] or the fourth-order Runge-Kutta in the Interaction Picture (RK4IP) method [51]. While the first method approximates the next step with

$$A(z+h, T) = \exp\left(\frac{h}{2}\hat{D}\right) \cdot \exp\left(\int_z^{z+h} \hat{N} dz'\right) \cdot \exp\left(\frac{h}{2}\hat{D}\right) A(z, t) \quad (4.89)$$

$$\approx \exp\left(\frac{h}{2}\hat{D}\right) \cdot \exp\left(\frac{h}{2}\hat{N}\right) \cdot \exp\left(\frac{h}{2}\hat{D}\right) A(z, t) + O(h) \quad (4.90)$$

the second one modifies the well-known Runge-Kutta-4 method:

$$A_I = \exp\left(\frac{h}{2}\hat{D}\right) A \quad (4.91)$$

$$k_1 = \exp\left(\frac{h}{2}\hat{D}\right) [h\hat{N}(A)] A \quad (4.92)$$

$$k_2 = h\hat{N}\left(A_I + \frac{k_1}{2}\right) \left[A_I + \frac{k_1}{2}\right] \quad (4.93)$$

$$k_3 = h\hat{N}\left(A_I + \frac{k_2}{2}\right) \left[A_I + \frac{k_2}{2}\right] \quad (4.94)$$

$$k_4 = h\hat{N}\left(\exp\left(\frac{h}{2}\hat{D}\right)(A_I + k_3)\right) \cdot \exp\left(\frac{h}{2}\hat{D}\right) [A_I + k_3] \quad (4.95)$$

$$A(z+h, T) = \exp\left(\frac{h}{2}\hat{D}\right) \left[A_I + \frac{k_1}{6} + \frac{k_2}{3} + \frac{k_3}{3}\right] + \frac{k_4}{6} + O(h^4) \quad (4.96)$$

In order to calculate \hat{D} and \hat{N} in a way that a computer can calculate them, one can use the Fourier transformation. This leads to ([52]):

$$\exp\left(\frac{\hbar}{2}\hat{D}\right)A = \mathcal{F}^{-1}\left[\hat{A} \cdot \exp\left(\hat{d} \cdot \frac{\hbar}{2}\right)\right] \quad (4.97)$$

$$\hat{A} = \mathcal{F}[A] \quad (4.98)$$

$$\hat{d} = -\frac{1}{2}\alpha + i \cdot \sum_{n=2} \frac{\beta_n}{n!} (2\pi\nu)^n \quad (4.99)$$

and

$$\hat{N} = -i\gamma \left(1 + \frac{1}{\omega_0} \partial_t\right) \cdot \left[(1 - f_R)|A|^2 + f_R (h_R * |A|^2)\right] \text{ from eq. (4.88)}$$

$$h_R * |A|^2 = \mathcal{F}^{-1}\left[\hat{h}_R \cdot |\hat{A}|^2\right] \quad (4.100)$$

$$-i\gamma \left(1 + \frac{1}{\omega_0} \partial_t\right) = \mathcal{F}^{-1}\left[i\gamma \left(1 - \frac{i \cdot \omega}{\omega_0}\right)\right] \quad (4.101)$$

\Rightarrow

$$\hat{N} = \mathcal{F}^{-1}\left[i\gamma \left(1 - \frac{i \cdot \omega}{\omega_0}\right) \cdot \mathcal{F}\left[(1 - f_R)A \cdot |A|^2 + f_R \cdot A \cdot \mathcal{F}^{-1}\left[\hat{h}_R \cdot |\hat{A}|^2\right]\right]\right] \quad (4.102)$$

This method of calculation makes the conversion into other programming languages significantly easier, as one does not have to rely on the existence of an ODE-solver in this programming language (which on the other hand makes the initial implementation in e.g. python or matlab easier). Further advantages and disadvantages of both approaches are discussed in section 6.3.

4.3 Summary

In this part a short overview over the different nonlinear and linear effects materials due to the influence of light was given including their derivation from the basic Maxwell laws (section 4.1.1), beginning from dispersion (section 4.1.3) with a special part dedicated to fibers (section 4.1.3.1) and SPM (section 4.1.4) to Raman scattering (section 4.1.7.3) including a calculation of different Raman effects and their contribution. In order to combine those effects in one formula the GNLSE and its derivation was described (section 4.1.2). Finally two different ways of solving the GNLSE numerically are proposed and shortly explained in theory.

Chapter 5

Experimental Setup

For being able to measure the Raman shift of a glass fiber or a crystal we had to use a Raman spectrometer which was out of work for at least around eight years. This spectrometer was controlled by a computer built in 1987 and a custom-build ISA extension card in the computer. The parts which were controlled in the spectrometer were on the one hand the spectrometer itself, i.e. the movement of the gratings and the current position of the gratings and on the other hand the controlling device for the photo multiplier tube.

5.1 Raman spectrometer

The Raman spectrometer which has been used is the spectrometer 14018 from SPEX industries. Its basic schematic is shown in figure 5.1.

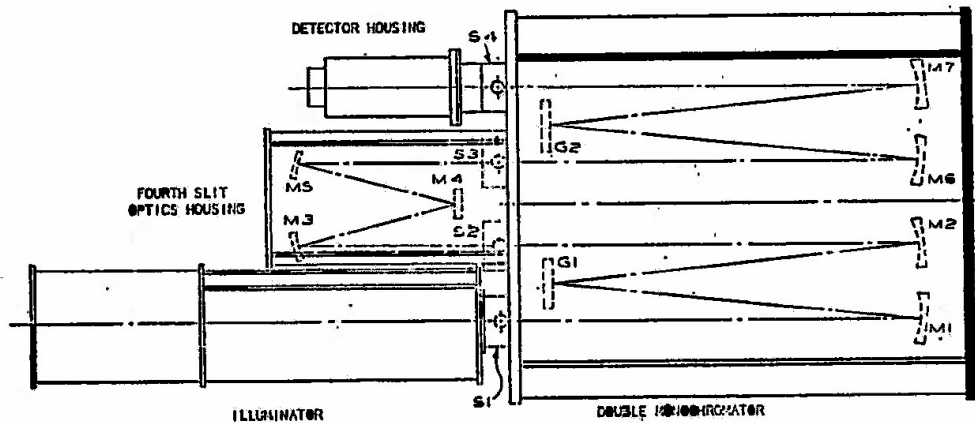


Figure 5.1: Spectrometer scheme

There you can see that it usually operates with the gratings „G1“ and „G2“ while directing the light beam via the mirrors „M1“ to „M7“ and controlling the beam intensity with the slit width of the slits „S1“ to „S4“. The full data sheet is in the appendix A.4.1. The detector used was the photomultiplier tube C31034 from RCA electronic components. This photomultiplier should be sensitive in a broad spectral range from 200nm up to 900nm, according to the data sheet in the appendix (A.4.2).

5.1.1 Redesign of the used hardware

Unfortunately we found out that the computer was not able to fully boot anymore because of a failed hard disk. Therefore we had to design a new control computer. By reverse-engineering of the old ISA extension card (refer also to fig. A.17) we could find out how the external devices were connected to the computer, and by rescuing the pascal control programs we could see how they were controlled. After it was extremely expensive to get a new hard disk for the old control pc without knowing if only this hard disk is broken, we decided to build the pc again from scratch. For that we are using a BeagleBone Black, a credit-card sized ARM-PC with Debian Linux as operating system. The advantage of this small system is that it has 65 GPIO-connections [53] which can be used for the communication with external devices. Furthermore there is the possibility to attach special „capes“ to the PC. These capes are extension boards which enhance the properties of the BeagleBone Black, for example by enabling it to control stepper motors or to add even more GPIO ports. Finally, it can be controlled either by connecting a keyboard and a monitor to it or remotely via a LAN connection. These properties made it quite suitable for our purpose. For enabling the BeagleBone Black to control the stepper motor inside of the spectrometer, we used an already available stepper motor controller which had already been used for controlling the stepper motor based on the controller BD300 from Phytron [54]. The controlling of the motor therefore only needed an input of the steps and the direction, everything else was set.

5.1.1.1 First cape

After the BeagleBone Black only supports 3.3V as I/O-voltage, we had to use voltage level converters from 3.3V to 5V. These voltage converters furthermore where used as a basic protection of the BeagleBoard, after they are easier to replace in case of a short circuit or a voltage overload. The schematic can be seen in the appendix A.2.1 (see figure A.16). The main part of the PCB is shown in figure 5.2.

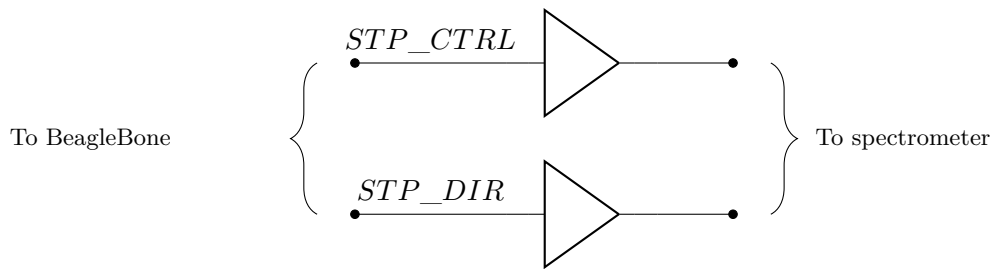


Figure 5.2: Main part of the control cape

The two voltage translators shown in this picture are the onliest parts which are important at this cape, every other connection is not used (due to both unnecessary and failure of the potential input devices). With this cape it could be confirmed that the stepper motor is still working, and that the gratings are still moving. Furthermore it could be tested (with the help of a small adjusting laser, see also 5.1.4) if the PMT was still working. Unfortunately one result was that either the DPC, which is used for controlling the PMT and counting the incoming photons, was defective or it was not properly operated (due to a missing manual). Therefore the DPC was only used as a high voltage generator, which was used for powering the PMT, but it did not print any BCD encoded values from the digital output of the DPC. Furthermore the first cape used pins which are usually used for the HDMI-output, therefore blocking the possibility of using a separate monitor. In order to solve that the LAN-port was used for communication. To be able to use the monitor output again a second cape was designed, while continuing with the measurements and tests with the first cape.

5.1.1.2 Second cape

The design of the second cape was done while doing the test runs with the first cape, born from the necessity to enable the monitor output again. Therefore it was decided to use the I²C-output of the beaglebone and use a multiplexer for controlling the stepper motor and the other remote devices. While designing this cape the problem of the malfunctioning DPC emerged, and therefore the decision was made to drop the cape while still being in the design phase in favor of a complete redesign from scratch.

5.1.1.3 Third cape

After connecting an oscilloscope to the output of the PMT we found out that we could measure the photon count if we use an A/D-converter, without having to rely on the counting of the DPC. Based on the DPC a 12-bit-A/D-converter was used for this purpose. Furthermore two additional boards were designed in order

to replace the original step-motor-controller and the current cape. The schematics for all of these controllers are shown in the appendix (section A.2.2, A.2.3 and A.2.4). Each board is controlled by an AtXMega 16A4U-AU, a small μ -controller, including a 12-bit-A/D-converter and two USART-ports. These ports are used for communication between the subcontrollers and the main (Cape)-controller by using the RS485-standard. This standard ensures the data integrity over a longer distance. The software for the μ -controller has been written in a mixture of C and C++. The listing of the software can be found in appendix A.2.1, appendix A.2.4, appendix A.2.2 and appendix A.2.3. Unfortunately due to several hardware failures it was impossible to test the newly designed controllers in joint operations (only parts of them are tested), thus all operations were done either manually (such as reading the current count/mV-values) or via the initially designed cape.

5.1.2 Redesign of the used software

To control the Beaglebone and with it the spectrometer a software was designed based on QT5 and C++. It supports both local and remote control abilities, i.e. its GUI can be used either directly (either via the cape from A.2.1 or the cape from A.2.2) on the Beaglebone if it is connected to a monitor, or via LAN-access. If used as a remote controller, it opens a SSH-connection to the Beaglebone, starts the internal controller of the Beaglebone, and connects to it afterwards via TCP. It uses in the current version three data lines from the Beaglebone, for movement updates, for position updates and for sensor updates. The program itself has one connection to the Beaglebone, using it for general commands such as movement commands and sensor updates, which will be sent back via one of the three mentioned channels. Furthermore it is able to plot the aquired data and store it together with the scan data. Additionally it can be used for simple movement of the spectrometer and the manual aquisition of a scan. Its source code is shown in appendix A.2.2 The basic layout of the program is shown in figure 5.3. Here it has to be noticed that every column represents a single thread, i.e. in total the program is running 13 threads in parallel. This leads to a decreased workload for each thread and an increased responsiveness. In addition the whole program is conceived as a modular program, i.e. every part can easily removed and replaced just by connecting the correct signals. Those features also make it easier to create a new frontend for the control software, or to add new modules, which was the reason for choosing this architecture.

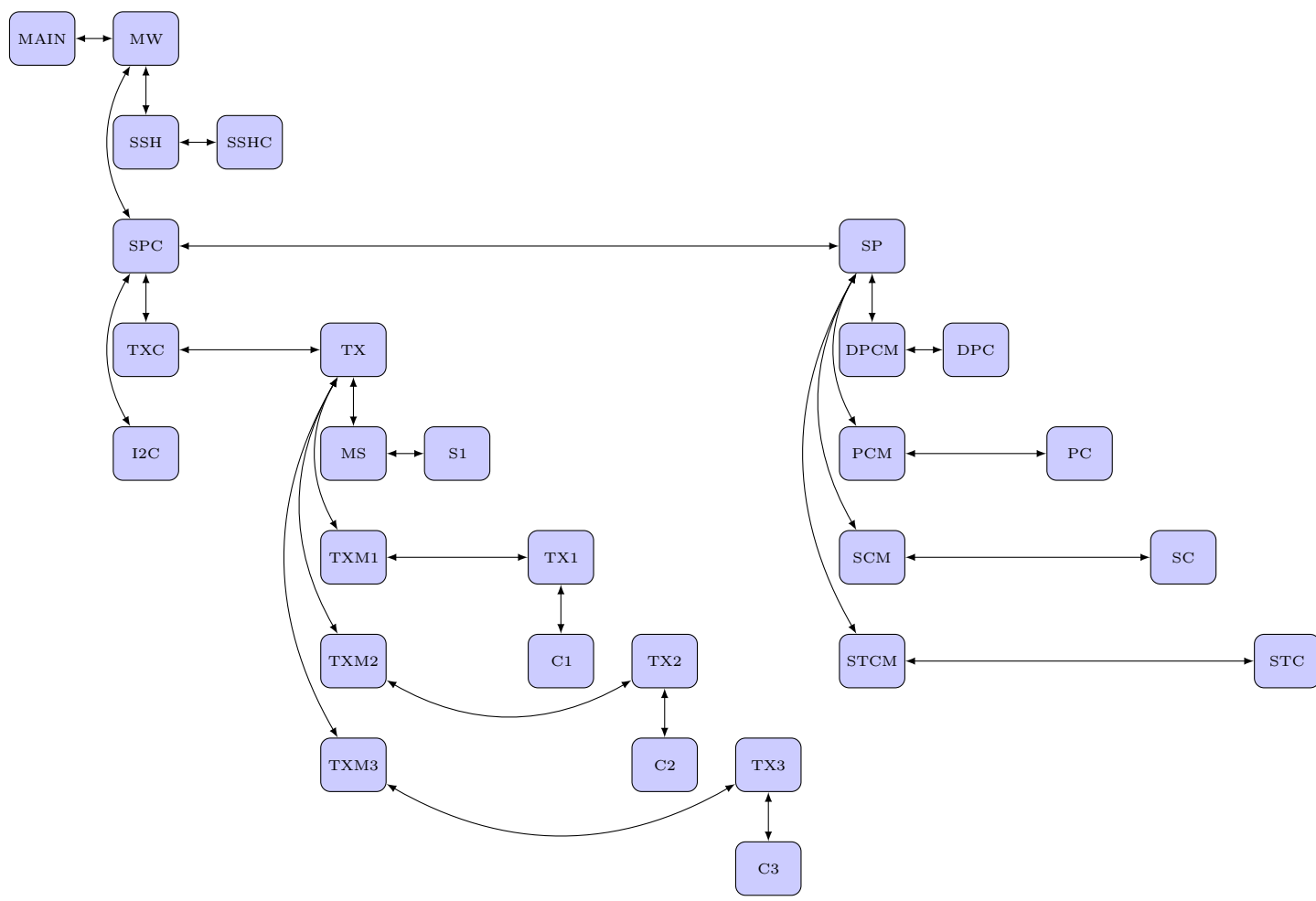


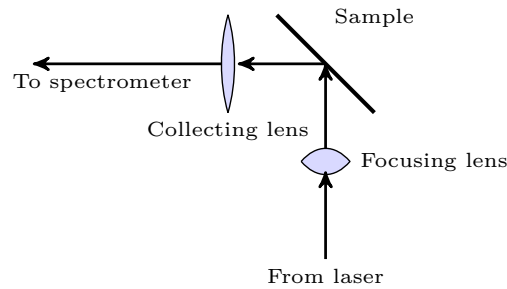
Figure 5.3: Basic structure of the control program. The symbols used in this figure are explained in table 5.1

MAIN	main() -function
MW	Function MainWindow() , including the GUI
SSH	SSH-Controller
SSHC	SSH-Worker, moving all SSH-actions to another thread
SPC	Spectrometer controller, provides a virtual spectrometer to the main program, hides all further communications
SP	Function for spectrometer itself, if executed directly on the BBB. Also executed in separate thread
TXC	Controller for the LAN data transmission
TX	TX-Worker, moving all LAN functionality to another thread
I ² C	I ² C-connector, converts the signals gotten via I ² C to data for the spectrometer. Currently not implemented
MS	Masterserver-Controller, is used for sending commands via LAN
S1	Server, moves all server functionality to another thread
TXM1	Client 1 (C1) controller
TXM2	Client 2 (C2) controller
TXM3	Client 3 (C3) controller
TX1	Moves the C1-control to a separate thread
TX2	Moves the C2-control to a separate thread
TX3	Moves the C3-control to a separate thread
C1	Client 1, receives general data from the BBB
C2	Client 2, receives movement data from the BBB
C3	Client 3, receives movement data from the BBB
DPCM	Controls the incoming data from the DPC, delivered by the DPC-Worker (DPC)
PCM	Controls the polarizer settings via the polarizer worker (PC)
SCM	Controls a scan directly, i.e. is called when a scan should be done. Is responsible for calculations and executions of the scan. Works via the scan worker (SC)
STCM	Stepper controller, controls the movement of the stepper motor via the worker (STC)
DPC	DPC-worker in separate thread
PC	Polarizer worker in separate thread
SC	Scanner worker in separate thread
STC	Stepper motor controller in separate thread

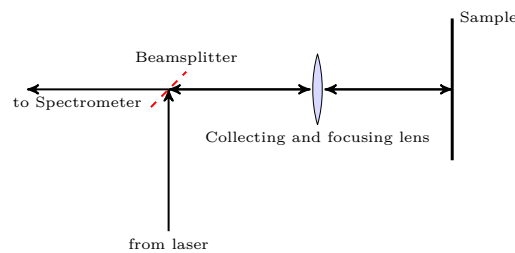
Table 5.1: Symbol explanation to figure 5.3

5.1.3 Scattering geometries

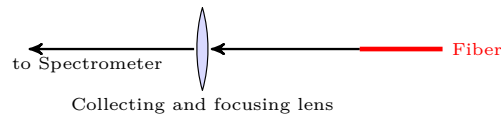
Three different scattering geometries were used in this setup. On the one hand (for bulk materials) a simple 90° - or 180° -scattering geometry was used (displayed in fig. 5.4a and fig. 5.4b). Furthermore a simple collection geometry was used for collecting the light coming from the fiber, which is displayed in fig. 5.4c.



(a) Scattering geometry for a scattering angle of 90°



(b) Scattering geometry for a scattering angle of 180°



(c) Scattering geometry for a parallel fiber

Figure 5.4: Used scattering geometries

While the third one (fig. 5.4c) exclusively was used for fibers, the first one (fig. 5.4a) was used for calibration with GSGG:Cr (compare to fig. 5.6) and for the measurements with diamond (compare to fig. 5.8). The second scattering geometry was used both for silicon (compare to fig. 5.9) and for testing on fibers. For those tests the fibers were placed instead of the sample, and the beam was coupled into the fiber core. The expectation was to get the back-scattered Raman and Rayleigh light out of the fiber and collect it with the collecting lens, thus omitting the stronger pump light, but the signal was too weak compared to the background noise. Therefore for fibers only

the third geometry was used, with the big disadvantage of having the main central peak in the spectrum, and the inability to measure fibers which are not transparent in the visible spectrum.

5.1.4 Calibration

For being able to recalibrate the spectrometer and realign the main laser, a alignment system was implemented consisting of a small He-Ne-laser with a nominal output power of 10mW at 632nm which has been coupled into the beam direction of the main laser. The main laser itself is an argon laser with a variable output power between 20mW and 10W, lasing at 514nm from Lixel laser, model 95. This setup has been also used for later test measurements of elements to show that the samples to be tested are in the correct position, and to position the guiding optics. The optics used for guiding the laser beam is shown in picture 5.5

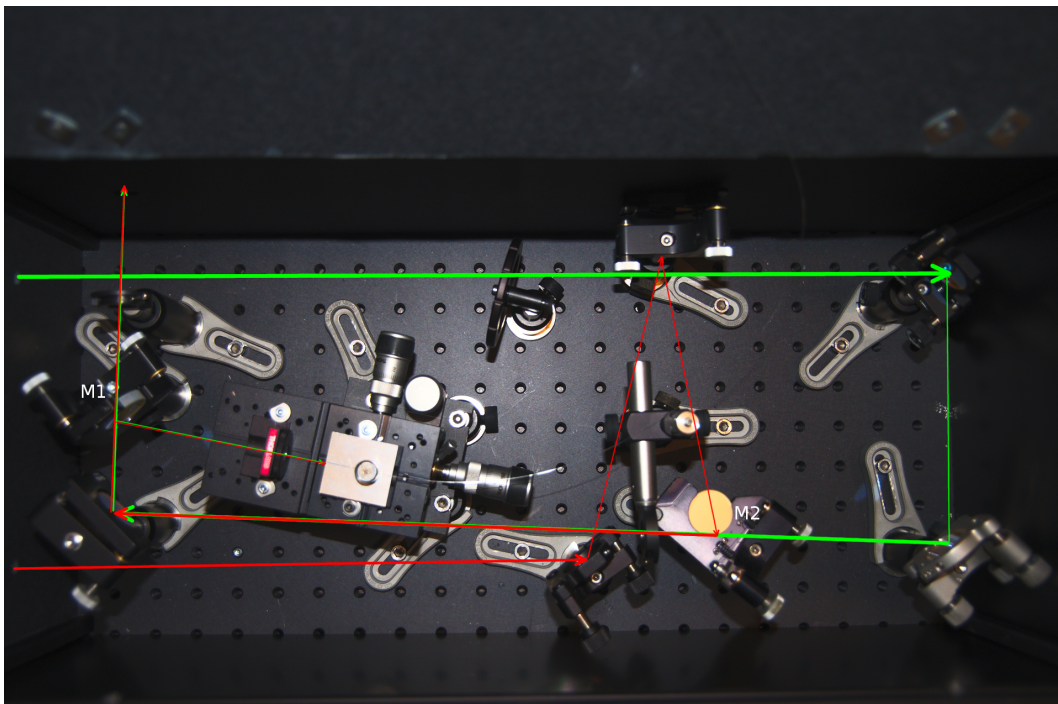


Figure 5.5: Laser guidance optics

This setup combined the two used lasers and allowed the user both to couple the light into a fiber with the coupling stage in the middle and direct it directly to the sample platform by flipping the mirror marked with $M1$. The mirror marked with $M2$ can be used to use either the red beam or the green beam, depending on its

position. Several tests with different materials were done, which are described in section 5.1.5. In order to calibrate the instrument, first the laser guidance optics was calibrated such that the red beam was in the same position as the green beam by using the diaphragms, and afterwards the red beam was used for the correct position of the sample. After switching to the PMT the position of the optics within the spectrometer were improved by looking at the highest intensity.

5.1.5 Test measurements

The first measurements were done with GSGG:Cr and GSAG:Cr to confirm that it is possible to get a reliable signal using the scattering geometry shown in fig. 5.4a. In this measurement the fluorescence property of the crystals was used, and resulted in the graph shown in fig. 5.6. The used laser was a gas-laser with a wavelength of 515.25nm. The used power was 200mW, and the slit width was set to 3mm.

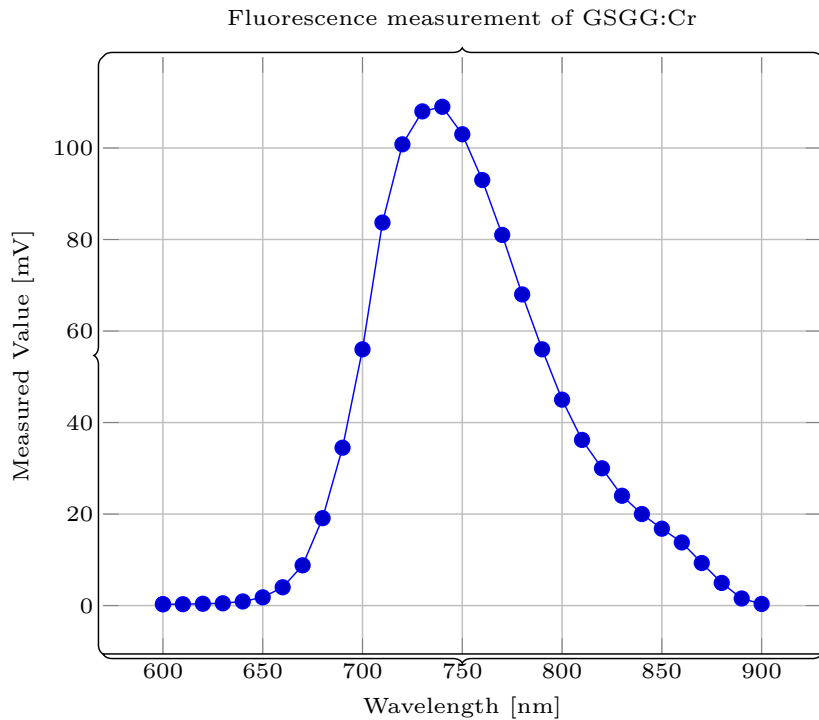


Figure 5.6: Fluorescence test measurement with GSGG:Cr

After thereby validating the functionality of the setup Raman signals should be measured. Among other materials such as magnesium fluoride (MgF₂) or calcium fluoride (CaF₂) diamond was the material with the most noticeable Raman response. For acquiring the spectrum the laser power was decreased to 100mW, the slit width of the spectrometer was set to 3mm and the maximum amplifying value of the lock-in-amplifier was set to 5mV. The whole spectrum is displayed in figure 5.7.

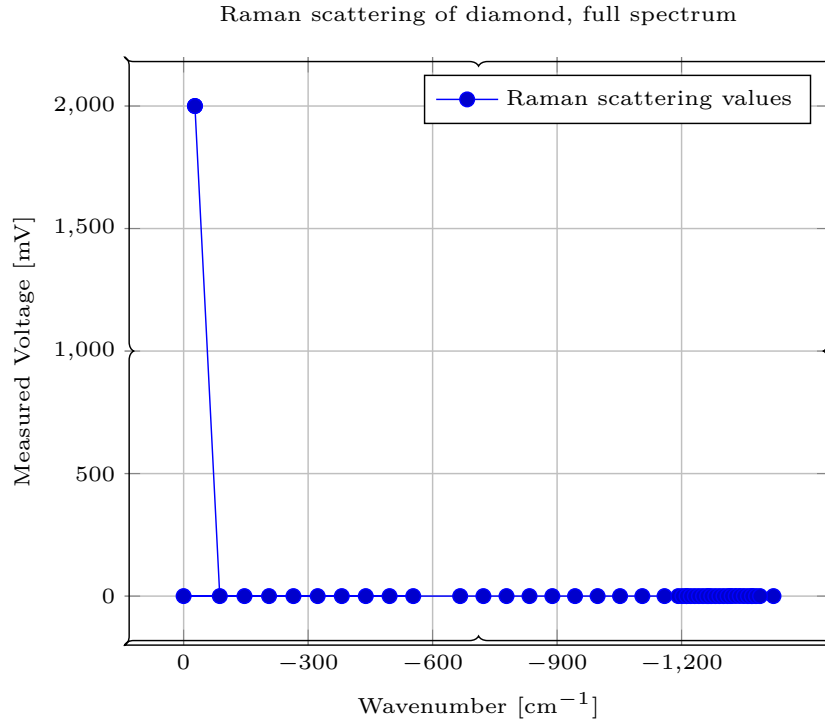


Figure 5.7: Raman measurement on diamond substrate, full spectrum

In this spectrum one can see that the peak at the central frequency of the laser is extremely noticeable, and therefore suppressing all other signals in the spectrum. Thus a single measurement was done at the position of the expected Raman peak, according to literature [55] at 1332cm⁻¹. The result can be seen in figure 5.8.

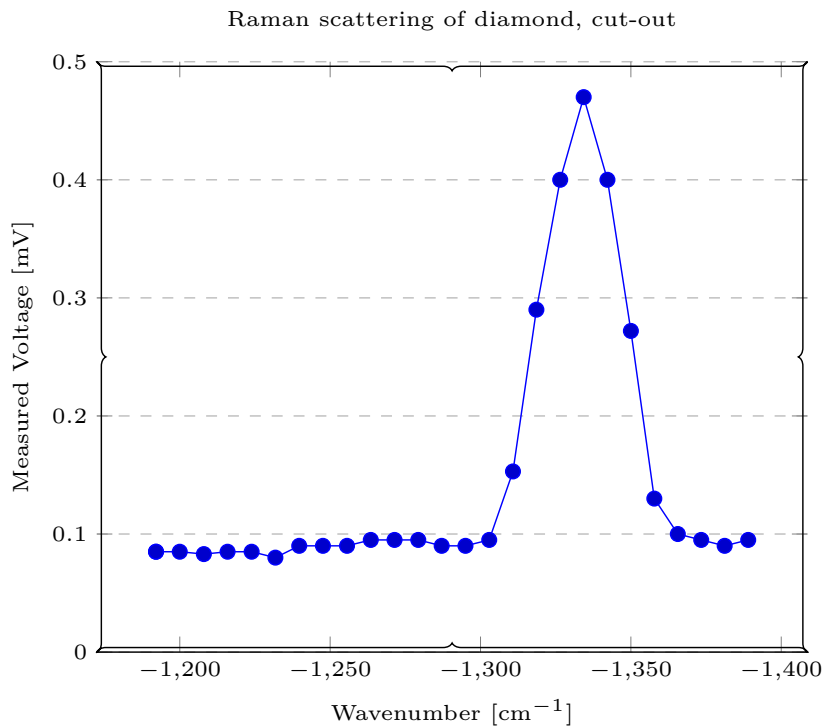


Figure 5.8: Raman measurement on diamond substrate, small spectrum

In this figure it can clearly be seen that even if diamond is quite a strong Raman signal generator [55] the signal is quite weak (approximately 5 times larger than the background signal). Thus the whole setup has to be further improved for measuring signals from other materials which give a lower Raman response. Those improvements included an improved optics for better focusing the laser onto the sample and recollecting the scattered light from the sample, but the most significant improvement was the automation of the setup, allowing the user measuring the signal at more points in the same range. Before that the user had to enter all values by hand, reading from a multimeter, which could become inconvenient for multiple points.

This is also the reason why all further measurements, beginning with fig. 5.9, provide a higher resolution than the measurements before.

To test the spectrometer with a second material as safety test silicon was chosen, after it produces a well-known Raman peak at 519cm^{-1} [56]. With this material the measurement resulted in the spectrum shown in fig. 5.9.

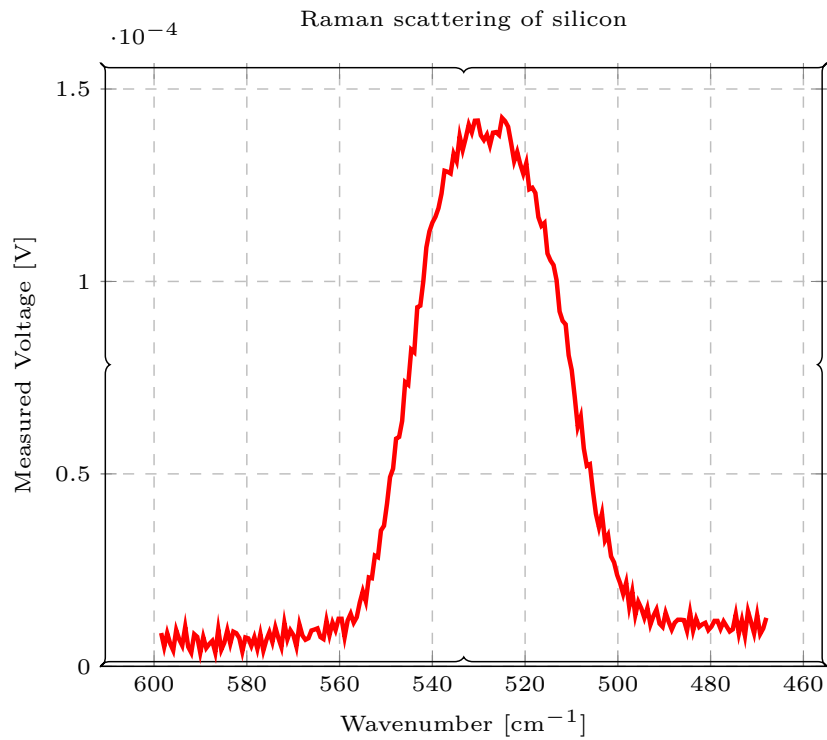


Figure 5.9: Raman measurement on silicon

Here a strong improvement compared to fig. 5.8 can be seen, especially in the Signal/Noise-ratio. While in the former the signal to noise-ratio is at around 5, the S/N-ratio is at around 120 in the latter one.

5.2 Automatisatation of the dispersion measurement setup

5.2.1 Setup

In order to measure the dispersion of fibers, a measurement setup was designed and built up. Its schematic is shown in figure 5.10.

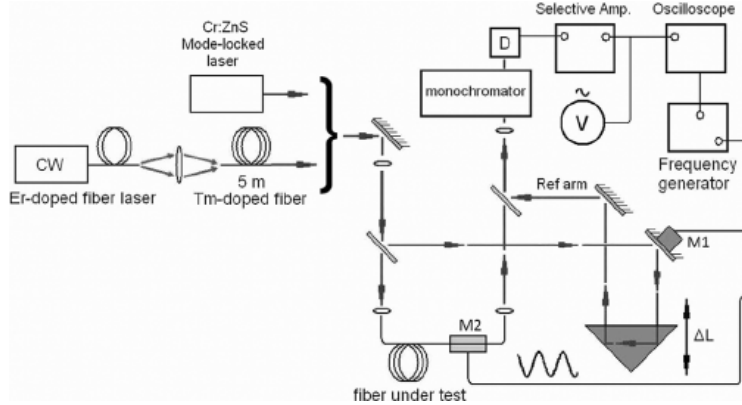


Figure 5.10: Schematic of the dispersion measurement setup [57]

This setup consists of a light source, two beam splitters, a movable 180° -mirror, the fiber itself, the monochromator and the PC. The function principle is that of a Michelson-Morley interferometer. Due to the path length difference of the light through the fiber and the mirror, one gets interferences. By adjusting the position of the mirror, the interference pattern gets either increased (by lowering the length difference) or decreased (by increasing the length difference). The light source itself should have a coherence length low enough to provide a noticeable decrease of the interference strength within the movement range of the mirror. Furthermore, in order to measure multiple wavelengths, the light source has to be a broadband light source. While the stepper motor and the spectrometer are controlled via the serial port in our setup, the line-in of the sound card of a computer was used in order to measure the amplitude of the current signal.

5.2.2 Calculation of the dispersion

In order to calculate the dispersion in dependence of the length of the path length difference, one has to start with the group velocity

$$V_g = \frac{c}{n} \cdot \frac{1}{1 - \frac{\lambda}{n} \frac{dn}{d\lambda}} \quad (5.1)$$

Furthermore, the time a pulse needs to travel through a fiber is

$$\tau = \frac{L \cdot n}{c} \cdot \left(1 - \frac{\lambda}{n} \frac{dn}{d\lambda} \right) \quad (5.2)$$

with n as the refractive index of the fiber and L as the length of the fiber. With those values the dispersion D can now be calculated as

$$D = \frac{1}{L} \frac{\partial \tau}{\partial \lambda} \quad (5.3)$$

$$= -\frac{\lambda}{c} \frac{d^2 n}{d\lambda^2} \quad (5.4)$$

$$= \frac{1}{L \cdot c} \cdot \frac{d}{d\lambda} \Delta l(\lambda) \quad (5.5)$$

By now measuring the position of the point where the highest intensity occurs one can determine the dispersion for the fiber for one specific wavelength, and by measuring the dispersion at different wavelengths one obtains the dispersion curve in this area. The acquisition of those values is easier if the light source covers a broad wavelength bandwidth due to the unnecessary to change the light source while conducting multiple measurements.

5.3 Summary

In this chapter the process of redesigning the control electronics and software for a Raman spectrometer (section 5.1) is described, including descriptions of the used electronics (section 5.1.1) and the software (section 5.1.2). In order to test the spectrometer several tests were done including the measurement of fluorescence and Raman scattering (section 5.1.5). In addition to those measurements three different scattering geometries were tested, and according to their properties used for the different samples. Additionally a setup for measuring the dispersion of fibers was automatized and test measurements were done (section 5.2). A goal which could not be fulfilled with the scattering geometries was to measure glasses due to problems with collecting the scattered light. The first two geometries were tested for measuring the Raman signal of bulk glass samples, but the resulting scattered light was below the signal strength of noise. Thus this part still has to be improved by testing further geometries, or by adding focusing/collecting mirrors. A second experimental part of the thesis is also briefly explained, the dispersion setup for measuring the dispersion of fibers. Its basic working principle is explained, and the formulas for calculating the dispersion curve out of the measurement values is introduced.

Chapter 6

Practical applications and results

In this chapter both the measurements of dispersion and raman measurements on fibers are presented and evaluated. Furthermore the two simulation scripts are described and the results from the simulations are presented.

6.1 Measurement of the dispersion of a fiber

Due to technical problems only two dispersion spectra for the same wavelength for a standard silica fiber SMF-28 could be obtained. Those are displayed in fig. 6.1.

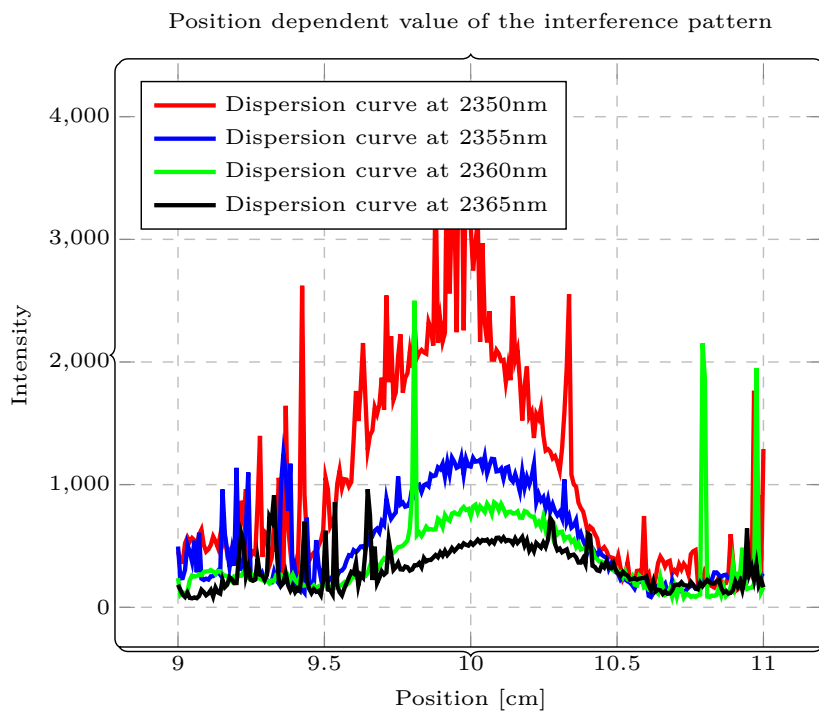


Figure 6.1: Position curves of the interference pattern of the dispersion setup

While the blue curve is quite noisy, the red (second) measurement is quite perfect, and was used for an approximative fit with a gaussian function

$$A \cdot \exp\left(-\frac{(x - b)^2}{2 \cdot c^2}\right)$$

with the values $A = 2.55014520 \cdot 10^3$, $b = 9.93966063$ and $c = 3.18258636 \cdot 10^{-1}$. The result is displayed in fig. 6.2.

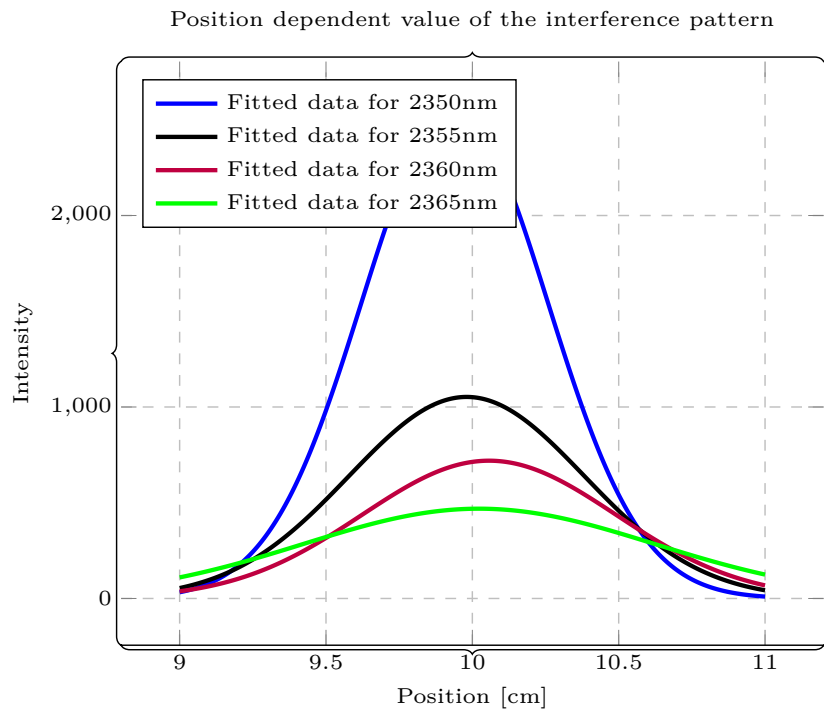


Figure 6.2: Measured and fitted data for the dispersion curve measurement

The script used for finding the best position can also be applied for all further measurements, and therefore increase the speed of the creation of the dispersion curve. The maximum points for those first measurements are displayed in fig. 6.3. Even if there are not enough for a whole dispersion curve those points demonstrate that the setup is theoretically working, even with its major flaws.

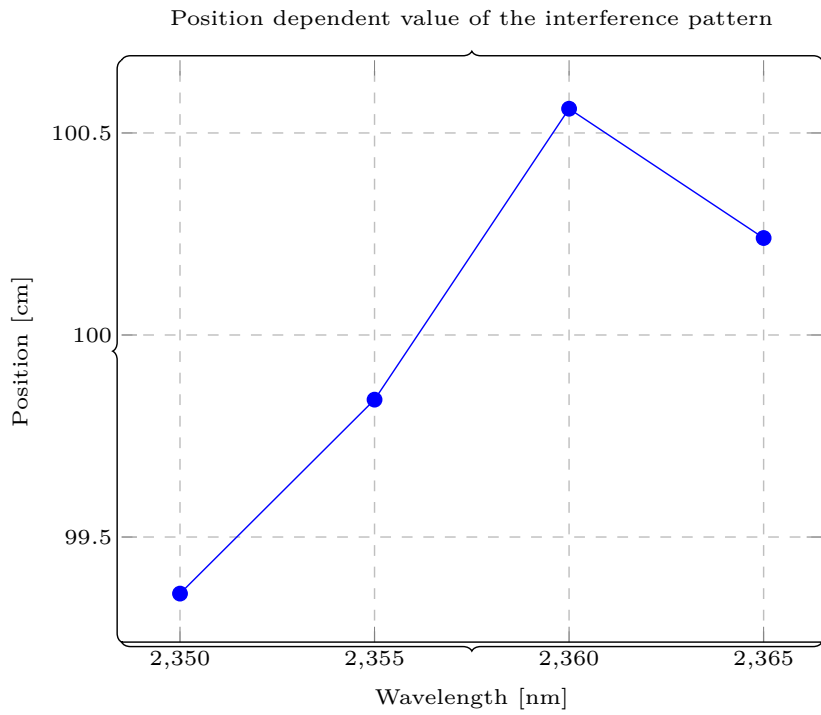


Figure 6.3: Proof of concept of the dispersion measurement setup

6.2 Measurement of the Raman shift in a fiber

After being able to show that the Raman setup is working (section 5.1.5) by scanning the Raman scattering of silicon (fig. 5.9) and diamond (fig. 5.8) the setup was converted in order to be able to measure fibers. For that a fiber coupling instrument was placed in the optical setup as seen in fig. 5.5, and the output of the fiber was attached at the entrance of the spectrometer. In order to align the fiber and to couple the light into the fiber the red laser was used, but for measurements the green laser was used. The first measurements were done on a silica-based fiber (SMF-28) with a length of approximately 2.5m. This resulted in the spectrum shown in fig. 6.4.

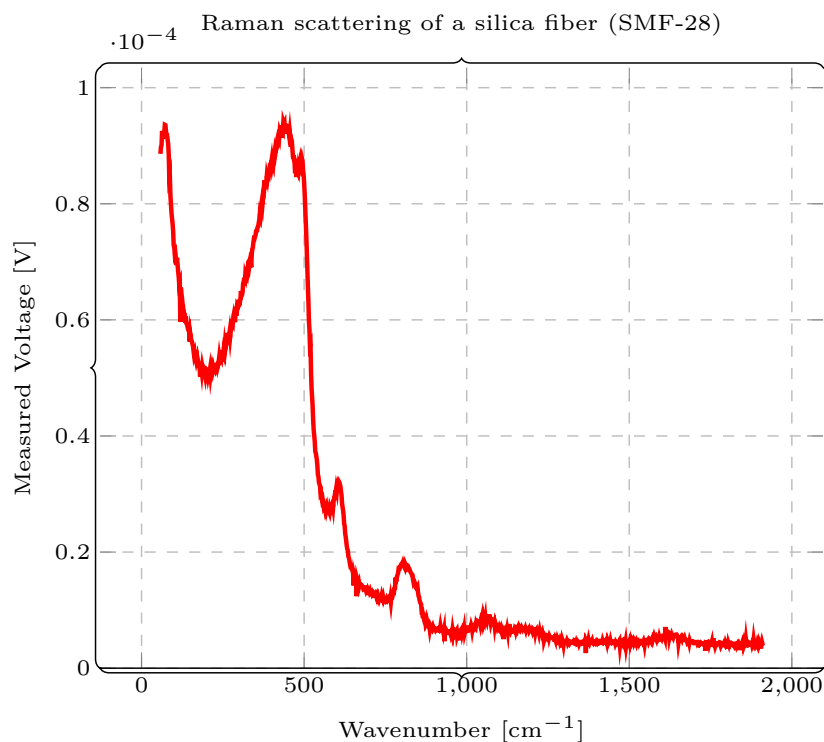


Figure 6.4: Raman gain of a silica fiber

It was generated with a laser power of 100mW and a slit width of 3mm. One can clearly see that in comparison with common spectra of silica the remaining part of the main peak at the left side can be seen. This peak occurred in all measurements, thus it had to be removed. In order to do that the measured spectrum first was approximated by a lorentzian function, followed by a subtraction of the function from the measurement. The result was used to determine the shape of the pulse, and

to design a function of the pulse shape to be used with other measurements. In order to determine the accuracy of the measurement, and to compare the scattering result in a fiber with the Raman scattering in glass, data for both is shown in fig. 6.5.

Raman scattering of a silica fiber (SMF-28) compared to the Raman scattering of silica glass [58]

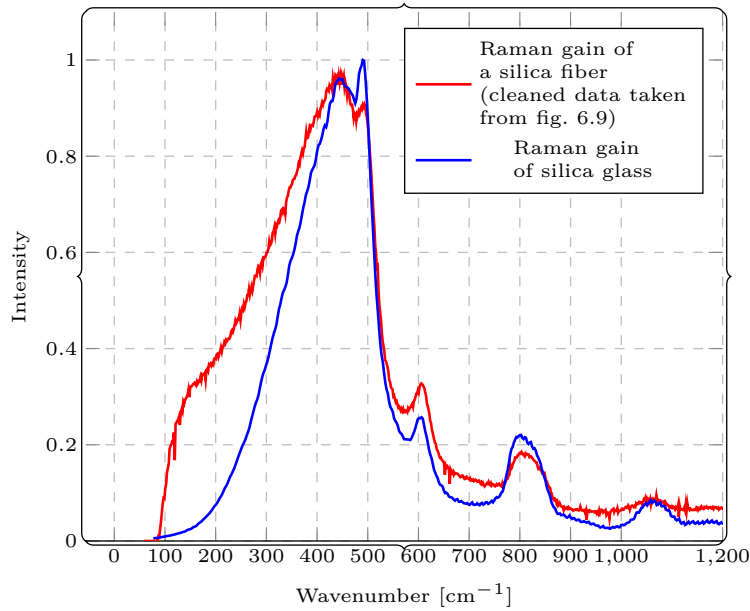


Figure 6.5: Comparison of the Raman scattering in a silica fiber vs the Raman scattering in silica glass

In this figure one can clearly see that even if the main peaks are at the same position for both materials, fiber and glass, the shape is different. The reason for the flatter right flank of the fiber spectrum can be that the central Rayleigh peak is not filtered out enough, and is still contributing to the measured spectrum. This can also be the reason for the bigger peak at $\approx 490\text{cm}^{-1}$. Another possible influence can be that the slit width of the spectrometer was set to the maximal width in order to increase the gained signal. Those probable error sources can be ruled out by further measurements.

A second fiber which has been measured was a germanate fiber. Here it was noticed that even if the coupling factor of light coming out of the fiber compared to the light going towards the entrance factor was at $\approx 5\%$ compared to $\approx 50\%$ for the silica fiber, the resulting spectrum was significantly higher (20 – 30 times higher). The single spectrum for the germanate fiber is shown in fig. 6.6. The length of both fibers was approximately the same at $\approx 2\text{m}$. In this spectrum one can see that the main peak (as expected) is at 420cm^{-1} , a main line of germanium [59].

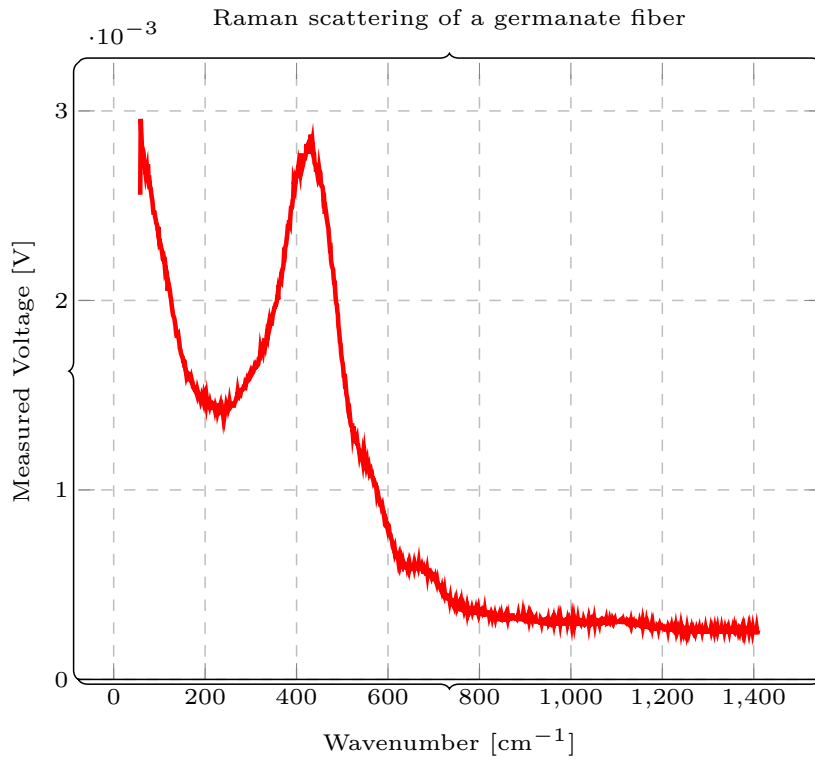


Figure 6.6: Raman gain of a germanate fiber

If both spectra are compared, one can see that several of the smaller peaks of the silica fiber are not present in the germanate fiber (compare to fig. 6.7). Furthermore one can see that the main peak of the germanate fiber is significantly sharper than the germanate peak, but this can also be explained by the smaller slit width of the germanate measurement, which increased the resolution.

Raman scattering of a silica fiber (SMF-28) compared to a germanate fiber

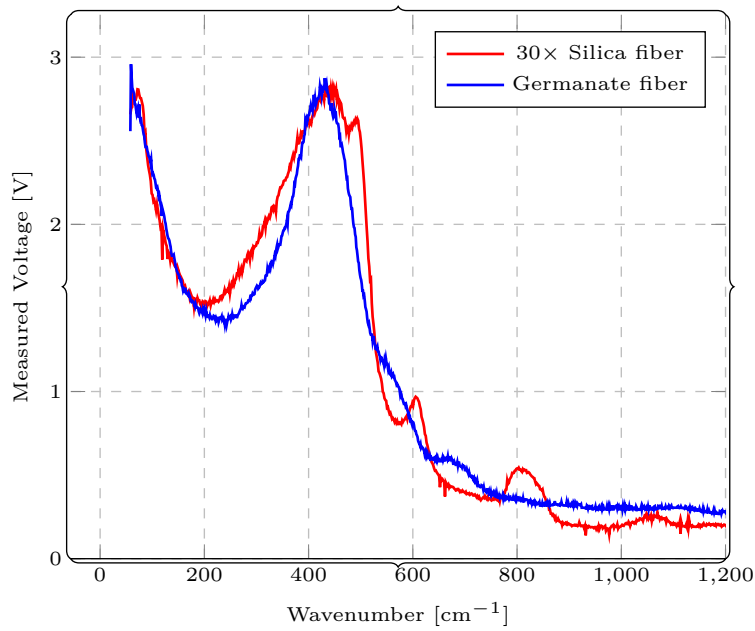


Figure 6.7: Raman gain of a silica and germanate fiber in comparison

6.2.1 Calculation of the Raman response function of the silica fiber

In order to calculate the Raman response function from the Raman gain, the data had to be fitted. This was done for the results of the silica fiber measurement by using a combination out of eighth lorentzian functions:

$$L(x, a, b, c, d) = a + \frac{\frac{b}{\pi}}{1 + \left(\frac{x-c}{d}\right)^2} \quad (6.1)$$

$$f(x, n_i, a_i, b_i, c_i, d_i) = \sum_{i=1}^8 n_i \cdot L(x, a_i, b_i, c_i, d_i) \quad (6.2)$$

The parameters used for eq. (6.2) are displayed in table 6.1.

i	1	2	3	4
n	2.819	-5.726	-1.955	$-2.100 \cdot 10^{-1}$
a	$2.180 \cdot 10^{-2}$	$2.375 \cdot 10^{-2}$	$2.281 \cdot 10^{-2}$	$2.198 \cdot 10^{-2}$
b	-1.700	-3.051	$-2.344 \cdot 10$	-1.188
c	$2.284 \cdot 10^2$	$2.342 \cdot 10^2$	$5.907 \cdot 10^2$	$8.003 \cdot 10^2$
d	$1.263 \cdot 10^2$	$1.969 \cdot 10^2$	$6.642 \cdot 10$	$1.854 \cdot 10$
i	5	6	7	8
n	$6.068 \cdot 10^{-1}$	1.874	3.936	$1.983 \cdot 10^{-1}$
a	$2.712 \cdot 10^{-2}$	$2.449 \cdot 10^{-2}$	$1.368 \cdot 10^{-2}$	$2.063 \cdot 10^{-2}$
b	1.070	$-6.874 \cdot 10^{-1}$	$-1.206 \cdot 10$	1.136
c	$4.963 \cdot 10^2$	$7.011 \cdot 10^2$	$5.897 \cdot 10^2$	$8.319 \cdot 10^2$
d	$-1.504 \cdot 10$	$-3.501 \cdot 10^2$	$6.871 \cdot 10$	$2.038 \cdot 10$

Table 6.1: Parameters used for fitting the normalized data in fig. 6.4 by using eq. (6.2)

The original data (normed to 1) and the fitted data is displayed in fig. 6.8. The corresponding R^2 -value is 99.80% indicating a quite good fit. Nevertheless one has to notice that on the one hand the peak at approximately 1200cm^{-1} is not fitted, and the leftmost peak resulting from Rayleigh scattering is also fitted. In order to find the influence of those two misfits the Raman response function was calculated by using eq. (4.80) and eq. (4.81).

Raman scattering of a silica fiber (SMF-28) compared to the fit using eq. (6.2)

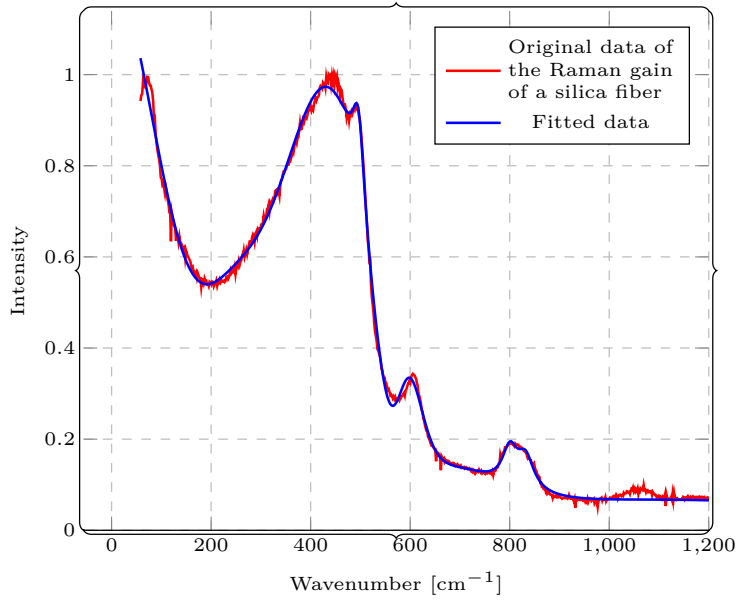


Figure 6.8: Comparison of fitted data of the Raman gain of a silica fiber vs the original data

In order to remove the Rayleigh peak the laser peak was approximated by a Lorentzian function, and the function subtracted from the experimental data. The result is shown in fig. 6.9, together with the new fit, and a comparison to the „dirty“ original experimental data.

Raman scattering of a silica fiber (SMF-28) with and without Rayleigh peak

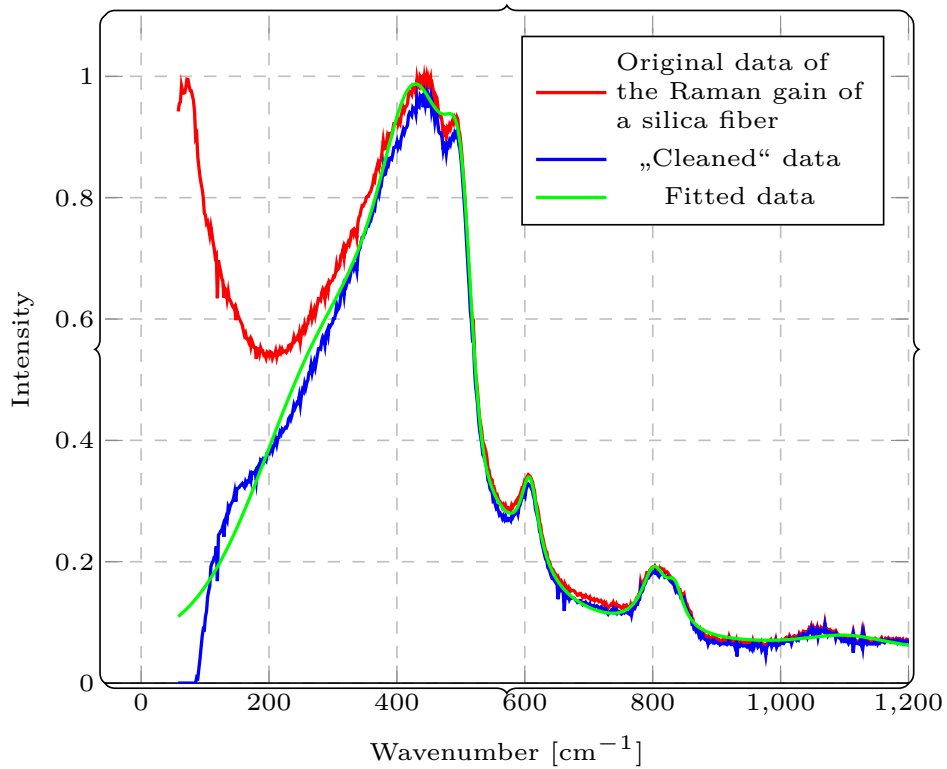


Figure 6.9: Comparison of fitted data of the Raman gain of a silica fiber vs. the original data without the Rayleigh peak

The resulting Raman response functions are shown in fig. 6.10

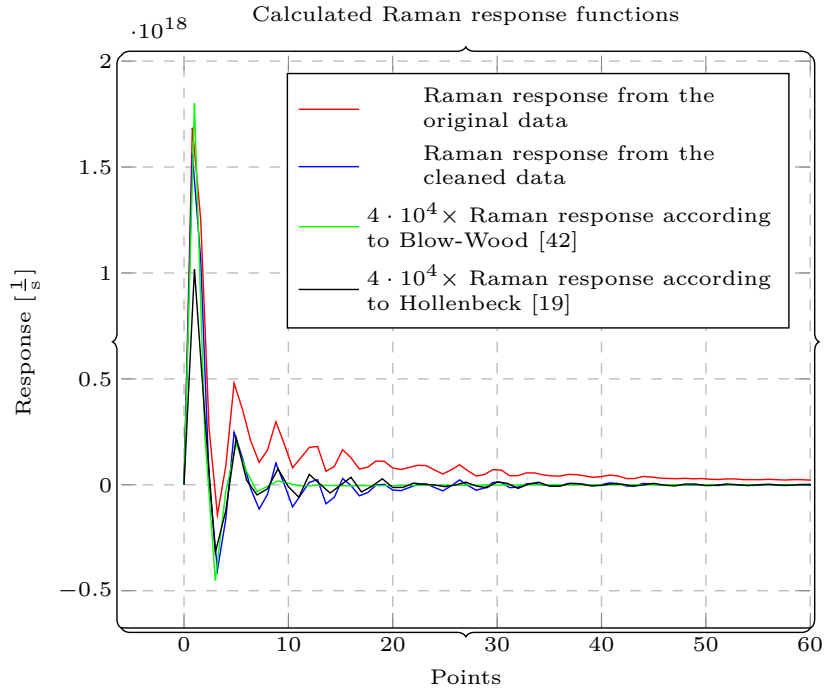


Figure 6.10: Calculated Raman response in comparison with an approximative formula

In this comparison between the calculated Raman response both response functions calculated from the measured data, cleaned and uncleaned, and two Raman response approximation functions from Blow-Wood and from Hollenbeck are shown. Here one can see that even if the „uncleaned“ function has a certain offset (probably resulting from the center line) all peaks are approximately at the same position, indicating a good accordance of theoretical and measured data . The reason for the big multiplication factor for the theoretical values could be that the Fourier transformation was done numerically with a relatively low number of points. This results both in a low resolution, which is also responsible for the sharp edges, instead of „round“ peaks, and in a not-perfect multiplication factor.

6.2.2 Calculation of the Raman response function of the germanate fiber

In order to calculate the Raman response function of the germanate fiber, one has to do the same procedure as described in section 6.2.1. First the resulting spectrum (shown in fig. 6.6) has to be cleaned from the Rayleigh peak. For that a Lorentzian approximation of the initial pulse (as above) will be used. The result (including the fitting function) is shown in fig. 6.11.

„Cleaned“ Raman gain in comparison with the original result and fitting function

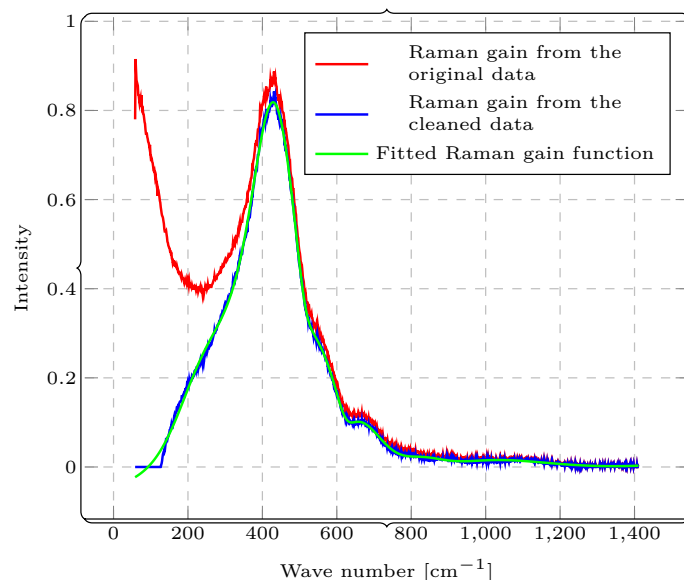


Figure 6.11: Raman gain of a germanate fiber, processed

The resulting Raman response function both for the gain measurement with Rayleigh scattering and without is shown in fig. 6.12.

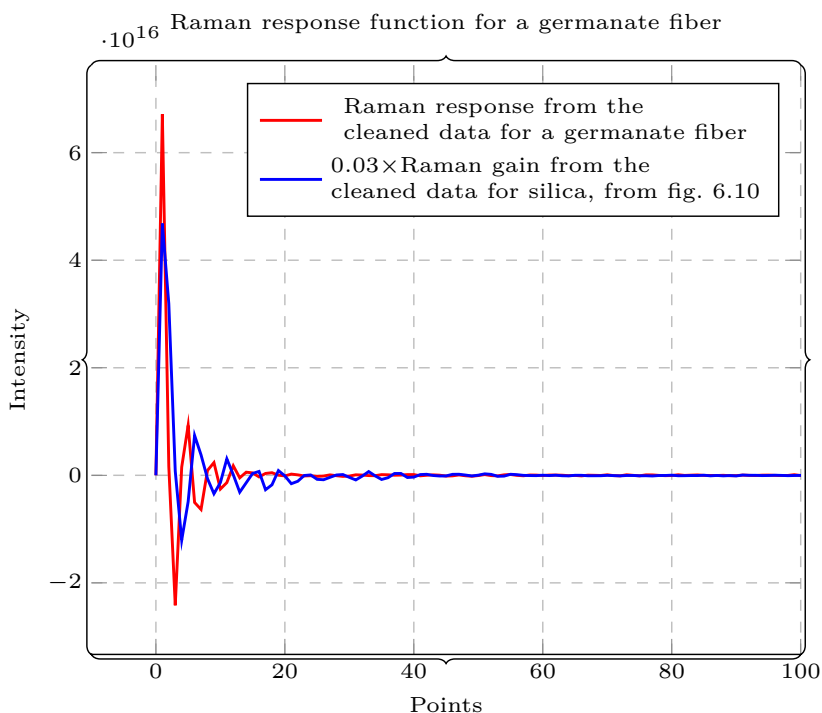


Figure 6.12: Calculated Raman response in comparison with an approximative formula

In this figure one can clearly see that the Raman response function from the germanate fiber is on the one hand slightly shifted compared to the Raman response function in the silica fiber, and on the other hand significantly larger. A physical reason for this behaviour could not be determined yet, but it could also be related to the Fourier transformation and resulting prefactors.

6.3 Fiber simulations

6.3.1 Simulation program

As already explained in the theory part (section 4.2.1) we have to solve the GNLSE by using the Split-Step-Method for both simulating a moving soliton in a fiber and the generation of a supercontinuum. This algorithm can be implemented in an easier way by rewriting it into a PDE:

In [25] the authors propose a potential algorithm implemented in matlab to solve the GNLSE ([25], Chapter 3, Listing 3.1). This code has already been implemented

in python, and therefore I could use this code([60], [61]). For my purposes I modified this code for improved output data. Before talking about the calculation results and the used method in the simulation, first some parts of the program should be presented.

Raman response functions

In literature several different Raman response functions can be found. Those are already listed in the section 4.1.7.3. The implementation of the most important function, the „Blow-Wood“-function is:

```
def Raman_blowwood(tvec):
    tau1 = 12.2e-15
    tau2 = 32.0e-15
    tvec2 = np.multiply( tvec, tvec>=0) # using tvec2 prevents
    ↪ numerical issues for big negative times with exp
    rt = (tau1**2 + tau2**2)/(tau1 * tau2**2) *np.multiply( np.exp(-
    ↪ tvec2/tau2), np.sin(tvec2/tau1))
    rt = np.multiply( rt, tvec>=0)
    return rt
```

Figure 6.13: Blow-Wood-function, implemented in python

The function takes a vector of τ -values, and returns a vector of the processed τ -values.

Reformulation of the GNLSE in python

To be able to solve the GNLSE numerically with the computer it has to be reformulated. This has already be done in equation 4.85:

$$\frac{\partial \tilde{A}}{\partial z} = i \frac{\gamma \omega}{\omega_0} \exp(-\hat{L}z) \cdot \mathcal{F} \left\{ A(z, t) \cdot \left((1 - f_R) |A(z, t)|^2 + f_R \Delta t \mathcal{F}^{-1} \left[\mathcal{F}(h_R(t)) \mathcal{F}(|A(z, t)|^2) \right] \right) \right\}$$

Thus, the final function for the right hand side of equation 4.85 is

```

def GNLS_RHS( z, AW, simp):
    AT = np.fft.fft( np.multiply( AW , np.exp( simp['linop'] * z)))
    IT = np.abs(AT)**2
    if simp['Raman'] == True:
        RS = simp['dt'] * np.fft.fft( np.multiply( np.fft.ifft(IT),
            ↪ simp['RW'] ))
        M = np.fft.ifft( np.multiply( AT,( 1-simp['fr'])*IT + simp['
            ↪ fr']*RS ) )
    else:
        M = np.fft.ifft( np.multiply( AT, IT))
    return 1.0j * simp['gamma'] * np.multiply( simp['W'], np.multiply(
        ↪ M, np.exp( -simp['linop'] * z)) )

```

Figure 6.14: Formula for calculating the right hand side of the equation 4.85, written in python

6.3.2 Fiber simulations

6.3.2.1 Simulation of a moving soliton in a fiber

For simply simulate a moving soliton without Raman effects, the Raman part of the right hand side of the formula 4.85 has to be disabled. That leads to the shortened function

$$\frac{\partial \tilde{A}}{\partial z} = i \frac{\gamma \omega}{\omega_0} \exp(-\hat{L}z) \cdot \mathcal{F} \left(A(z, t) \cdot |A(z, t)|^2 \right) \quad (6.3)$$

which still can be solved with the same solver. As example a fiber with the values $l = 50\text{cm}$, $\beta_2 = -10 \cdot 10^{-27}$ and $\gamma = 2.1 \cdot 10^{-2}$ was chosen, with an input pulse with a power of $P = 7.6\text{J}$ and a length of $T = 2.5 \cdot 10^{-13}\text{s}$. The central wavelength is $1064\mu\text{m}$. The result can be seen in figure 6.15. The pulse power itself is calculated with eq. (6.4).

$$P = \frac{|\beta_2|}{T_0^2 \cdot \gamma} \quad (6.4)$$

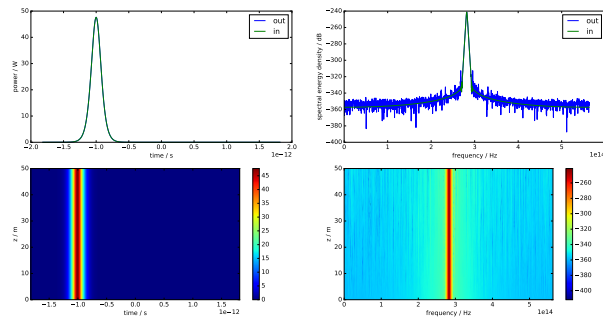


Figure 6.15: Simple soliton calculation

If the Raman effect is enabled, the soliton is shifted due to the Raman effect, which is shown in fig. 6.16.

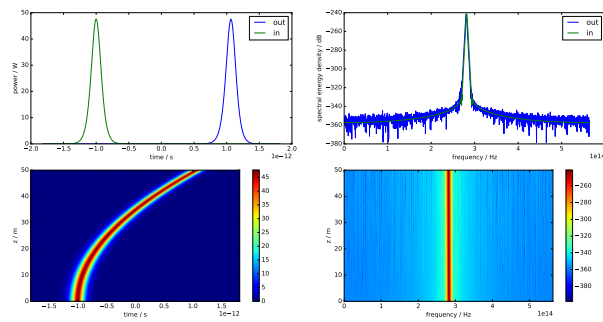


Figure 6.16: Raman shift of a soliton

6.3.2.2 Simulation of the generation of a supercontinuum in a fiber

To simulate the supercontinuum generation now additional β -values have to be added. For showing the significance of the different β -values they were added stepwise. For that $n_2 = 1.3375 \cdot 10^{-20}$ was chosen, and the simulated values from table 6.3. Thus one receives the graphs shown in fig. 6.17. In this figure can see the influence of the

Comparison of the influence of different β -values onto the supercontinuum of a fiber

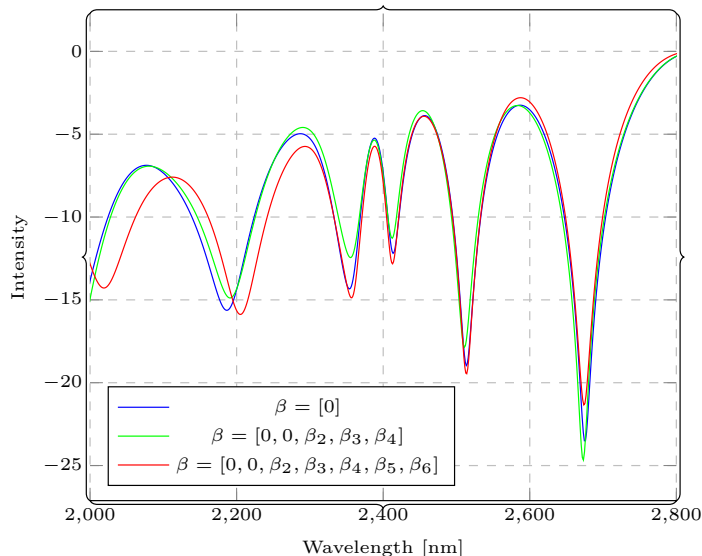


Figure 6.17: Comparison of the influence of different β -values towards the supercontinuum in a fiber

different β -values. All spectra are displayed in the frequency domain, with a central frequency of 2390nm of the input pulse (not drawn here). Here one can notice that the influence of the β -values is visible, but especially at the central point not that significant. Nevertheless the further one move outside towards the higher frequencies, the bigger the influence of the additional β -values get.

To investigate the influence of the refraction index n_2 several spectra also were created with different n_2 -values, while keeping the β -values constant. In this example the n_2 -values are shown in table 6.2.

For comparison the β -values where set to $\beta = [\beta_2, \beta_3, \beta_4, 0, 0]$. Thus one receive fig. 6.18.

$n_{2,1}$	$0.5 \cdot 1.3375 \cdot 10^{-20}$
$n_{2,2}$	$1 \cdot 1.3375 \cdot 10^{-20}$
$n_{2,3}$	$2 \cdot 1.3375 \cdot 10^{-20}$
$n_{2,4}$	$5 \cdot 1.3375 \cdot 10^{-20}$
$n_{2,5}$	$10 \cdot 1.3375 \cdot 10^{-20}$
$n_{2,6}$	$20 \cdot 1.3375 \cdot 10^{-20}$

Table 6.2: Used n_2 -values for comparison

Comparison of the influence of different β -values onto the supercontinuum of a fiber

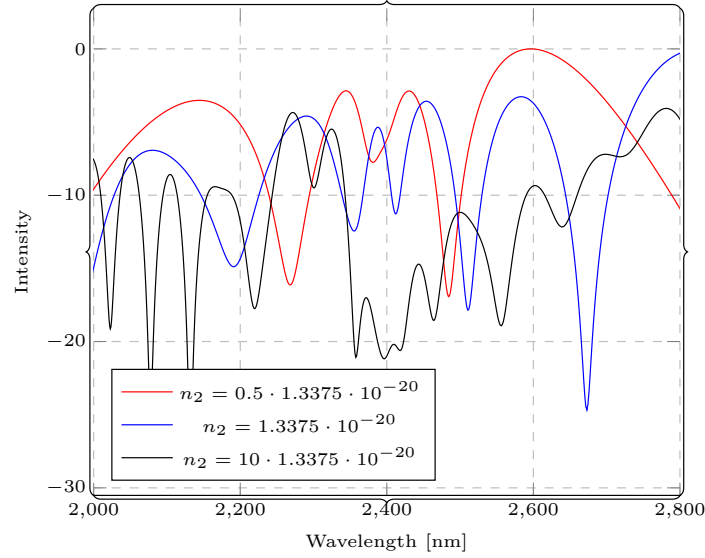


Figure 6.18: Comparison of the influence of different n_2 -values towards the supercontinuum in a fiber

Here one can see that even small changes of the value of n_2 have significant influences onto the resulting pulse shape, especially if compared to fig. 6.17. In order to keep the figure understandable, not all values for n_2 are displayed. Therefore the proper calculation of the nonlinear refraction index can be seen as way more important than the proper calculation of the additional β -values if the area of interest is close to the main pumping line.

6.3.3 Comparison of the simulation results with the measured data

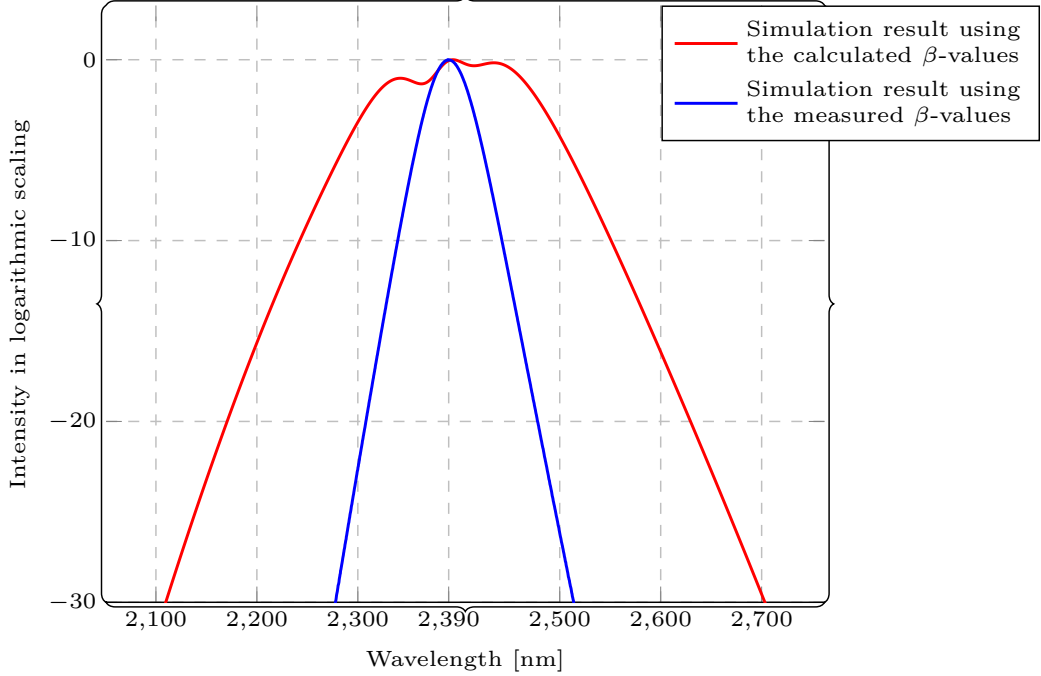
During the experimental simulations several simulations were done to determine the importance of both the β -values and the n_2 -value. Furthermore the importance of

the attenuation and its influence onto the resulting shape of the pulse was tested. The first important step was to get reliable β -values. The first intention was to use β -values obtained from real dispersion measurements from the fiber by deriving the β_2 -values further ($\beta_3 = \partial\beta_2/\partial\omega$, $\beta_4 = \partial^2\beta_2/\partial\omega^2$). This resulted in the values shown in table 6.3.

	Measured values	Simulated values
β_2	$7.31 \cdot 10^{-27} \frac{\text{s}}{\text{m}}$	$1.736 \cdot 10^{-26} \frac{\text{s}}{\text{m}}$
β_3	$-1.163 \cdot 10^{-19} \frac{\text{s}}{\text{m}}$	$3.665 \cdot 10^{-41} \frac{\text{s}}{\text{m}}$
β_4	$-2.316 \cdot 10^{-17} \frac{\text{s}}{\text{m}}$	$-2.887 \cdot 10^{-54} \frac{\text{s}}{\text{m}}$
β_5	$0 \frac{\text{s}}{\text{m}}$	$2.794 \cdot 10^{-67} \frac{\text{s}}{\text{m}}$
β_6	$0 \frac{\text{s}}{\text{m}}$	$1.630 \cdot 10^{-79} \frac{\text{s}}{\text{m}}$

Table 6.3: Measured and simulated β -values

By putting them into the simulation, we received the blue spectrum shown in fig. 6.19. Unfortunately these results were not as close to the real results A.15 as expected. Therefore those results were compared with the results obtained from the mode calculator in the rp-photonics program „fiber power“. Those values differ quite a lot from the values from the dispersion measurement, and are shown in table 6.3. When those β -values were used for the simulation of the supercontinuum, the resulting spectrum was much better, and is shown as the red spectrum in fig. 6.19.

Comparison of the measured β -values compared with the calculated β -valuesFigure 6.19: Comparison of the simulation results using the β -values from table 6.3

The reason for this big difference could not be determined, but one assumption for it is that it might result from a non-ideal measurement. Nevertheless this thesis can neither be confirmed nor denied as long as the measurements are not repeated, but until then the β -values obtained from the rp-photonics simulation were used. For each simulation an input pulse with a FWHM of 68fs and an energy of 0.68nJ was used, resulting in a peak power of 10kW of the laser pulse. To show the importance of the different values, several different n_2 -values in the appropriate range from $5 \cdot 10^{-21} \frac{\text{m}^2}{\text{W}}$ to $20 \cdot 10^{-20} \frac{\text{m}^2}{\text{W}}$ were chosen. To each of those n_2 -values β -values were added, beginning with only β_2 up to $[\beta_2, \beta_3, \beta_4, \beta_5, \beta_6]$. While the adding of only n_2 -values modified the size of the resulting output-pulse in the frequency domain, while adding β -values without n_2 -values modifies the shape of the resulting output-pulse in the time domain.

6.3.4 Comparison of both solving approaches (ODE and SSFM)

Even if this approach is easy to implement and straight forward, it still has the problem that it is quite slow, and not portable to other languages, after it relies

on the ODE45-solver of python. With the use of „gprof“, a profiling program, the slowest parts were tried to be identified. It showed up that the solver is one of the slowest functions next to the *GNLSE_RHS*-function (fig. 6.14). This prevented a significant speed-up, which was tried by implementing the function partly in C and coupling it to the python-program with Cython. This led to a theoretical speed-up of 2, but this speed-up is insignificant if comparing with the estimated time needed for calculating the first stage of the laser described in chapter 7 ($t \approx > 4 \cdot 10^{12}h$). Thus the split-step approach mentioned in section 4.2 was implemented for tests both in C and in python (based on the algorithms proposed in [46], in [47] or in [48]), but until the end of the thesis no simulation images were created. Nevertheless this approach increases the speedup significantly, leading to program execution times of seconds to minutes, even if not optimized for speed. The code for the SSFM- and RK4IP-method for solving the GNLSE was obtained from [62].

6.4 Summary

In this chapter the different practical applications are described. First the results from the dispersion measurement of fibers done with the setup described in section 5.2 are described, followed by the results of the Raman measurements of fibers done with the setup from section 5.1. Finally the results of the simulations of pulse propagation in fibers with different pre-settings are displayed and compared with the measurements in the experiment (section 6.3).

Chapter 7

Design of a laser using SPM

In order to use the calculated results in reality a final task was to improve a MOPA-laser which uses the SPM-effect in order to narrow the pulse bandwidth, and further to design a packaging to make it ready for shipping. A schematic of the laser is drawn in fig. 4.1.

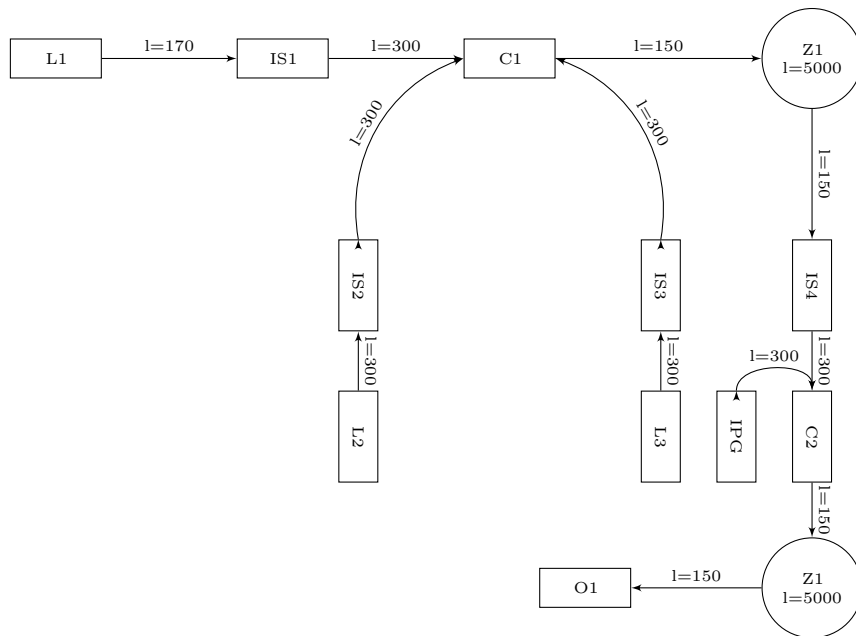


Figure 7.1: Basic layout of the laser, including distances in [mm]. Description of the parts is in table 7.1

It consists out of the main input laser L1, two additional support lasers (pumping lasers for the first stage) L2 and L3 and the big pumping laser IPG for the second pumping stage.

L1	Initial pulse laser
L2	Forward pumping laser for the first amplifying stage
L3	Backwards pumping laser for the first amplifying stage
IPG	Forward pumping laser for the second amplifying stage
IS1	Isolator for L1
IS2	Isolator for L2
IS3	Isolator for L3
IS4	Isolator between the first amplifying stage and the coupler C2
C1	Coupler between the amplifying lasers and the pulse laser
C2	Coupler between the first amplifying stage, the second amplifying stage and the IPG-laser
Z1	Cylinder used for holding and cooling the first and second amplifying stage
O1	Laser output

Table 7.1: Description of the parts used in figure 7.1

The main input laser L1 is pulsed, and creates an average output of 4mW at a frequency of 100kHz, thus having a peak power of 600mW. Its pulse width is 0.45nm at FWHM, and its operating wavelength is 1550nm. A pulse spectrum of the laser is shown in fig. 7.2

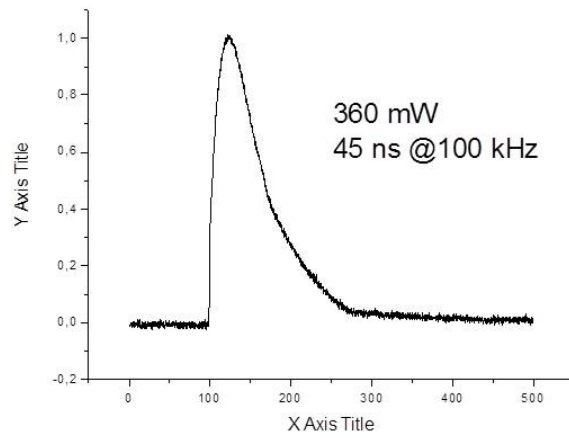


Figure 7.2: Pulse spectrum of laser L1

The lasers L2 and L3 are used for pumping the first amplification stage. Both are operating at 1480nm with a power of 300mW in continuous mode. Their respective spectrum is shown in fig. 7.3.

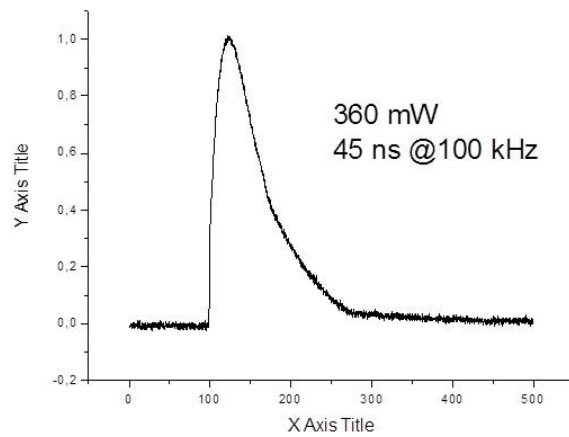


Figure 7.3: Pulse spectrum of laser L2 and L3

The pumping laser for the second amplification stage, L4, is operating at a wavelength of 975nm with a pulse-FWHM of ≈ 3.2 ns in the temporal regime and ≈ 0.4 nm in the wavelength dimension. With an average power of 10W that results in a peak energy of $100\mu\text{J}$. The obtained spectrum of the laser is shown in fig. 7.4.

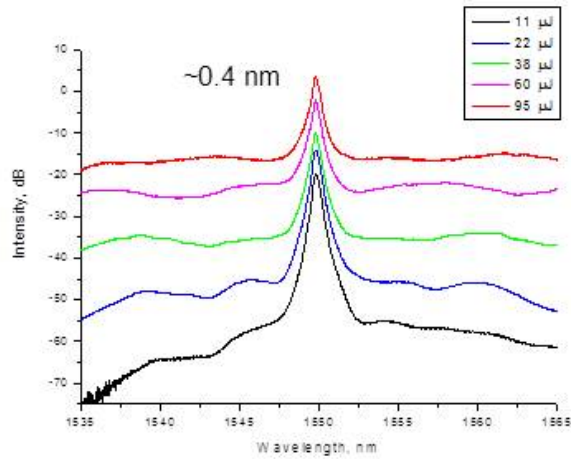


Figure 7.4: Pulse spectrum of the whole fiber laser

7.1 Packaging of the laser

An additional task during my master thesis was to design and build a housing case for a fiber laser. The case was first designed in SolidWorks and then tested and simulated for sufficient airflow by calculating the corresponding values (sections A.6.1 and A.7). Based on this results a second generation of the packaging was generated, resulting in a smaller and lighter package with improved features such as temperature range and stability. This process is described in appendix A.6.2 and in appendix A.6.3 in the appendix.

7.2 Summary

In this final chapter the application of the results achieved in chapter 6 and chapter 4 in a short-pulse laser with SPM is described. Furthermore a packaging (appendix A.5) for this laser was designed in two steps, including the calculation of the thermal distribution and the airflow necessary for cooling (appendix A.6.1), followed by improvements of the design leading to several build configurations.

Chapter 8

Summary

In this thesis several different aspects of nonlinearity were taken a look at, with Raman scattering as the biggest one. On the one hand those nonlinearities were simulated and their influence onto the light pulse were observed, and on the other hand those nonlinearities were measured. For this purpose two measurement setups were redesigned and newly constructed, one for measuring the Raman gain of materials, and the other one for measuring the dispersion of fibers. For both measurement places new devices had been designed and controlling programs written. With those setups already known data was confirmed, such as the Raman gain function for silica fibers, and new data was acquired which has not been measured before, such as the Raman response and the Raman gain for a germanate fiber.

Unfortunately the dispersion setup still needs some improvement, after it was not possible to use it as intended in this thesis due to the technical failure of the stepper motor.

For the future both setups can be used for measuring further unknown data or confirm known data, such as the Raman spectrum of ZBLAN-fibers, Chalcogenide fibers, or custom self-made fibers. The improvements of the setups allows it to increase the speed of the measurements and the accuracy, while administrating the measurements remotely, and therefore increasing the working speed.

If the PMT used in the Raman measurements is changed with a PMT sensitive in the infrared area, the same experimental setup can also be used for measuring fibers which are only transparent in the infrared area, such as chalcogenide fibers. Nevertheless the pumping laser also has to be exchanged in this case, but it is possible to use the same coupling input.

Another possible improvement can be the improvement of the scattering geometries, allowing the user to also measure the Raman scattering of bulk glasses, which was not possible with the current geometries. Furthermore both setups can and have to be further improved, both in the user friendliness and usability by improving the programming itself and the controlling devices.

A final possible improvement can be done for the simulation program of the GNLSE by porting it to the GPU, and adding a user interface to it, thereby increasing its user friendliness.

Glossary

A/D Analog/Digital. 31, 32

ARM Advanced RISC Machines, name of a microprocessor architecture. 30

BBB BeagleBone Black. 34

DPC Digital Photon Counter. 31, 34

FWHM Full Width, Half Maximum. 61, 64, 66

FWM Four-Wave Mixing. iii, 6, 16, 17

GNLSE General Non-Linear Schrödinger Equation. iii, 3, 6, 9–11, 14, 15, 22, 25, 26, 28, 54, 62, 69

GPIO General Purpose Input-/Output. 30

GUI Graphical User Interface. 32, 34

GVD Group velocity dispersion. 6, 13

I²C Inter-Integrated Circuit, a serial databus used for communication between electronic devices. 31, 34

I\O Input\Output. 30

IRS Induced raman scattering. 6, 19

ISA Industry Standard Architecture. v, viii, 29, 30, 131, 132

LAN Local Area Network. 30–32, 34

MI Modulation instability. 17

MOPA Master Oscillator Power Amplifier. 63

NLSE Nonlinear Schrödinger equation. 6

- ODE** Ordinary differential equation. iv, 25, 28, 61
- PCB** Printed Circuit Board. 30, 96
- PDE** Partial differential equation. 54
- PMT** Photo Multiplier Tube. 31, 37, 69
- RK4IP** Runge-Kutta-4 in the Interaction Picture-method. 27, 62
- SIF** Step-index fiber. 12
- SPM** Self-phase modulation. iv, 5, 6, 13, 28, 63, 64, 66, 67
- SRS** Spontaneous raman scattering. 19
- SSFM** Split-Step-Fourier method. iv, 61, 62
- SSH** Secure Shell, a network protocol. 32, 34
- TCP** Transmission Control Protocol, a network protocol. 32
- USART** Universal Synchronous/Asynchronous Receiver/Transmitter. 32
- ZDW** Zero-dispersion wavelength. 13

Appendix A

Appendix

A.1 Code Listing

A.1.1 Python script for solving the GNLSE

<https://github.com/xmhk/gnlse>

A.1.2 Code for the controller boards

Cape

<https://github.com/anates/Cape>

Amplifier

<https://github.com/anates/PreAmp>

Stepper-Controller

<https://github.com/anates/StepperController>

A.1.3 Controller program - GUI

<https://github.com/anates/Spectro>

A.1.4 Controller program - remote

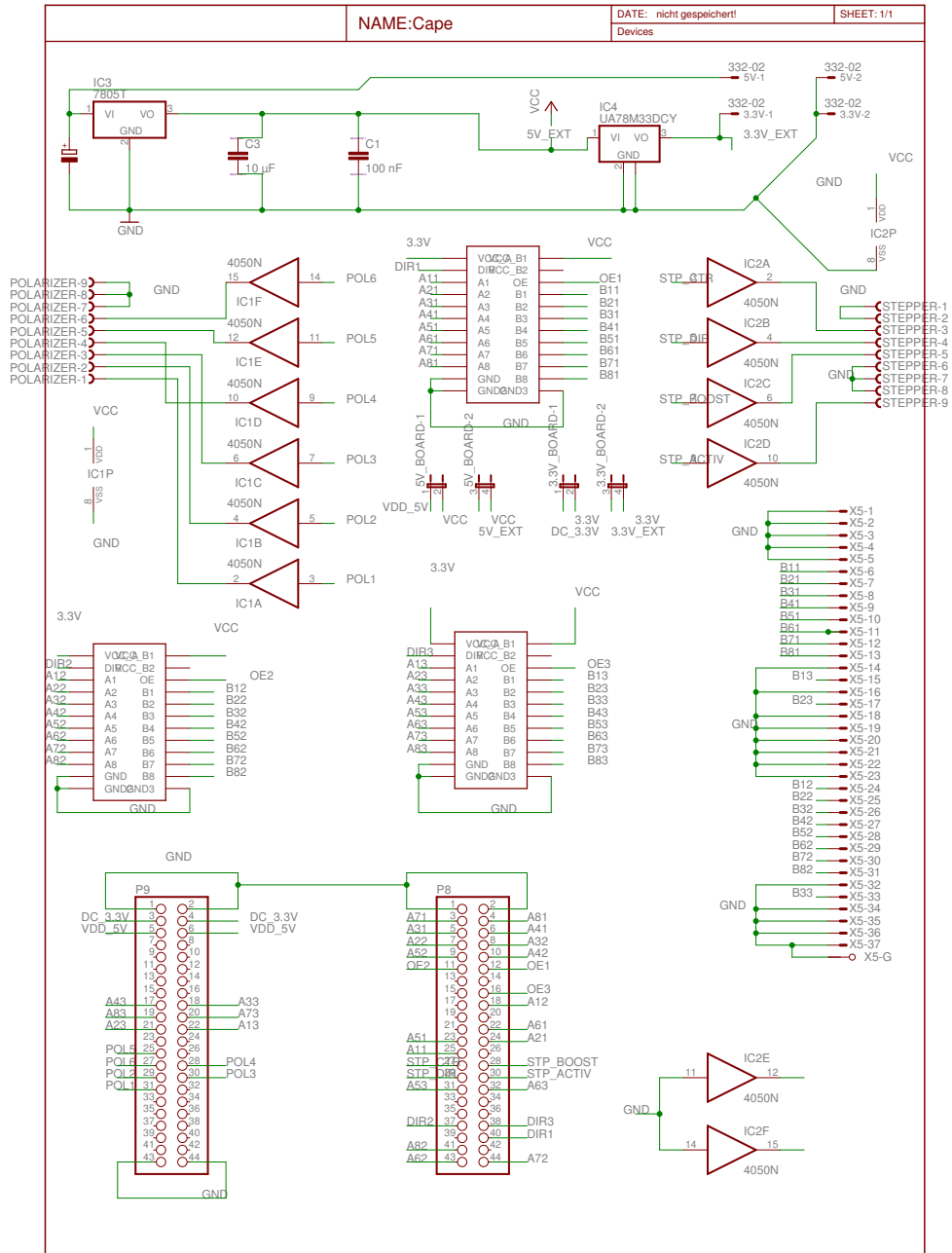
<https://github.com/anates/TCP-controller>
<https://github.com/anates/remoteController>

A.1.5 Controller for the dispersion setup

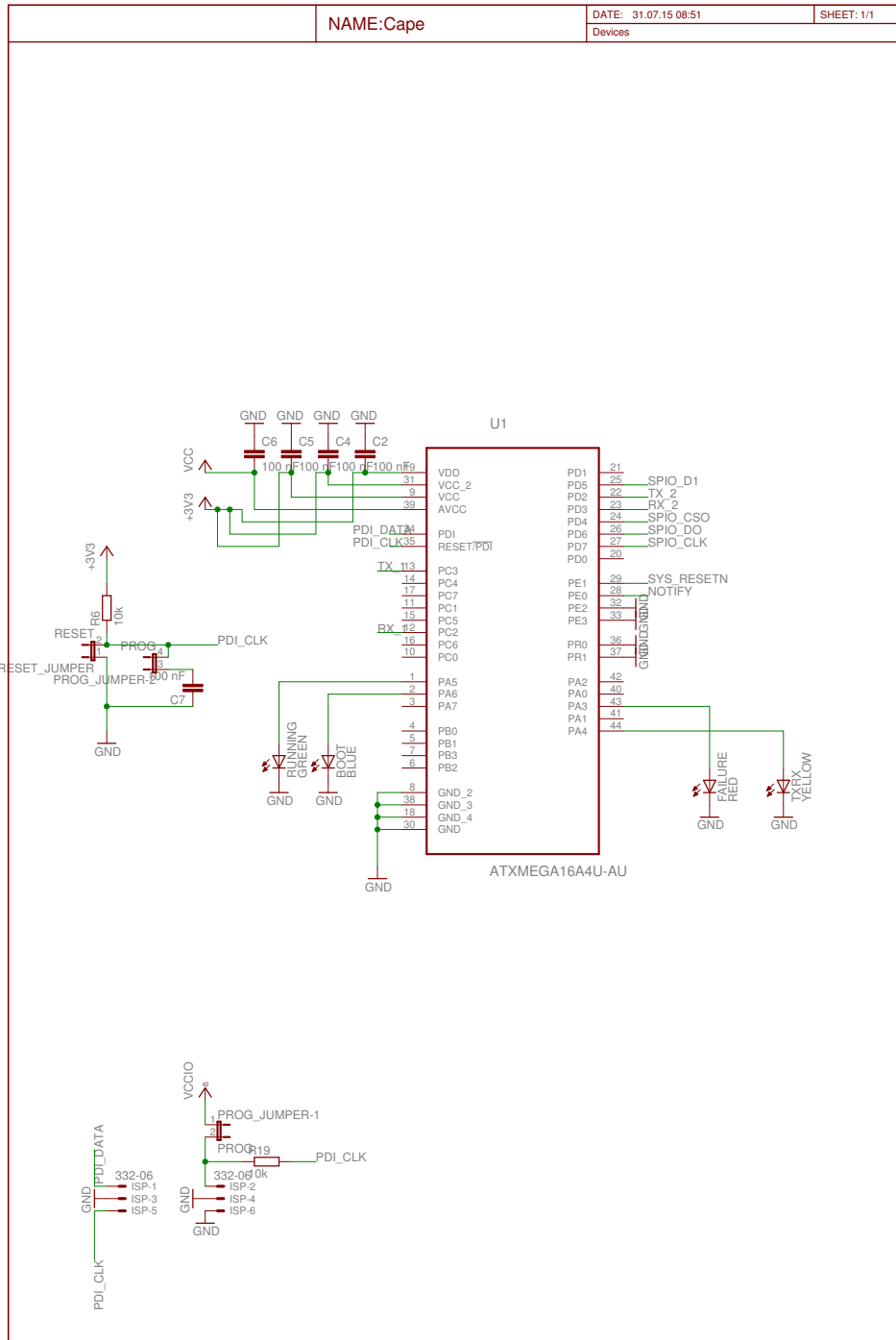
<https://github.com/anates/DispersionSetup>

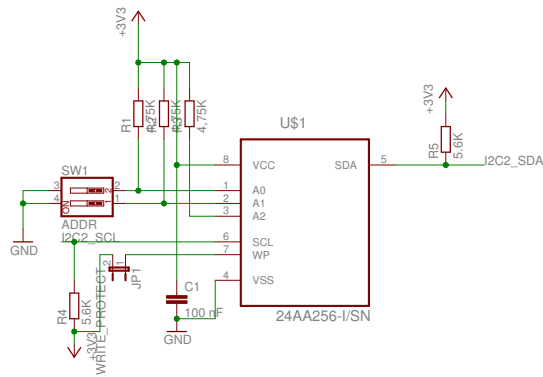
A.2 Circuits

A.2.1 Cape, Ver. I



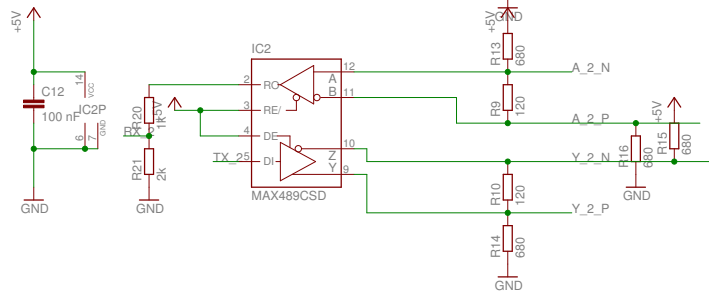
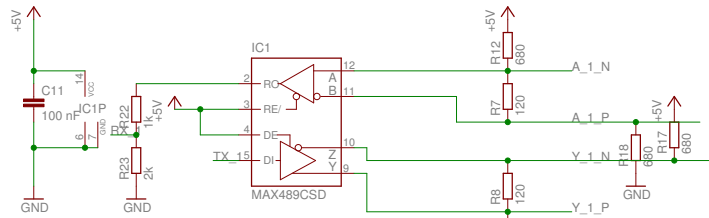
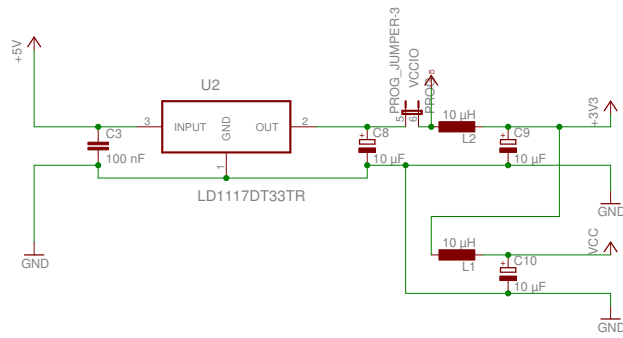
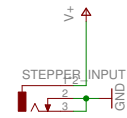
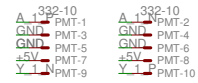
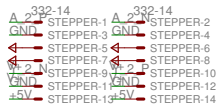
A.2.2 Cape, Ver. III



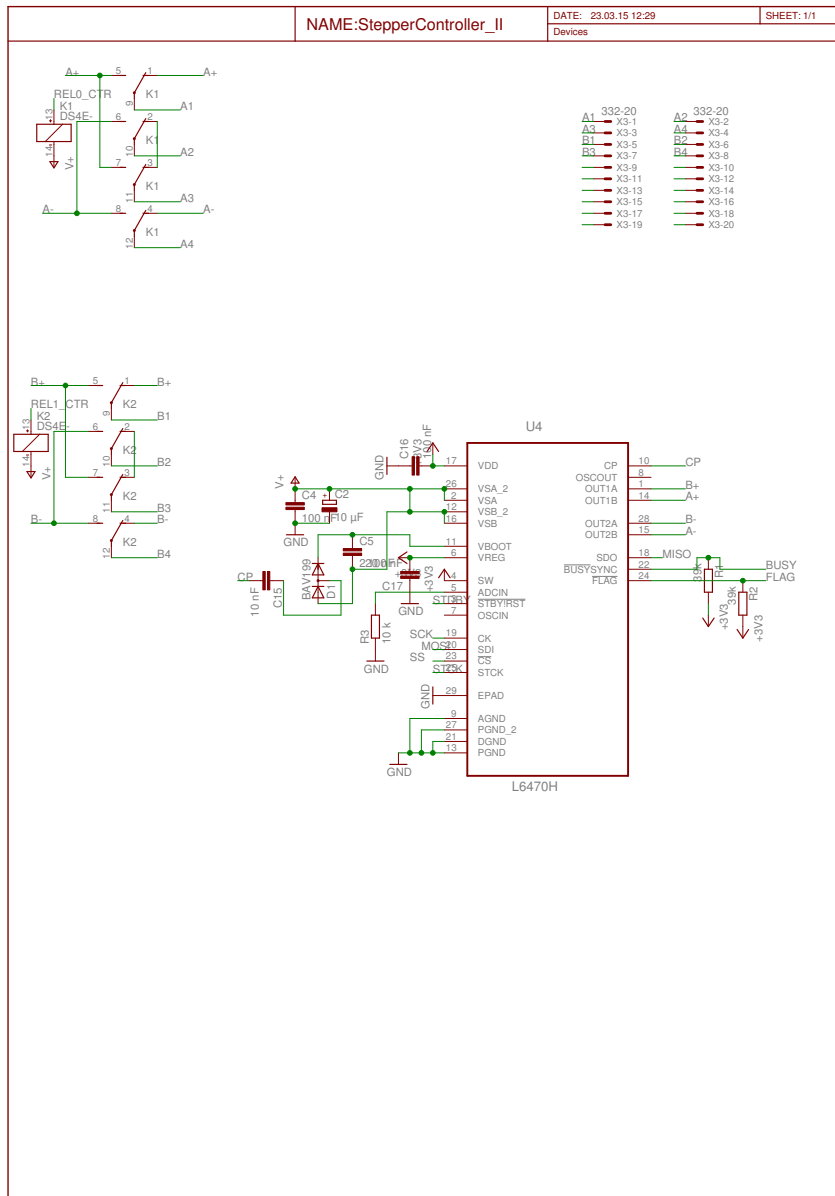


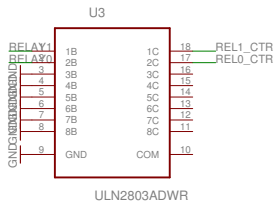
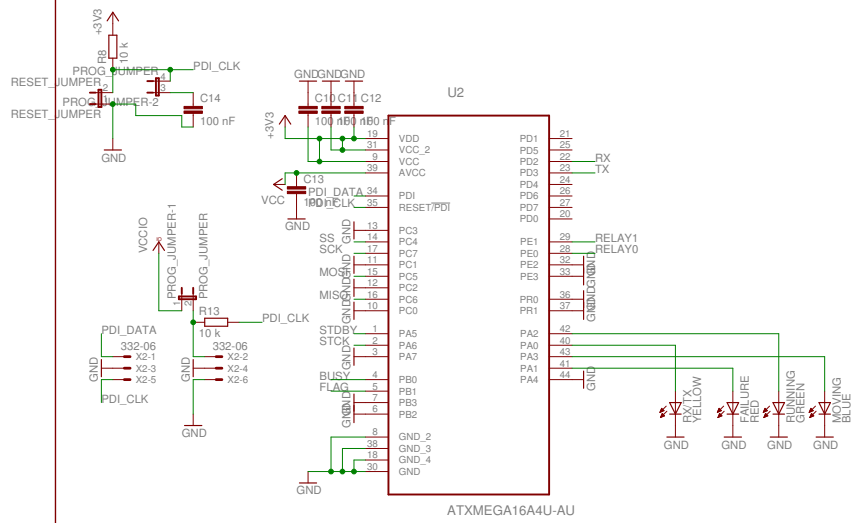
GND	P8-46	GND	P8-46
MCC1_DA16	P8-45	MCC1_DA16	P8-45
MCC1_DA17	P8-44	MCC1_DA17	P8-44
MCC1_DA18	P8-43	MCC1_DA18	P8-43
NS4	P8-7	NS22	P8-8
NS5	P8-9	NS23	P8-10
NS6	P8-11	NS24	P8-12
EHPWM	P8-13	NS25	P8-14
NOTIEV	P8-15	NS26	P8-16
NS9	P8-17	NS27	P8-18
EHPWM	P8-19	MMC1_DA20	P8-19
MMC1_DA21	P8-21	MMC1_DA21	P8-21
MMC1_DA22	P8-23	MMC1_DA22	P8-23
MMC1_DA23	P8-24	MMC1_DA23	P8-24
MMC1_DA24	P8-25	NS31	P8-28
LCD_VS	P8-27	LCD_PCLK	P8-28
LCD_HS	P8-29	LCD_A0	P8-29
LCD_DA1	P8-30	LCD_DA1	P8-30
LCD_DA2	P8-31	LCD_DA2	P8-31
LCD_DA3	P8-32	LCD_DA3	P8-32
LCD_DA4	P8-33	LCD_DA4	P8-33
LCD_DA5	P8-34	LCD_DA5	P8-34
LCD_DA6	P8-35	LCD_DA6	P8-35
LCD_DA7	P8-36	LCD_DA7	P8-36
LCD_DA8	P8-37	LCD_DA8	P8-37
LCD_DA9	P8-38	LCD_DA9	P8-38
LCD_DA10	P8-39	LCD_DA10	P8-39
LCD_DA11	P8-40	LCD_DA11	P8-40
LCD_DA12	P8-41	LCD_DA12	P8-41
LCD_DA13	P8-42	LCD_DA13	P8-42
LCD_DA14	P8-43	LCD_DA14	P8-43
LCD_DA15	P8-44	LCD_DA15	P8-44
LCD_DA16	P8-45	LCD_DA16	P8-45

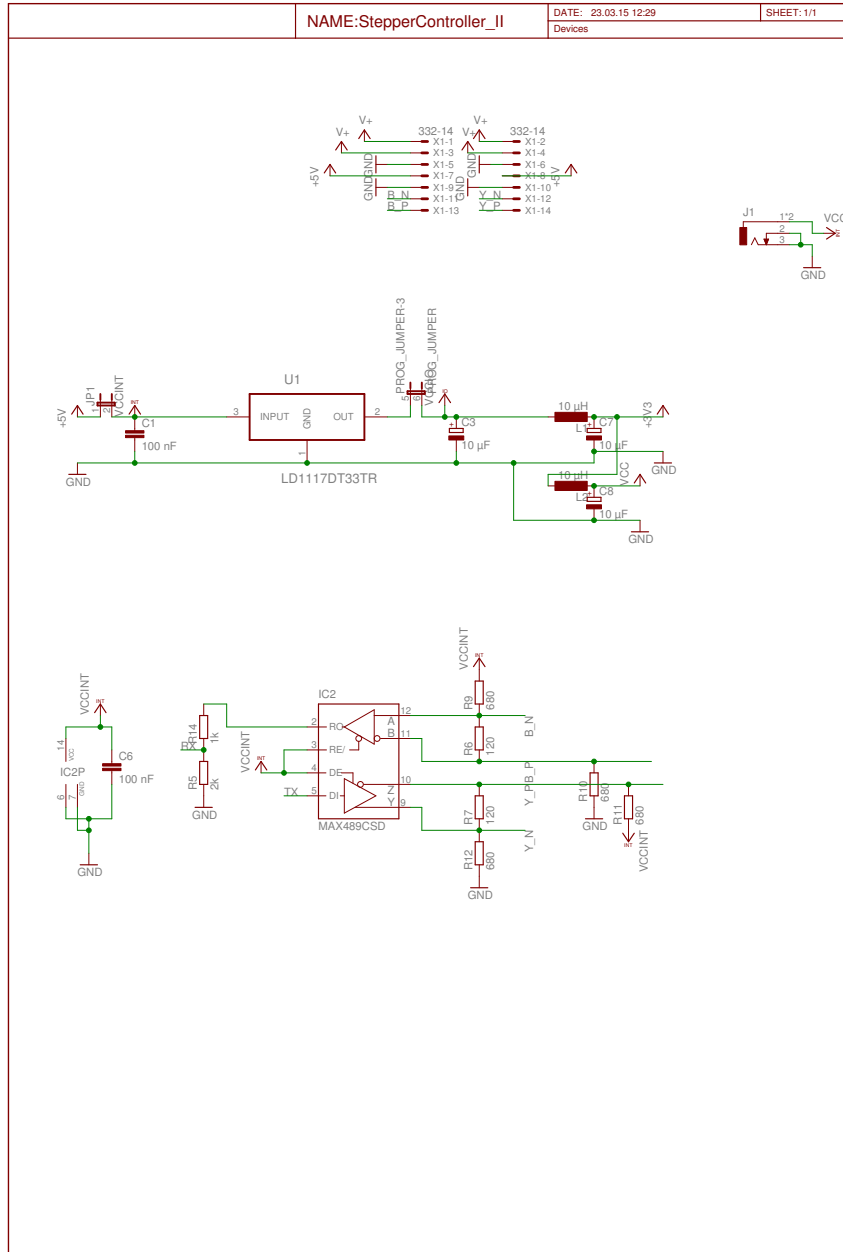
GND	P9-46	GND	P9-46
VDD_3V3	P9-2	VDD_3V3	P9-2
+5V	P9-3	+5V	P9-3
+5V	P9-6	+5V	P9-6
SYS_5V	P9-8	SYS_5V	P9-8
PWR_BTN	P9-9	SYS_FLT	P9-11
NS2	P9-12	NS75	P9-12
NS3	P9-13	EHPWM	P9-14
NS4	P9-15	EHPWM	P9-15
SPI0_CS0	P9-17	SPI0_CS0	P9-17
J2C2_SCL	P9-19	J2C2_SDA	P9-19
SPI0_DQ	P9-20	SPI0_DQ	P9-20
NS5	P9-21	NS81	P9-24
NS58	P9-23	NS82	P9-25
NS59	P9-25	NS83	P9-26
NS60	P9-27	SPI1_CS0	P9-28
SPI1_DQ	P9-29	NS84	P9-30
SPI1_SCL	P9-31	VDD_ADC	P9-32
AIN4	P9-33	GND_A	P9-34
AIN6	P9-35	AIN6	P9-36
AIN2	P9-37	AIN3	P9-38
AIN0	P9-39	AIN1	P9-40
NS67	P9-41	ECAP_PWM	P9-42
GND	P9-43	GND	P9-44
GND	P9-45	GND	P9-46



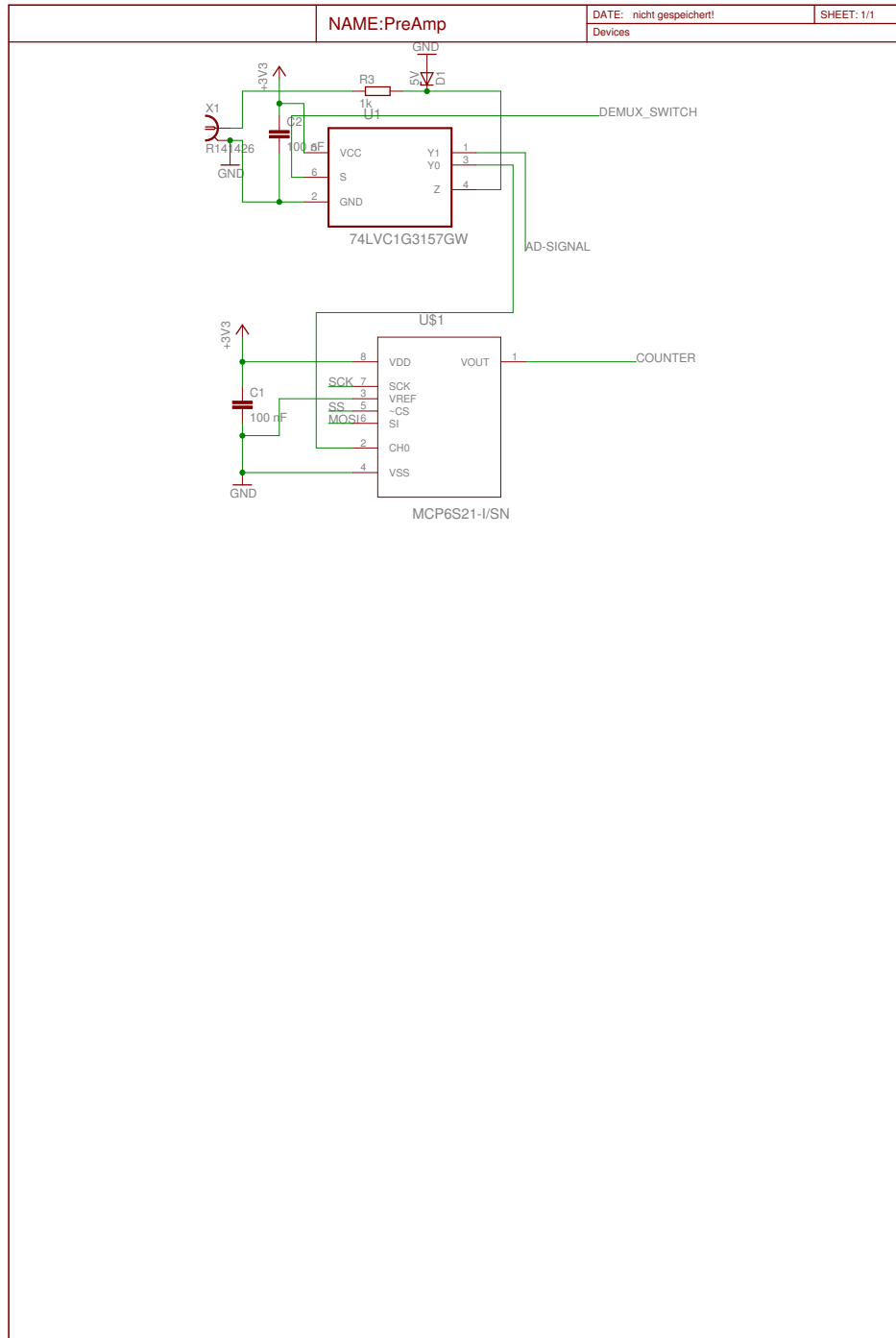
A.2.3 Stepper Controller, Ver. I

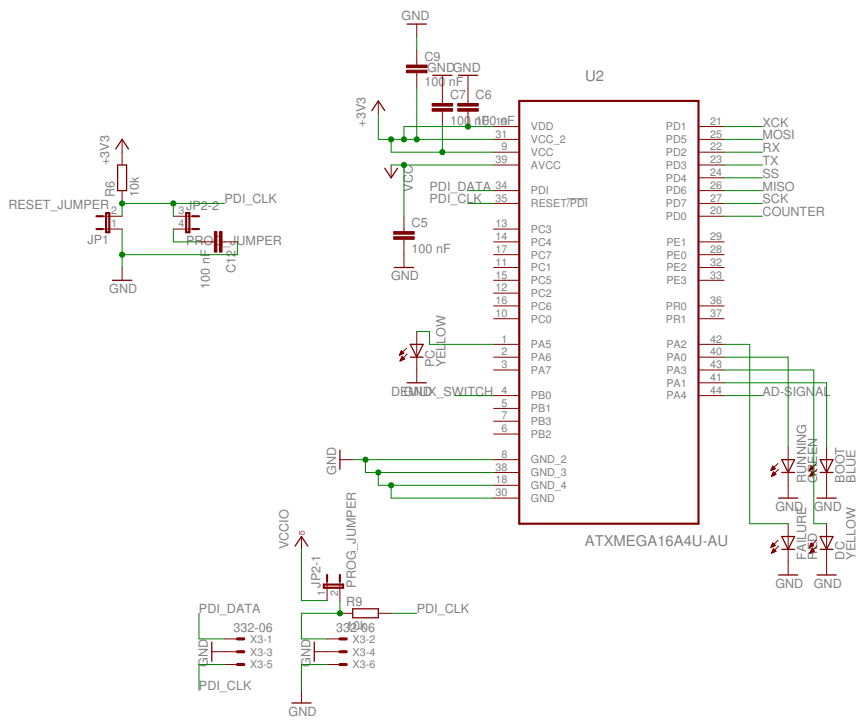


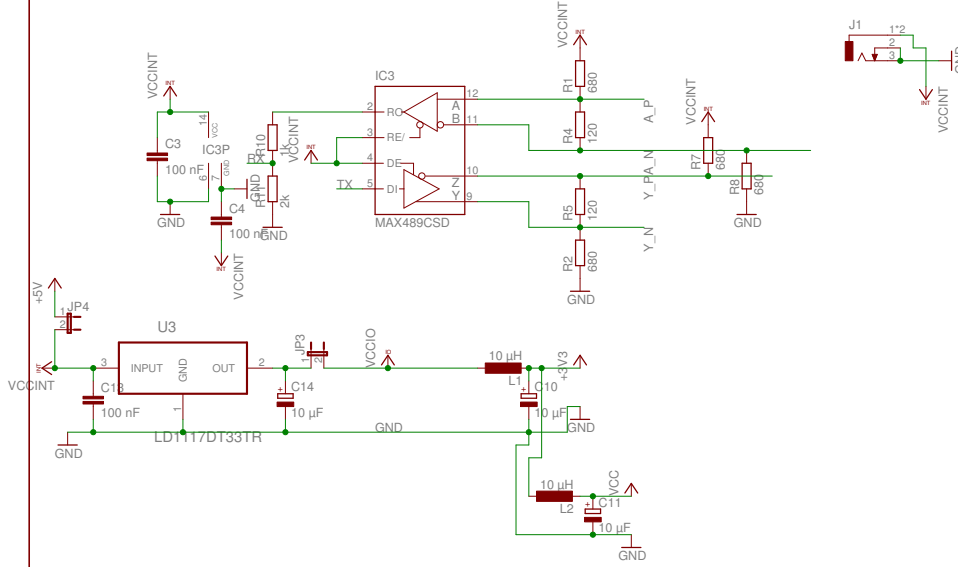




A.2.4 Amplifier, Ver. I







- | | | | | | |
|-----|---|------|-----|---|-------|
| A_P | → | X2-1 | A_N | → | X2-2 |
| GND | → | X2-3 | GND | → | X2-4 |
| +5V | → | X2-5 | +5V | → | X2-6 |
| Y_N | → | X2-7 | Y_P | → | X2-8 |
| | | X2-9 | | | X2-10 |

A.3 Case requirements

Requirement	value
Maximum Size	
Width	19"-rack
Height	3u or 4u
Maximum Depth	18"
Necessary power supplies	
Power supply for cooling fans	
Variable power supply	max. 12V/12A
Fixed power supply	15V/1A
Fixed power supply	5V/20A
Power to be cooled	
3-lasers	10W each
IPG-laser	120W
Fiber coupler	30W
Laser fiber	60W
Fiber requirements	See image 7.1
Front panel openings	
Power supply control for variable power control	
USB Port	
BNC Port	
Security key lock	
Emergency power off button	
Laser fiber output	
Cooling ports	
Back panel openings	
Main power supply input	
Secondary power supply input (for 1. generation)	
BNC input port	

Table A.1: Laser case requirements

A.4 Data sheets

A.4.1 Spectrometer 14018

SPEX

INDUSTRIES, INC. • 3880 PARK AVENUE • METUCHEN, N.J., 08840 • ☎ (201)-549-7144

Technical Note No. 40

Revised FEB. 1975

Subject: Low Frequency Raman Spectra with the Spex Double Monochromator and Triple Monochromator SystemSummary

Measurement of low frequency Raman spectra of many substances is easily accomplished with the Spex double monochromator, provided:

- 1) 1800g/mm holographic gratings are used instead of ruled gratings, as in our 14018.
- 2) Aperture of the monochromator is reduced, and
- 3) Image of hot spot of laser beam on sample is imaged to the side of the entrance slit.

There are still certain types of sample which require a triple spectrometer system (Spex 14018 and TTM). Good examples are MoS₂ powder, PbS powder, Mg metal, all opaque.

Until recently, it was thought that the Raman lines of l-cystine at 9.6 and 15 cm⁻¹ could be detected only with a triple monochromator or, in the Spex version, a double monochromator plus the add-on Third Monochromator. We have now found that they can be detected equally well with the Spex 14018. Apart from switching to finer holographic gratings, the advantages of which are pointed out in Technical Note No. 39, the trivial modifications required are applicable to many materials.

Until the advent of holographic gratings, optical aberrations could not normally be detected in a Spex monochromator. They were masked by the scattered light, ghosts and satellites characteristic of all ruled gratings, even those interferometrically ruled. On the other hand, with the newly introduced holographic gratings, which have no measurable ghost or satellite structure and a scattered light 1 to 2 decades below that of ruled gratings, residual spherical aberration in the Czerny-Turner mount becomes apparent. Its only effect, as far as we can presently determine, is on the optical transfer function: to reduce the contrast between a weak line and a neighboring strong line. Lines close to the Rayleigh line provide the most significant challenges.

Since spherical aberration is inversely proportional to the square of the aperture, the collimating mirror of the first half of a Spex 14018 Double Monochromator in a Ramalog 5 was masked to 1/2 aperture in Figure 1B. Note that there is a distinct improvement in the near scatter. Fig. 2A and B compared to Fig. 1 show the effect of the removal of the hot spot from the entrance slit of the spectrometer. The hot spot is composed of Rayleigh, Tyndall and Raman scatter. It is obvious from the results that the Raman-to-Tyndall ratio is higher in the outer sections of the image than in the central section. The last spectrum is fully equivalent to the best we have seen with any competitive double or triple monochromator or, for that matter, with our TTM.

Even more dramatic, however, is the spectrum shown in Fig. 3. A paraffin with the formula C₃₆H₇₄ scanned from -40 to +40 cm⁻¹ clearly shows structure at 6 cm⁻¹ from the exciting line. Until now, even with single-mode, high-power lasers and an iodine filter, this structure has never been seen.

The new J&Y double monochromator has also been shown to produce close-in spectra equivalent to those heretofore thought possible only with a triple monochromator. Essentially, this instrument incorporates two features: an optical mount that is free of spherical aberration and a fourth slit apparently designed as a spatial filter to cut down on Rayleigh scatter. Having already demonstrated that spherical aberration is indeed an important consideration, we investigated the performance of a fourth slit.

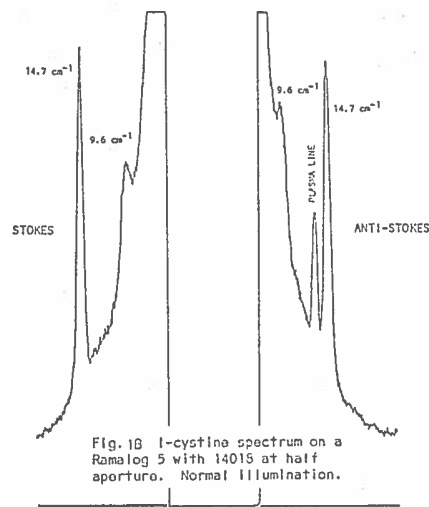
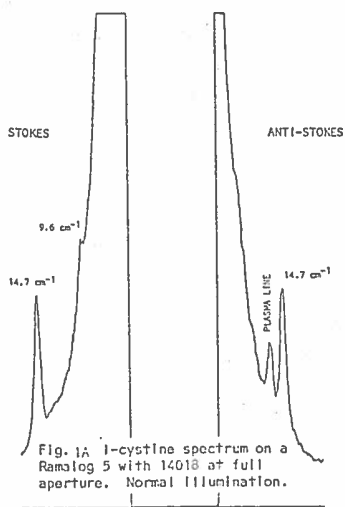
* TTM = The Third Monochromator

A fourth slit was quite easy to attach to a Spex double for an experiment as shown in Fig. 4. Note that only one additional reflecting surface was required over that in our normal instrument.

No improvement was achieved through a fourth slit. Compare Fig. 5 to the spectrum in Fig. 2B. From this and other experiments done, we conclude that a fourth slit has no effect on near stray light.

The last parameter investigated was polarization. In practice this is not expected to be too important. From highly scattering surfaces--those that a competent Raman technologist would avoid or simply polish--Tyndall scattering and reflections can be highly polarized while close-in Raman scattering is depolarized. An analyzer in the scattering beam helps for those unusual samples. The easiest way to check this is to examine the image at the slit with and without a polarization analyzer.

As stated before, certain types of samples require a triple monochromator system for recording the low frequency Raman region. These samples are metals that are highly reflecting at the laser wavelength, and solid samples that are opaque to the illumination. Such samples do not permit the internal scattering and diffusion of the laser light that enhances the Raman to Tyndall scatterer ratio, giving the improvements described before. Figures 6A and 6B compare the spectrum of Mg metal with a double and triple spectrometer system. Figures 7A and 7B give the same for MoS_2 .



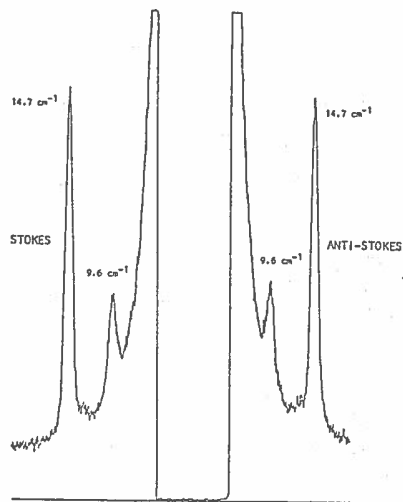


Fig. 2A l-cystine spectrum on a Ramalog 5 with 14018 at full aperture and hot-spot off-axis.

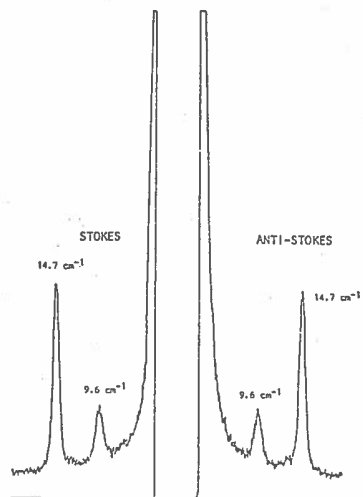


Fig. 2B l-cystine spectrum on a Ramalog 5 with 14018 at half aperture and hot-spot off-axis.

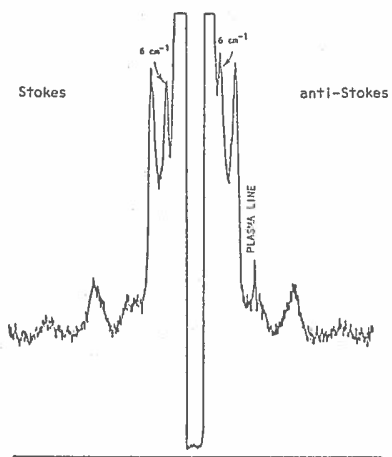


Fig. 3 Spectrum of a paraffin, with formula $C_{26}H_{54}$, clearly showing structure at 6 cm^{-1} never before reported even with single moded laser and iodine filter.

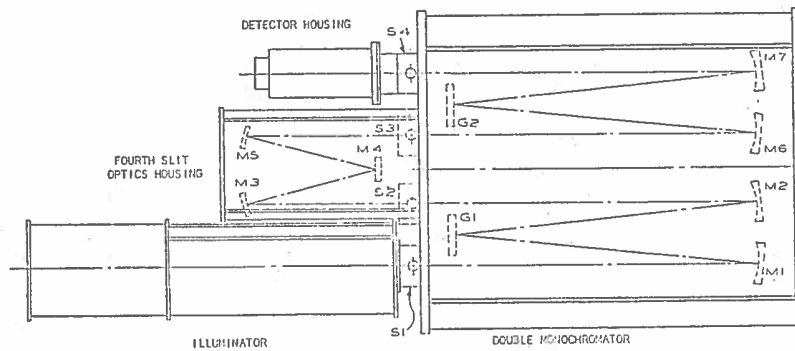


Fig. 4 Experimental 14018 with two central slits, instead of the usual one, and all reflecting optics in place.

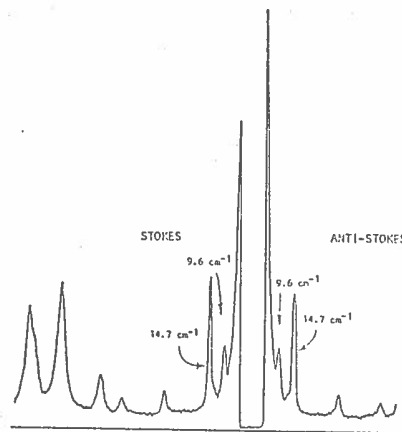
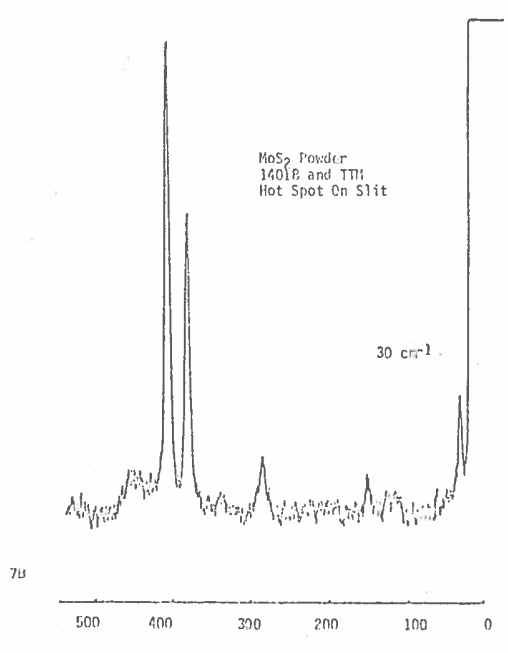
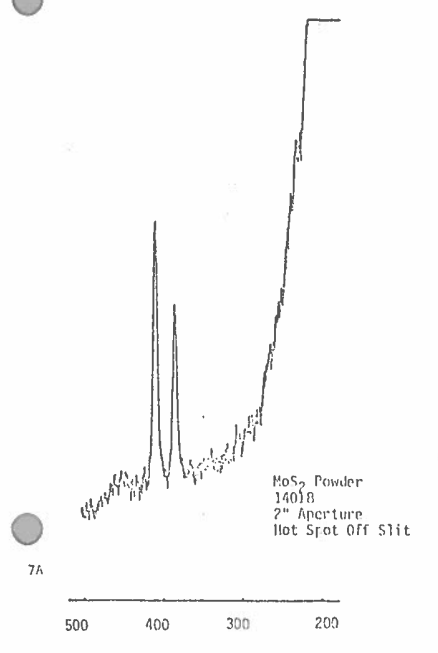
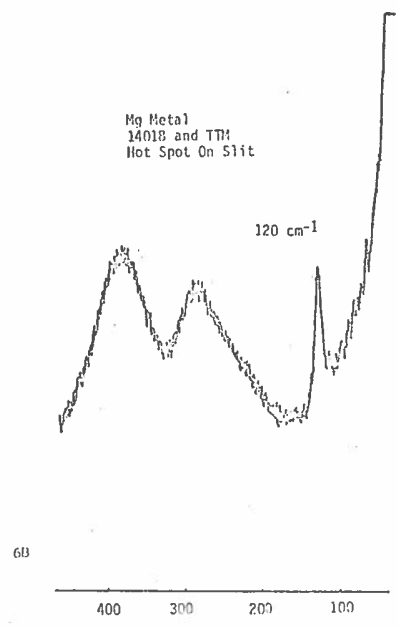
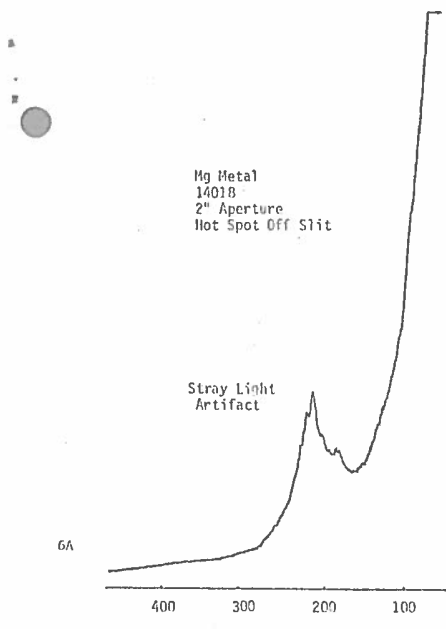


Fig. 5 l-cystine spectrum on a Ramalog 5 with 14018 and 4th slit accessory in place. Hot-spot off-axis.



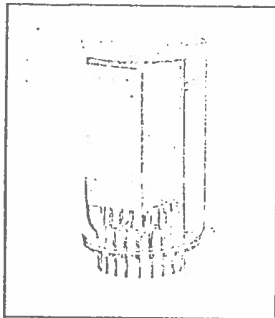
A.4.2 Photo multiplier C31034

RCA
Electronic
Components

SPER LEISTUNG GERM
7 000 Stuttgart - 40
Waikersheimer Straße 15
Telefon (07 11) 87 12 40
W e s t G e r m a n y

Photodetector
Developmental Type

C31034



Photomultiplier

2"-Diameter, 11-Stage, QUANTACON Type Having a Gallium-Arsenide Photocathode

- Broad Spectral Response --
200 to 930 nanometers
- Restricted Photocathode Area --
4 mm x 10 mm minimum
- Typical Quantum Efficiency --
14% at 550 nm
12% at 694.3 nm
9% at 860 nm
- Low Dark Noise --
Dark Pulse Summation
16 pe
 $\sum_{1/8 \text{ pe}} = 10,000 \text{ cps at } 20^\circ \text{ C}$
16 pe
 $\sum_{1/8 \text{ pe}} = 12 \text{ cps at } -20^\circ \text{ C}$

RCA Developmental Type C31034 is a 2"-diameter, head-on, 11-stage QUANTACON photomultiplier having a gallium-arsenide photocathode, an ultraviolet-transmitting glass window, and high-stability copper-beryllium dynodes. The photocathode surface of this tube has a minimum sensitive area of 4 mm x 10 mm.

The C31034 has high sensitivity throughout its entire spectral range, extremely low dark noise, and fast time response characteristics. These characteristics make this tube highly useful in such applications as photon counting and laser detection systems.

General Data

Spectral Response	See Figure 1
Wavelength of Maximum Response	830 ± 50 nm
Cathode, Opaque	Gallium-Arsenide
Minimum projected area	4 mm x 10 mm
Window	Ultraviolet-Transmitting Glass, Corning [®] No. 9741, or equivalent
Index of refraction at 656 nm	1.466
Dynodes:	
Substrate	Copper-Beryllium
Secondary-emitting surface	Beryllium-Oxide
Structure	In-Line Electrostatic-Focus Type
Socket	RCA Part Nos. AJ2144, AJ2145, or AJ2180 ^b
Magnetic Shield	See footnote c

Maximum Ratings, Absolute-Maximum Values

DC Supply Voltage:

Between anode and cathode	2000 max. V
Between anode and dynode No.11	250 max. V
Between adjacent dynodes	250 max. V
Between dynode No.1 and cathode	200 max. V

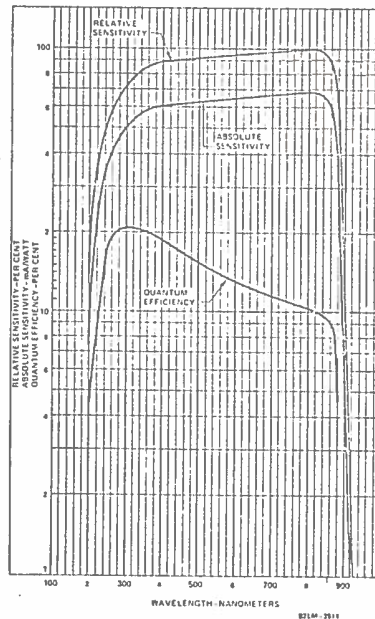


Figure 1 — Typical Photocathode Spectral Response Characteristics

For further information or application assistance on this device, contact your RCA Sales Representative or write Phototube Marketing, RCA, Lancaster, PA 17604.

Developmental type devices or materials are intended for engineering evaluation. The type designation and data are subject to change, unless otherwise arranged. No obligations are assumed for notice of change or future manufacture of these devices or materials.

Information furnished by RCA is believed to be accurate and reliable. However, no responsibility is assumed by RCA for its use, nor for any infringements of patents or other rights of third parties which may result from its use. No license is granted by implication or otherwise under any patent or patent rights of RCA.

Printed in U.S.A. /571
C31034

Maximum Values (cont'd)

Average Anode Current ^d	0.1 max.	mA
Average DC Cathode Current	10 max.	nA
Ambient Temperature	55 max.	°C

Characteristics Range Values for Equipment Design

Under conditions with DC supply voltage (E) across a voltage-divider providing electrode voltages as shown in Table I, and at an ambient temperature of 22° C, unless otherwise indicated.

With E = 1500 volts (except as noted)

	Min.	Typ.	Max.	
Anode Sensitivity:				
Radiant, at 830 nm	—	4.1x10 ⁴	—	A/W
Luminous ^e	100	300	2000	A/lm
Cathode Sensitivity:				
Radiant:				
At 830 nm	—	68	—	mA/W
At 860 nm ^f	25	60	—	mA/W
Luminous ^g	300	500	—	μA/lm
Quantum efficiency:				
At 550 nm	—	14	—	%
At 694.3 nm	—	12	—	%
At 860 nm	—	9	—	%
Current Amplification (Gain)	—	6x10 ⁵	—	
Anode Dark Current at 100 A/lm ^h	—	3x10 ⁻⁹	1x10 ⁻⁸	A
Equivalent Anode Dark Current Input, at 100 A/lm ^h	—	3x10 ⁻¹¹	1x10 ⁻¹⁰	lm
Dark Pulse Summation:ⁱ				
1/8 to 16 photoelectrons:				
At +20° C	—	10,000	—	cps
At -20° C	—	12	—	cps

Table I

Voltage to be Provided by Divider	
Between	8.06% of Supply Voltage (E) multiplied by:
Cathode and Dynode No.1	1.0
Dynode No.1 and Dynode No.2	1.4
Dynode No.2 and Dynode No.3	1.0
Dynode No.3 and Dynode No.4	1.0
Dynode No.4 and Dynode No.5	1.0
Dynode No.5 and Dynode No.6	1.0
Dynode No.6 and Dynode No.7	1.0
Dynode No.7 and Dynode No.8	1.0
Dynode No.8 and Dynode No.9	1.0
Dynode No.9 and Dynode No.10	1.0
Dynode No.10 and Dynode No.11	1.0
Dynode No.11 and Anode	1.0
Anode and Cathode	12.4

^a Made by Corning Glass Works, Corning, N.Y. 14930.

^b The AJ2145 is designed specifically for chassis mounting. The AJ2180 is similar to the AJ2145 but is light-tight. The AJ2144 is designed for use in any desired mounting arrangement. It is supplied with an unattached clamp ring which fits to either the top or bottom of its socket body to permit chassis mounting. The ring is not normally required for other mounting arrangements and can be discarded to make such arrangements more compact.

The C31034 is supplied without a socket. The AJ2144, AJ2145, or the AJ2180 may be ordered from your nearest RCA Field Sales Office.

^c Magnetic shielding material in the form of foil or tape as available from the Magnetic Shield Division, Perfection Mica Company, 1322 N. Elston Avenue, Chicago, IL 60622, or equivalent.

^d Averaged over any interval of 30 seconds maximum.

^e Under the following conditions: The light source is a tungsten-filament lamp having a lime-glass envelope. It is operated at a color temperature of 2870° K. The value of light flux is 1 x 10⁻⁸ lumen.

^f Measured using a calibrated narrow bandpass filter having a peak wavelength of 860 nanometers and a bandpass of approximately 10 nanometers blocked from infrared to X-ray wavelength. The light source is a tungsten-filament lamp having a lime glass envelope. The value of light flux incident on the filter is 1 x 10⁻⁴ lumen and 200 volts are applied between cathode and all other electrodes connected as anode.

^g Under the following conditions: The light source is a tungsten-filament lamp having a lime-glass envelope. It is operated at a color temperature of 2870° K. The value of light flux is 1 x 10⁻⁴ lumen and 200 volts are applied between cathode and all other electrodes connected as anode.

^h With supply voltage adjusted to give a luminous sensitivity of 100 amperes per lumen. Dark current caused by thermionic emission may be reduced by use of a refrigerant.

ⁱ Measured with the tube in complete darkness. The pulse height for the single photoelectron equivalent is determined by using a light source operated at a low color temperature to assure the high probability of single photoelectron emission from the photocathode of the tube. The intensity of the light source is adjusted for approximately 10⁴ photons per second. This light is removed before the dark pulse summation is measured. The supply voltage is adjusted so that the peak of the single electron distribution lies in channel No.8. This corresponds to a tube gain of approximately 10⁶.

Operating Considerations

Ambient Atmosphere

Operation or storage of this tube in environments where helium is present should be avoided. Helium may permeate the tube envelope and may lead to eventual tube destruction.

Anode-Dark Current

The tube is intended for use in systems requiring low dark current. Accordingly, the base of the tube and its socket should never be allowed to become contaminated by handling. Such contamination produces leakage and dark current. It is recommended that if the tube base or its socket is handled that it be washed with a solution of alkaline soap cleaner such as Alconox[®], or equivalent, and de-ionized or

distilled water having a temperature not exceeding 60° C. The base or socket should then be rinsed in de-ionized or distilled water (60°) for several minutes and then air-blown dry.

*Distributed by Arthur H. Thomas Company, Vine Street and 3rd, Philadelphia, PA 19105.

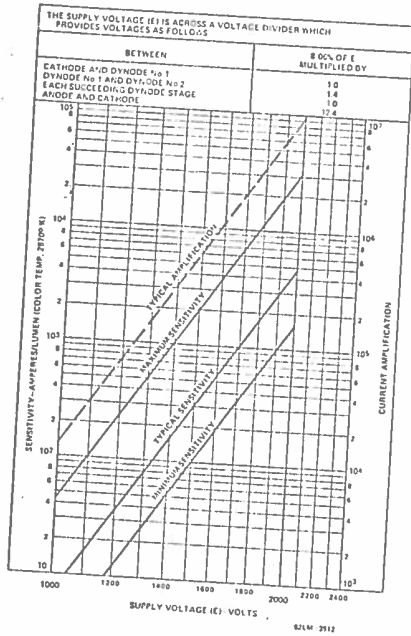


Figure 2 — Sensitivity and Current Amplification Characteristics

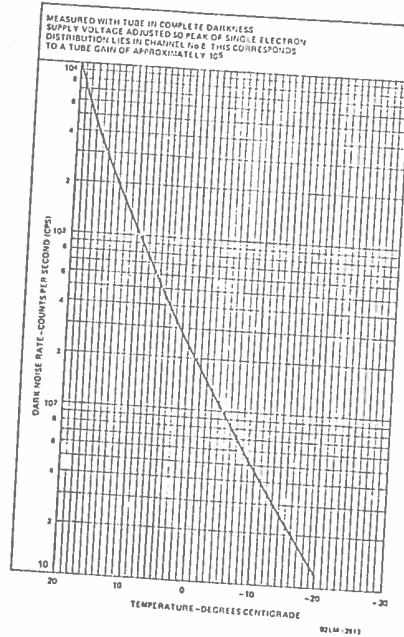
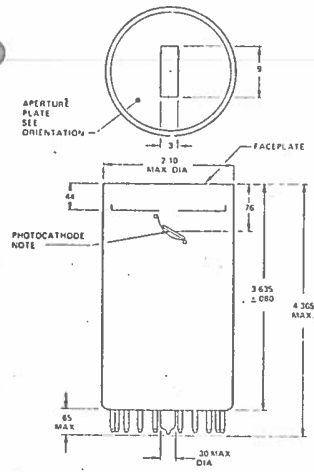


Figure 3 — Typical Dark Noise Rate as a Function of Temperature

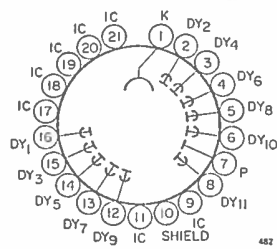


Dimensions in Inches

92LS 3472A1

Note - Collection angle is approximately f/1.8.

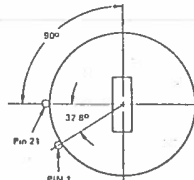
Figure 4 - Dimensional Outline



- | | |
|---|---|
| Pin 1: Photocathode | Pin 12: Dynode No.9 |
| Pin 2: Dynode No.2 | Pin 13: Dynode No.7 |
| Pin 3: Dynode No.4 | Pin 14: Dynode No.5 |
| Pin 4: Dynode No.6 | Pin 15: Dynode No.3 |
| Pin 5: Dynode No.8 | Pin 16: Dynode No.1 |
| Pin 6: Dynode No.10 | Pin 17: Aperture plate (See Note) |
| Pin 7: Anode | Pin 18: Internal Connection, Do not use |
| Pin 8: Dynode No.11 | Pin 19: Internal Connection, Do not use |
| Pin 9: Internal Connection, Do not use | Pin 20: Internal Connection, Do not use |
| Pin 10: Electron Multiplier Shield (Connect to Dynode No.4 potential) | Pin 21: Internal Connection, Do not use |
| Pin 11: Internal Connection, Do Not use | |

Note: Connect Aperture plate (pin 17) to photocathode (pin 1).

Figure 7 - Basing Diagram (Bottom View)



92LS 3514

Figure 5 - Orientation of Aperture Plate with Respect to Base Pin 21. (Top View)

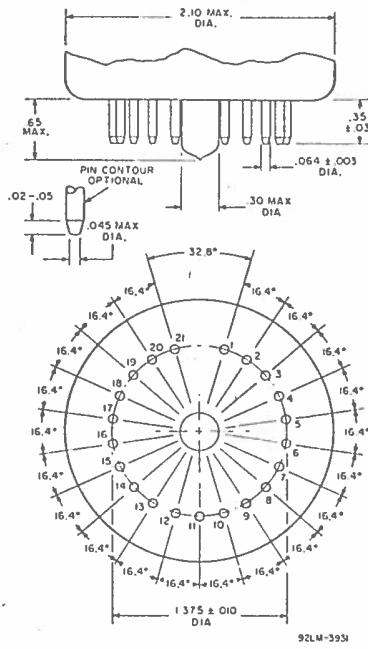


Figure 6 - Detail of Base Arrangement

A.5 Design of the case for the laser described in chapter 7

A.5.1 Requirements for the case

The first task before designing was to determine the target requirements. Those are displayed in table A.1. Furthermore the laser which had to be placed inside is shown in image 7.1.

To make the design itself and the possibility of repairment easier the case was separated into modules. That means that both the optical and the electrical part were separated, and only via wire trees connected. If one of those parts breaks the module can easily removed and replaced without having to unscrew too much.

A.5.2 General module description

A.5.2.1 Laser module

As already stated in the requirements (table A.1), the laser consists out of three „small“ laser diodes, one „big“ laser, some optical combiners and isolators and some fibers. Those elements had to be fixed relatively to each other such that fast movements could not disturb the operation of the laser. Furthermore the fiber mount itself has to maintain a certain minimal radius for keeping the fiber from breaking or losing too much energy due to light exiting the fiber.

Each of the components dissipate heat (which is listed in table A.1) which also has to be removed while keeping an eye on the target temperature range.

A.5.2.2 Electrical module

The electrical module consists both of the power supply and the controlling circuits. The power supply is responsible for converting the supply voltage into one or more target voltages, while the controlling circuits monitor the temperatures of the lasers, provide external access and external control of the laser.

A.5.3 First design

The first design of the laser packaging was mainly aimed towards meeting at least most of the requirements of the packaging while keeping it still simple and easy to calculate. All parts of this design can be found in the folder „drafts“ delivered together with this thesis. The parts for the first design are located in „First design“.

A.5.3.1 Laser module

In order to both cool the fiber and to provide enough stability, we decided to wind the fibers up onto an aluminium cylinder. The first stage of the laser does not

need cooling, while the second stage of the laser nevertheless emits up to 60W of thermic power, and therefore has to be cooled. The heat dissipation was calculated by assuming that all laser power which is emitted from the pump laser is damped in the fiber itself, and none is emitted at the end. This method of calculation should keep a safety margin big enough for sudden power peaks. To cool the whole fiber, and to stabilize it it was mounted onto an aluminium cylinder, and attached to it with heat paste to improve the thermal flow. This coil is attached to an aluminium radiator to increase the area exposed to the air flow and to increase stability. Furthermore the three smaller lasers are also attached to this radiator. Each of those lasers generate up to 10W of thermic power (table A.1), which also has to be cooled. The whole arrangement was designed to be air-cooled. To be sure that it stays within the temperature borders the whole module was calculated afterwards, which can be seen in appendix A.6.1 of this thesis. A second thing to be cooled was the fiber coupler which combined the fibers from the first stage of the laser and the pumping laser to the second stage. This connector was also supposed to emit between 10W and 30W of thermal energy, but for safety margin a theoretical output power of 30W was applied. An additional requirement for the connector was that it should be as near as possible towards the copper coil to reduce the amount of free-floating fiber. Therefore it needed its own holder. This holder was built out of aluminium, and mounted onto the main radiator. To increase the possibility of heat transfer between the main radiator and the holder itself the ground plane was increased. One idea to increase the cooling was to add either a radiator or directly some fins onto the holder. This idea was calculated in A.7.5, with the result that it is possible to decrease the temperature difference, but not at the correct point. The pumping laser itself could generate up to 120W of thermal energy, which was again calculated by taking the maximum input of electrical energy and assuming that the whole energy is dissipated as heat. To keep the pumping laser within the temperature borders it was attached to two peltier elements via several heat pipes. Those two elements are cooled by two aluminium coolers with 120mm-fans attached. According to the data sheet each of those elements can cool up to 56W of thermal energy without increasing the temperature of the cold site of the peltier element. The incoming air flow is afterwards redirected onto the fins of the big aluminium cooler to provide the necessary air flow. To allow air cooling of the copper coil and the free fibers an additional inlet was created in the backside such that both the power supply and the fibers are getting enough air. This flow is pictured in figure A.2. To reduce the amount of free wires hanging around, and to control the air flow, a wire channel was designed. It should guide the wires from the fans and the IPG-laser on the heat pipes below the radiator to the electronic module. Additionally its form guides the incoming air from the back fans into the ribs of the radiator, which can be seen in figure A.2.

A.5.3.2 Electronic module

In the first design of the packaging we decided to use a commercial PC power supply for the fixed voltages and a separate input for the variable 12V/12A power supply. Nevertheless we left enough space for an additional power supply in the next design step. To be able to remove the whole electronic part at once (to make repairment and maintenance easier) all electronic components are fixed in a cage made out of aluminium u-shaped rails with a width of 10mm, a height of 8mm and a material thickness of 1.5mm. The control panels for the lasers are mounted on the front, while the power supply and the necessary air support channel is mounted in the back. The laser controllers each consist out of a display, the controller PCB itself and five control buttons.

A.6 Assembled model

Both modules are put together in the rack after final assembly, separated by a wall in between. This wall should both increase stability and prevent damage in case of intruding water. The whole model can be seen in figure A.1.

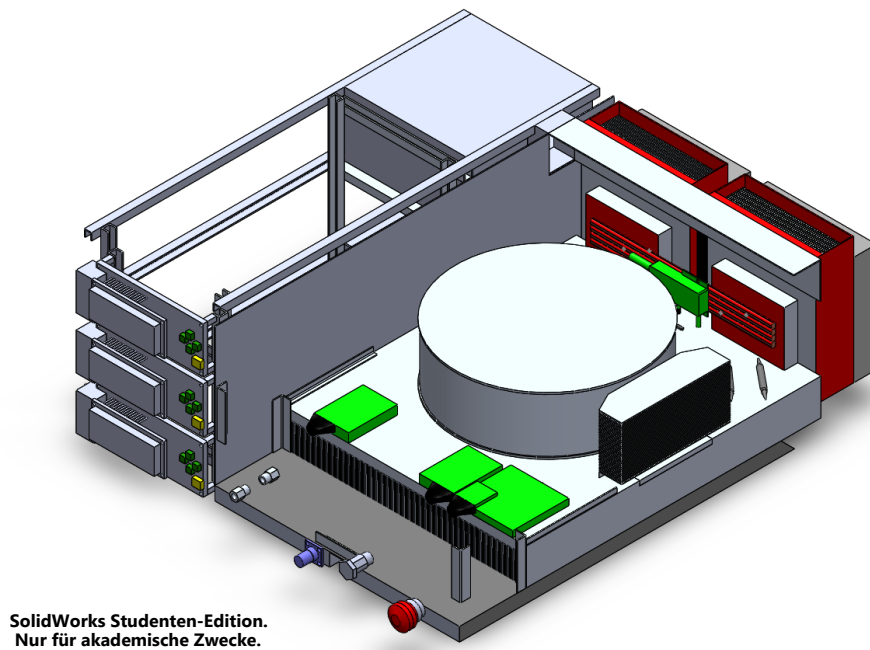


Figure A.1: 3D-model of the designed laser case, I. generation, without cover

In this model the covering case has been removed, in order to make the parts better visible. Nevertheless the input- and output ports can be seen on the front- and backpanel, as well as the two modules.

A.6.1 Heat- and airflow calculation

To decrease the possibility of hotspots the case was designed with a higher airflow out of the case than into the case. This was achieved by putting three 80mm-fans into the front of the case, each of them with a higher air flow rate than both the 120mm-fans according to their data sheet. The air flow through the 120mm-fans on the backside is used to cool the main radiator, while the air flow provided by the channel in the electronics compartment is used for providing extra air cooling in the fiber area (as already stated in A.5.3.1). The planned air flow is displayed in figure A.2.

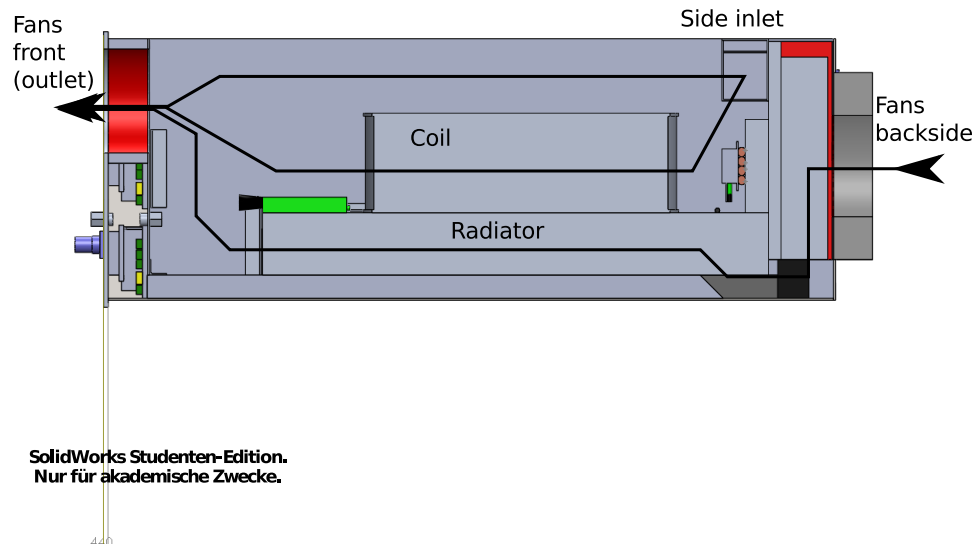


Figure A.2: Air flow in the laser case for the first generation

The maximum temperature of the radiator, of the lasers and of the coils should not exceed a maximum temperature of 75°C . Furthermore the fans at the backside should be designed to create a lower air flow intake than the fans at the front side are able to push out. This secures a lower pressure in the inside compared to the outside. For the beginning every material connection should be considered as ideal in terms of heat flow.

A.6.1.1 Calculation of heatflow for the first packaging design

To calculate the heat flow, [63] was used as a first reference point for calculating the heat flow without supporting air flow. For lowering the calculation difficulty the laser model was distributed into several parts: The fiber itself was distributed into two parts, the core and the cladding. After the fiber the heat is distributed into the single aluminium coil where the fiber is mounted onto. The aluminium coil is then forwarding the heat to the main radiator which also houses three small lasers and the fiber connector of the laser. First all applied heat powers had to be set. This leads to table A.2

Element	Heat applying elements	Total applied heat power in [W]
Aluminium coil	Amplifier stage	60
Aluminium radiator	Three lasers and fiber coupler	60

Table A.2: Heat distribution in the laser model

With those values we can calculate the temperature difference between fiber and radiator. But first the temperature of the incoming air has to be calculated, after that air is already used for cooling the peltier elements. Thus we have to use the formula (by using the energy conservation law) A.1.

$$P_{el} + \dot{Q}_L = \dot{V}_L \varrho_L \cdot c_L (T_{L_{in}} - T_u) \quad (\text{A.1})$$

with the used symbols explained in table A.3.

$P_{el} = 130$	electric power of the peltier elements and the fans ([W])
$\dot{Q}_L = 120$	heat power from the IPG laser diode ([W])
$\dot{V}_L = 0.05$	air flow current from the fans ($[\frac{\text{m}^3}{\text{s}}]$)
$\varrho_L = 1.2$	air density ($[\frac{\text{kg}}{\text{m}^3}]$)
$c_L = 1000$	air heat capacity ($[\frac{\text{J}}{\text{kg}\cdot\text{K}}]$)
$T_u = 293$	surrounding temperature ([K])

Table A.3: Symbols used in equation A.1

Thus we receive as result equation

$$T_{Lin} = \frac{P_{el} + \dot{Q}_L}{\dot{V}_L \cdot \rho_L \cdot c_L} + T_U \quad (\text{A.2})$$

$$= \frac{250}{0.05 \cdot 1.2 \cdot 1000} \text{ }^\circ\text{K} + 293 \text{ }^\circ\text{K} \quad (\text{A.3})$$

$$= 297.17 \text{ }^\circ\text{K} \quad (\text{A.4})$$

With this we see that the incoming air is already heated up with approximately 4°K before entering the main cooling system. This is regardless of the incoming air temperature, but after we do not have the data sheet of the used peltier element, we will always assume that the incoming temperature has 293°K.

To make the calculations easier and for simplifications we create an electric (thermal) network before starting the calculations:

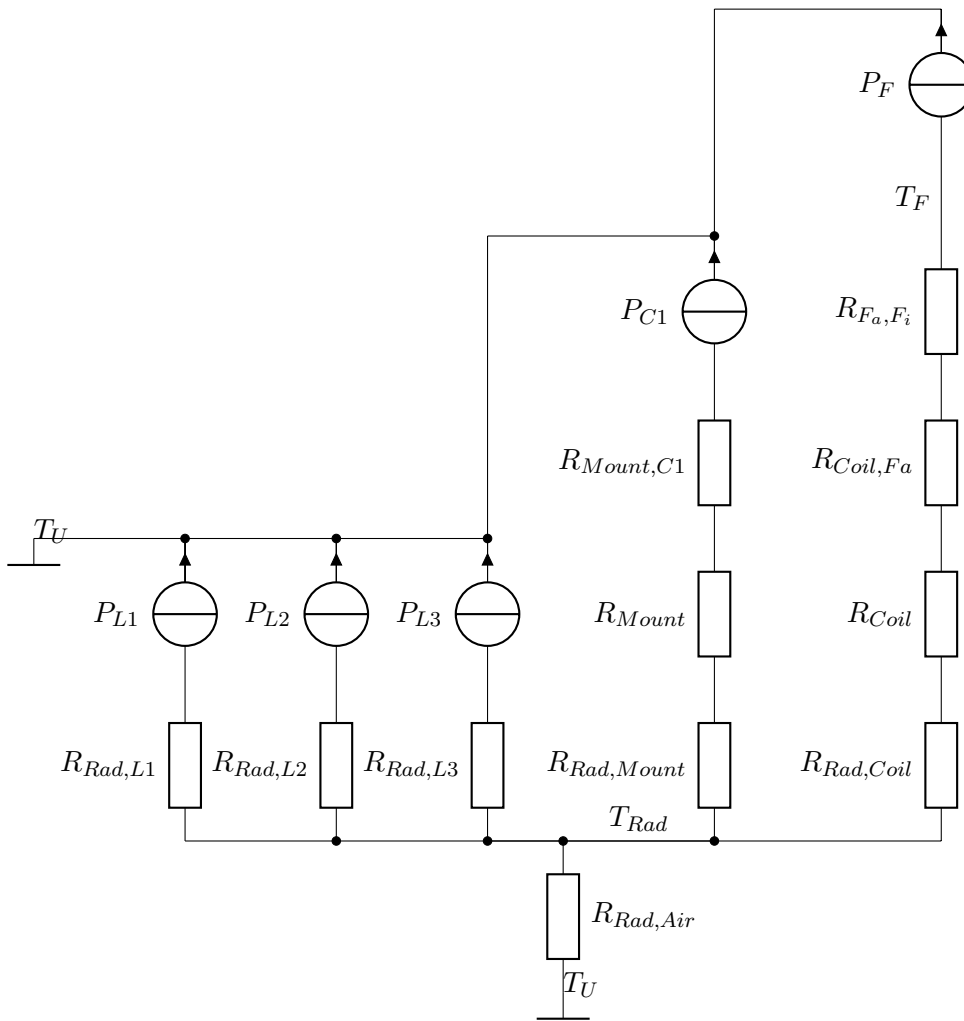


Figure A.3: Simplified thermic resistor network for the laser assembly

In this figure we omit all possible heat transfers between air and parts except between air and radiator ($R_{Rad,Air}$), as it makes the calculations easier and will be ignored in a future generation of the laser case. Furthermore as written in appendix A.7.2 we can omit the heat capacities after we are only interested in the steady state. The symbols in the network are described in table A.4.

P_F	Heat input power from the fiber
P_{L1}	Heat input power from laser $L1$
P_{L2}	Heat input power from laser $L2$
P_{L3}	Heat input power from laser $L3$
P_{C1}	Heat input power from fiber coupler $C1$
T_{Rad}	Temperature of the radiator
T_U	Ambient temperature
T_F	Temperature of the fiber
$R_{Rad,L1}$	Thermal resistance between laser $L1$ and the radiator
$R_{Rad,L2}$	Thermal resistance between laser $L2$ and the radiator
$R_{Rad,L3}$	Thermal resistance between laser $L3$ and the radiator
$R_{Rad,Mount}$	Thermal resistance between the coupler mount and the radiator
$R_{Mount,C1}$	Thermal resistance between the coupler $C1$ and the coupler mount
$R_{Rad,Coil}$	Thermal resistance between the coil and the radiator
$R_{Rad,Air}$	Thermal resistance between the radiator and the air
$R_{Coil,Fa}$	Thermal resistance between the coil and the outside of the fiber
$R_{Fa,Fi}$	Thermal resistance between the outside of the fiber and the inside of the fiber
R_{Coil}	Internal resistance of the aluminium coil
R_{Mount}	Internal resistance of the coupler mount

Table A.4: Network elements of figure A.3

First we have to calculate the heat transfer between the core of the fiber and the surface of the fiber. Based on the general formula for radiation transport

$$\dot{Q} = \frac{A\lambda\Delta T}{l} \quad (\text{A.5})$$

we get the formula for the fiber by A.133.

$$\dot{Q} = 2\pi \cdot \frac{\lambda \cdot (T_1 - T_2)}{\ln\left(\frac{r_2}{r_1}\right)} \quad (\text{A.6})$$

$$\Delta T = \frac{\dot{Q} \cdot \ln\left(\frac{r_2}{r_1}\right)}{2\pi \cdot \lambda} \quad (\text{A.7})$$

$$\begin{aligned} &= \frac{60\text{W} \cdot \ln\left(\frac{200\mu\text{m}}{180\mu\text{m}}\right)}{2\pi \cdot 0.2 \frac{\text{J}}{\text{m}\cdot\text{K}}} \\ &= 5.03^\circ \text{K} \end{aligned} \quad (\text{A.8})$$

Next we have to calculate the heat transfer in the aluminium coil. For that we have to define some variables first. Those are displayed in table A.5 first, and afterwards calculated.

A_B	Area of the connection surface between coil and radiator
A_Q	Area of the area where the heat-inducing fibers are mounted onto
S_a	Longest way the heat can go to reach the radiator
S_i	Shortest way the heat can go to reach the radiator
Z_Q	Height of the area which is covered with heat-inducing fibers
Z_S	Total height of the coil
R_S	Radius of the coil
\dot{Q}_F	Heat radiation current of the fiber

Table A.5: Symbols used for calculating the heat distribution in the coil

Thus we can calculate now the temperature difference in the coil:

$$A_B = 100^2 \cdot \pi \text{mm}^3 \quad (\text{A.9})$$

$$Z_Q = 10\text{mm} \quad (\text{A.10})$$

$$Z_S = 60\text{mm} \quad (\text{A.11})$$

$$R_S = 100\text{mm} \quad (\text{A.12})$$

$$A_Q = 2 \cdot R_S \cdot \pi \cdot Z_Q \quad (\text{A.13})$$

$$\begin{aligned} &= 2 \cdot 100\text{mm} \cdot \pi \cdot 10\text{mm} \\ &= 2000 \cdot \pi \text{mm}^2 \end{aligned} \quad (\text{A.14})$$

$$\dot{Q}_F = 60\text{W} \quad (\text{A.15})$$

$$S_a = 25\text{mm} + 2 \cdot R_S + Z_S \quad (\text{A.16})$$

$$= 285\text{mm} \quad (\text{A.17})$$

$$S_b = 25\text{mm} \quad (\text{A.18})$$

$$S_m = \frac{1}{2} (Z_S + R_S + (Z_S - Z_Q)) \quad (\text{A.19})$$

$$= \frac{1}{2} (S_a + S_b)$$

$$= 155\text{mm} \quad (\text{A.20})$$

$$A(S) = \frac{A_B - A_Q}{S_m} S + A_Q \quad (\text{A.21})$$

$$\dot{Q}_F = \frac{\lambda_{Al} \cdot (A_B - A_Q)}{S_m \cdot \ln\left(\frac{A_B}{A_Q}\right)} \cdot (T_Q - T_B) \text{ from A.118} \quad (\text{A.22})$$

\Rightarrow

$$60\text{W} = \frac{235 \frac{\text{W}}{\text{m}\cdot\text{K}} ((100^2 - 2000) \cdot \pi \text{mm}^2)}{155\text{mm} \cdot \ln\left(\frac{100^2 \cdot \pi \text{mm}^2}{2000 \cdot \pi \text{mm}^2}\right)} \cdot \Delta T \quad (\text{A.23})$$

$$\Delta T = 2.53^\circ\text{K} \quad (\text{A.24})$$

We obtain that the temperature difference between the position of the fiber on the aluminium and the surface mounted on the radiator is approximately 2.5°K if we assume a maximum loss of 60W from the fiber.

In order to calculate the heat transfer between the aluminium coil and the aluminium radiator we assume that the surface in between is coated in a heat transfer paste with $\lambda \approx 1.7 \frac{\text{W}}{\text{m}\cdot\text{K}}$ [64], and an average distance of $200\mu\text{m}$. Thus we can use formula A.25 and A.27 to calculate the thermal resistance between both bodies:

$$k_W = \frac{\lambda}{\delta} \quad (\text{A.25})$$

$$= \frac{1.7 \frac{\text{W}}{\text{m}\cdot\text{K}}}{200\mu\text{m}}$$

$$= 8500 \frac{\text{W}}{\text{m}^2 \cdot \text{K}} \quad (\text{A.26})$$

With that we can calculate the temperature difference:

$$\dot{Q} = k_W \cdot A_B \cdot \Delta T \quad (\text{A.27})$$

$$= 8500 \frac{\text{W}}{\text{m}^2 \cdot \text{K}} \cdot 100^2 \cdot \pi \text{mm}^2 \cdot \Delta T \quad (\text{A.28})$$

\Rightarrow

$$60\text{W} = 267.0 \cdot \Delta T \frac{\text{W}}{\text{K}} \quad (\text{A.29})$$

$$\Delta T = 0.225\text{K} \quad (\text{A.30})$$

In order to calculate the additional temperature differences between the three lasers L_1 , L_2 and L_3 , and the coupler C_1 we assume that all of them have the same connection area of $30 \cdot 13\text{mm}^2$ to the radiator plate. With that the temperature difference can be calculated:

$$\Delta T = \frac{P}{k_W \cdot A_B} \quad (\text{A.31})$$

$$\begin{aligned} &= \frac{10\text{W}}{8500 \frac{\text{W}}{\text{m}^2 \cdot \text{K}} \cdot 390\text{mm}^2} \text{ for the lasers} \\ &= 3.02^\circ\text{K} \text{ for the lasers} \end{aligned} \quad (\text{A.32})$$

For the coupler we have to do two steps, after we have a mount in between radiator and coupler. The first calculation step is between the mount and the coupler. For the calculation the fins are omitted to make it easier, therefore we can approach the problem the same way as the lasers on the radiator (with the same assumptions):

$$\Delta T = \frac{P}{k_W \cdot A_B} \quad (\text{A.33})$$

$$\begin{aligned} &= \frac{30\text{W}}{8500 \frac{\text{W}}{\text{m}^2 \cdot \text{K}} \cdot 720\text{mm}^2} \\ &= 4.90^\circ\text{K} \end{aligned} \quad (\text{A.34})$$

This is the temperature difference between the mount and the coupler itself, but still we have to calculate the heat flow through the connector and the heat transfer to the radiator. The first one can be done by using formula A.118:

$$\dot{Q} = \frac{\lambda \cdot (A_1 - A_2)}{s \cdot \ln\left(\frac{A_1}{A_2}\right)} \cdot (T_D - T_U)$$

Thus we get the equation system

$$A_1 = 720\text{mm}^2 \quad (\text{A.35})$$

$$A_2 = 2800\text{mm}^2 \quad (\text{A.36})$$

$$\lambda = 235 \frac{\text{W}}{\text{m} \cdot \text{K}} \quad (\text{A.37})$$

$$s \approx 50\text{mm} \quad (\text{A.38})$$

$$\dot{Q} = 30\text{W} \quad (\text{A.39})$$

$$\begin{aligned}
 &\Rightarrow \\
 \Delta T &= \frac{30\text{W} \cdot 50\text{mm} \cdot \ln\left(\frac{2800}{720}\right)}{235 \frac{\text{W}}{\text{m}\cdot\text{K}} \cdot (2080\text{mm})} \\
 &= 3.37 \cdot 10^{-3} \text{°K}
 \end{aligned} \tag{A.40}$$

The second part can be calculated by

$$\begin{aligned}
 \dot{Q} &= k_W \cdot A_B \cdot \Delta T \\
 &\Rightarrow \\
 \Delta T &= \frac{30\text{W}}{8500 \frac{\text{W}}{\text{m}^2\cdot\text{K}} \cdot 2800\text{mm}^2} \\
 &= 1.26 \text{°K}
 \end{aligned} \tag{A.42}$$

Finally we have to calculate the heat transfer between the cooler and the air flowing through. For that we need again to do some preparational equations:

$$\lambda_L = 0.0262 \frac{\text{W}}{\text{m} \cdot \text{K}} \tag{A.43}$$

$$S_k = 1\text{mm} \tag{A.44}$$

$$d_R = 1\text{mm} \tag{A.45}$$

$$\begin{aligned}
 A_W &= 325 \cdot 270\text{mm}^2 \\
 &= 87750\text{mm}^2
 \end{aligned} \tag{A.46}$$

$$t_k = 30\text{mm} \tag{A.47}$$

$$N_k = 125 \tag{A.48}$$

$$d_N = 2 \cdot S_k \tag{A.49}$$

$$= 2\text{mm} \tag{A.50}$$

$$\nu_L = 1.6 \cdot 10^{-5} \frac{\text{m}^2}{\text{s}} \tag{A.51}$$

$$\bar{u} = \frac{\dot{V}}{N_k \cdot t_k \cdot S_k} \tag{A.52}$$

$$\begin{aligned}
 &= \frac{0.05 \frac{\text{m}^3}{\text{s}}}{125 \cdot 30\text{mm} \cdot 1\text{mm}} \\
 &= 13.3 \frac{\text{m}}{\text{s}}
 \end{aligned} \tag{A.53}$$

$$L = 325\text{mm} \tag{A.54}$$

$$A_R = N_k \cdot L \cdot (2 \cdot t_k \cdot S_k) \tag{A.55}$$

$$= 2.48\text{m}^2 \tag{A.56}$$

$$Re = \frac{\bar{u} \cdot d_n}{\nu_L} \quad (\text{A.57})$$

$$= 1.667 \cdot 10^3 \quad (\text{A.58})$$

$$Nu = \sqrt[2]{4.364^2 + (0.018 \cdot Re^{0.8})^2} \quad (\text{A.59})$$

$$= 8.083 \quad (\text{A.60})$$

$$h_0 = \frac{\lambda_L \cdot Nu}{d_n} \quad (\text{A.61})$$

$$= 105.9 \frac{\text{W}}{\text{m}^2 \cdot \text{K}} \quad (\text{A.62})$$

$$\mu = \sqrt[2]{\frac{h_0 \cdot t_k^2}{\lambda_{Al}} \cdot \frac{2 \cdot L_k \left(1 + \frac{d_r}{L_k}\right)}{t_k \cdot S_k}} \quad (\text{A.63})$$

$$= 17.10 \quad (\text{A.64})$$

$$\varepsilon_\lambda = \frac{\tanh(\mu)}{\mu} \quad (\text{A.65})$$

$$= 58.5 \cdot 10^{-3} \quad (\text{A.66})$$

$$\dot{Q} = \varepsilon_\lambda \cdot h_0 \cdot N_k \cdot A_R \cdot \Delta T \quad (\text{A.67})$$

\Rightarrow

$$\Delta T = \frac{\dot{Q}}{\varepsilon_\lambda \cdot h_0 \cdot N_k \cdot A_R} \quad (\text{A.68})$$

$$= \frac{120\text{W}}{\varepsilon_\lambda \cdot h_0 \cdot N_k \cdot A_R} \quad (\text{A.69})$$

$$= 62.53 \cdot 10^{-3} \text{°K}$$

A.6.1.2 Air flow resistance and restrictions, calculation for the first design

Even if the results for the temperature are quite promising, they can only be used if the airflow is ideal. To calculate that we have to implement another resistance network.

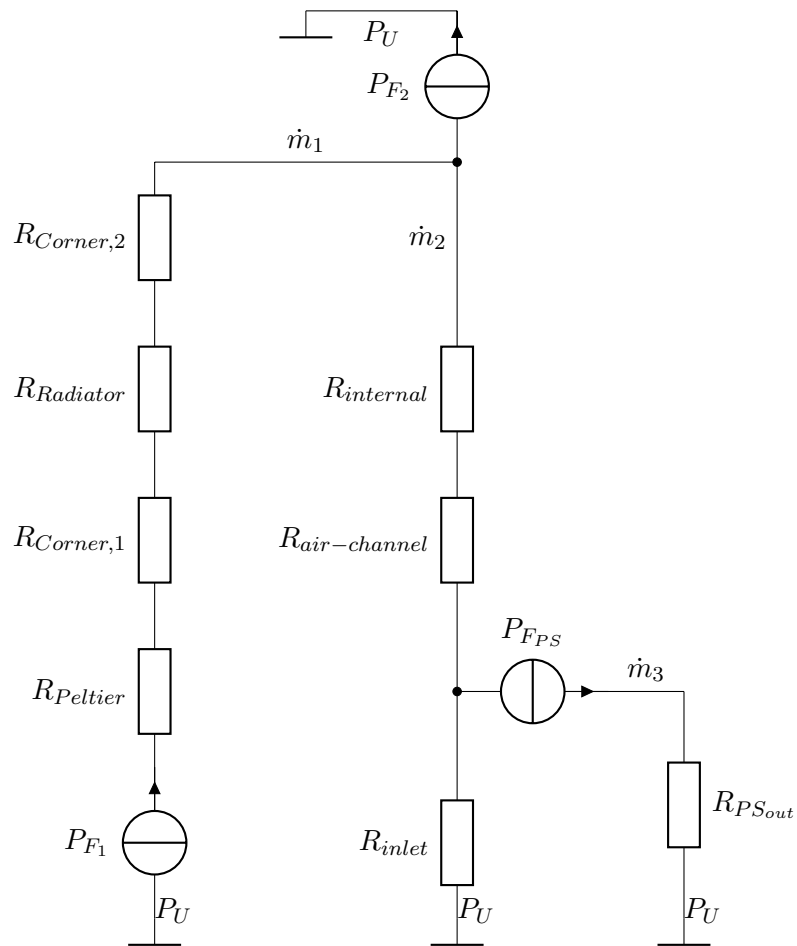


Figure A.4: Simplified air flow network for the laser assembly, symbol explanations in table A.6

P_U	Ambient pressure
P_{F_1}	Total pressure of inlet fans
P_{F_2}	Total pressure of outlet fans
P_{FPS}	Total pressure of power supply fan
$R_{Peltier}$	Flow resistance of the peltier radiator
$R_{Corner,1}$	Flow resistance of the first corner
$R_{Radiator}$	Flow resistance of the radiator
$R_{Corner,2}$	Flow resistance of the second corner
$R_{internal}$	Internal resistance of the laser assembly
R_{inlet}	Flow resistance of the air inlet to the air flow channel
$R_{PS_{out}}$	Flow resistance at the flow outlet of the power supply
$R_{air-channel}$	Flow resistance of the air channel inlet to the laser chamber
\dot{m}_1	Mass flow from backside inlet
\dot{m}_2	Mass flow through the air channel
\dot{m}_3	Mass flow through the power supply

Table A.6: Symbol explanation for figure A.4

Even if the resistors and pressure differences are shown in figure A.4, not all of them can be calculated due to missing data. That is (at the current state) $R_{internal}$ which only can be approximated, P_{FPS} and $R_{PS_{out}}$, after no data about the power supply cooling is available. For the fan P_{F_1} the data from the datasheet [65] is used. In this calculation the main concern is to provide the necessary amount of air flow to the main radiator. Thus the necessary air flow mass will be set to $0.05 \frac{\text{m}^3}{\text{s}}$, as it is the same value as used in the thermic calculation in equation A.69. The resistor $R_{Peltier}$ can be approximated by

$$\Delta p_t \approx \frac{\dot{m}^2}{2\rho \cdot A^2} \cdot 2 \quad [66] \quad (\text{A.70})$$

with $A = 10.0 \cdot 10^{-3} \text{m}^2$ as the air outlet from the radiators of the peltier cooling system. Thus we receive

$$\begin{aligned} \Delta p_t &\approx \frac{\left(0.05 \frac{\text{m}^3}{\text{s}} \cdot 1.29 \frac{\text{kg}}{\text{m}^3}\right)^2}{2\rho_L \cdot (10 \cdot 10^{-3} \text{m}^2)^2} \cdot 2 \\ &= 32.31 \frac{\text{kg}}{\text{s}^2 \cdot \text{m}} \end{aligned} \quad (\text{A.71})$$

For the first corner we approximate the pressure drop with

$$\Delta p_{C_1} \approx \frac{\dot{m}^2}{2 \cdot \rho \cdot A^2} \cdot 0.25 \quad (\text{A.72})$$

while leaving all other parameters constant:

$$\begin{aligned} \Delta p_{C_1} &\approx \frac{\left(0.05 \frac{\text{m}^3}{\text{s}} \cdot 1.29 \frac{\text{kg}}{\text{m}^3}\right)^2}{2 \rho_L \cdot (10 \cdot 10^{-3} \text{m}^2)^2} \cdot 0.25 \\ &= 4.04 \frac{\text{kg}}{\text{s}^2 \cdot \text{m}} \end{aligned} \quad (\text{A.73})$$

For the cooler itself we have to add up three different pressure drops: When the air enters the radiator fins, during the fins, and when the air leaves the fins again. Thus we get three formulas:

$$\Delta p_1 = \frac{\dot{m}_1^2}{2 \rho \cdot A_R^2} \cdot 0.25 \quad (\text{A.74})$$

$$= 28.72 \frac{\text{N}}{\text{m}^2} \quad (\text{A.75})$$

$$\Delta p_2 = \frac{\dot{m}_1^2}{2 \rho \cdot A_R^2} \cdot \frac{0.3164}{Re^{0.25}} \cdot \frac{L}{d_{nR}} \text{ refer to formula A.59} \quad (\text{A.76})$$

$$= 19.21 \frac{\text{N}}{\text{m}^2} \quad (\text{A.77})$$

$$\Delta p_3 = \frac{\dot{m}_1^2}{2 \rho \cdot A_R^2} \quad (\text{A.78})$$

$$= 114.86 \frac{\text{N}}{\text{m}^2} \quad (\text{A.79})$$

$$A_R = N_K \cdot s_K \cdot t_k \quad (\text{A.80})$$

$$\begin{aligned} &= 125 \cdot 1 \text{mm} \cdot 30 \text{mm} \\ &= 3.75 \cdot 10^{-3} \text{m}^2 \end{aligned} \quad (\text{A.81})$$

$$\nu = 15.11 \cdot 10^{-6} \frac{\text{m}^2}{\text{s}} \text{ (kinematic viscosity of air)} \quad (\text{A.82})$$

$$L = 325 \text{mm} \quad (\text{A.83})$$

$$d_n = \frac{4 \cdot A_R}{L} \text{ (hydraulic diameter)} \quad (\text{A.84})$$

$$= 46.15 \cdot 10^{-3} \text{m} \quad (\text{A.85})$$

$$Re = \frac{\bar{v} \cdot d_n}{\nu} \quad (\text{A.86})$$

$$= \frac{\frac{\dot{m}}{\rho \cdot A_R} \cdot d_n}{\nu} \quad (\text{A.87})$$

$$\begin{aligned}
&= \frac{\frac{0.05 \frac{\text{kg}}{\text{s}}}{1.29 \frac{\text{kg}}{\text{m}^3} \cdot 3.75 \cdot 10^{-3} \text{m}^2} \cdot 46.15 \cdot 10^{-3} \text{m}}{15.11 \cdot 10^{-6} \frac{\text{m}^2}{\text{s}}} \\
&= 31.52 \cdot 10^3
\end{aligned} \tag{A.88}$$

Therefore we get a total pressure difference Δp_R of

$$\Delta p_R = \Delta p_1 + \Delta p_2 + \Delta p_3 \tag{A.89}$$

$$= 162.79 \frac{\text{N}}{\text{m}^2} \tag{A.90}$$

Finally one has to calculate the last corner:

$$\begin{aligned}
\Delta p_{C_2} &\approx \frac{\left(0.05 \frac{\text{m}^3}{\text{s}} \cdot 1.29 \frac{\text{kg}}{\text{m}^3}\right)^2}{2 \rho_L \cdot (8.1 \cdot 10^{-3} \text{m}^2)^2} \cdot 0.25 \\
&= 6.15 \frac{\text{kg}}{\text{s}^2 \cdot \text{m}}
\end{aligned} \tag{A.91}$$

and a total pressure the fans at the backside inlet have to produce in order to get air in the necessary amount through the radiators:

$$\Delta p_{R_T} = 205.3 \frac{\text{N}}{\text{m}^2} \tag{A.92}$$

This shows that the fans which are currently in use are way to weak both in static pressure and in air mass flow, and have to be replaced with stronger fans. Now one still have to calculate R_{inlet} , $R_{air-channel}$ and $R_{internal}$. Here we can use the formulas

$$\Delta p_{inlet} = \frac{(\dot{m}_3 + \dot{m}_2)^2}{2 \rho \cdot A^2} \tag{A.93}$$

$$\Delta p_{air-channel+internal} = \frac{\dot{m}_2^2}{2 \rho \cdot A_g^2} \tag{A.94}$$

Based on the results we got from appendix A.6.1.1 we decided for the next developmentstage to close the air channel between the electronics module and the laser module, setting $\dot{m}_2 = 0$. This leaves us with

$$\Delta p_{inlet} = \frac{\dot{m}_3}{2 \rho \cdot A^2} \tag{A.95}$$

This calculation is unsolvable for us after we do not know the data of the fan used in the power supply. Therefore we also omit this calculation, and only need a ventilation system for the laser radiator with the data from table A.7.

Placement	Amount	Static pressure (total)	Airflow (total)
Front	3	$\geq 50\text{Pa}$	$\geq 0.05 \frac{\text{m}^3}{\text{s}}$
Back	2	175Pa	$0.05 \frac{\text{m}^3}{\text{s}}$

Table A.7: Fans needed for proper ventilation

A.6.1.3 Conclusion and results of the calculations

If comparing all thermal results while considering the airflow as ideal with the airflow used in appendix A.6.1.1 and static pressure calculated in appendix A.6.1.2, we get the following results:

Measurement point	ΔT compared to the air temperature at the inlet point [$^{\circ}\text{K}$]	Temperature at 35 $^{\circ}\text{C}$ inlet temperature ($[^{\circ}\text{C}]$)
After the peltier radiators	4.17	39.17
Heating of the radiator	4.23	39.23
Temperature of the lasers	7.25	42.25
Temperature of the coupler	10.40	45.40
Temperature of the coil	6.56	41.56
Temperature of the fiber mantle	≈ 1	<i>approx</i> 43
Average temperature of the fiber core	≈ 13	≈ 48

Table A.8: Thermal results for the laser case

Taking all the thermal maximum limits in account one can therefore say that at the maximum power the maximum air temperature at the inlet can be 60 °C to leave 5 °K as a buffer zone for the coupler to its maximum temperature of 75 °C. This is not the expected temperature range, but in the further generations it will be improved. Another possibility to improve the working temperature range is to add an radiator at the backside of the coupler mount. The necessary calculations are done in A.7.5 showing that alone the addition of an radiator could decrease the temperature of the coupler by approximately 1 °K. Nevertheless this decrease is unfortunately not enough for bringing the coupler down to an useful temperature. The biggest problem in this case is still the too small area used for transferring heat from the coupler to the mount. This problem can only be solved either by using a peltier element or by using both sides of the coupler for mounting it. Furthermore it can be noticed that if the problem with the high ΔT of both the small lasers and the coupler, for example by using peltier elements, the laser case is able to handle up to four times the current power input if the environmental temperature does not exceed 50 °C.

A.6.2 Improvements of the package

A.6.2.1 Laser module

In order to make the setup described in the first steps more stable and more durable it was decided to remove the peltier elements on the backside, and mount all lasers onto the main radiator. This decision was also influenced by the result from the thermal calculation of the radiator (eq. (A.69) and eq. (A.43)). Furthermore all lasers were placed onto peltier elements in order to increase their operating temperature range. The fiber is mounted onto a split aluminium coil, with an inner coil for the first laser stage and an outer coil for the second aluminium stage. The laser compartment is encased by an aluminium cage preventing water leakage from the outside, and keeping the fiber and lasers protected from environmental influences. The fiber and the wires are guided outside through a separated compartment in the aluminium cage, providing an extra cover from the outside. This compartment can be seen in fig. A.5.

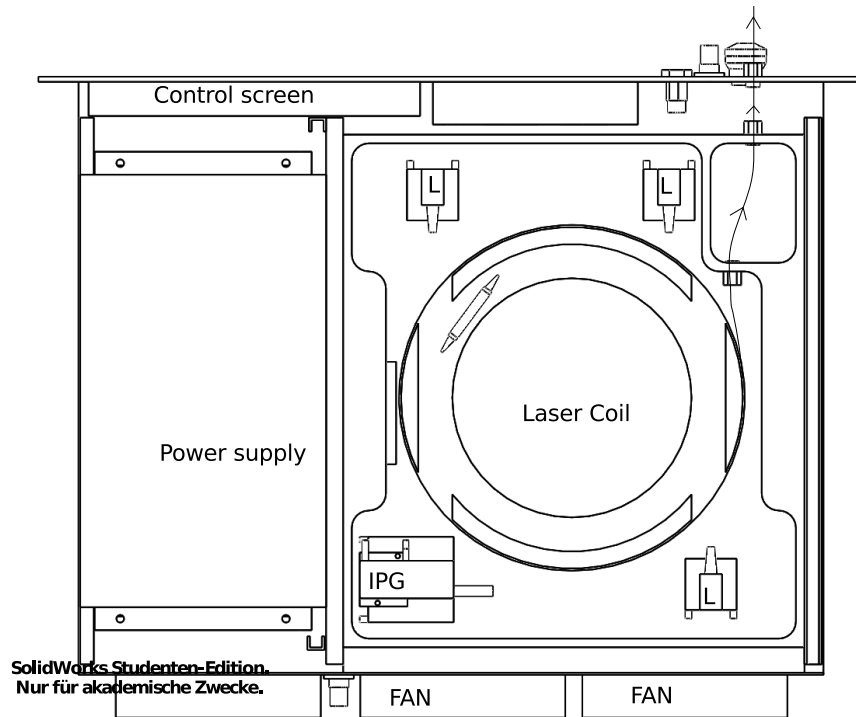


Figure A.5: Proposal for an improved build for the laser packaging, view including the laser compartment

In this figure the small lasers are marked with an **L**, while the pumping laser is marked with **IPG**. The laser fiber is marked with a black arrowed line. The module itself is displayed as a 3d-model in fig. A.6.

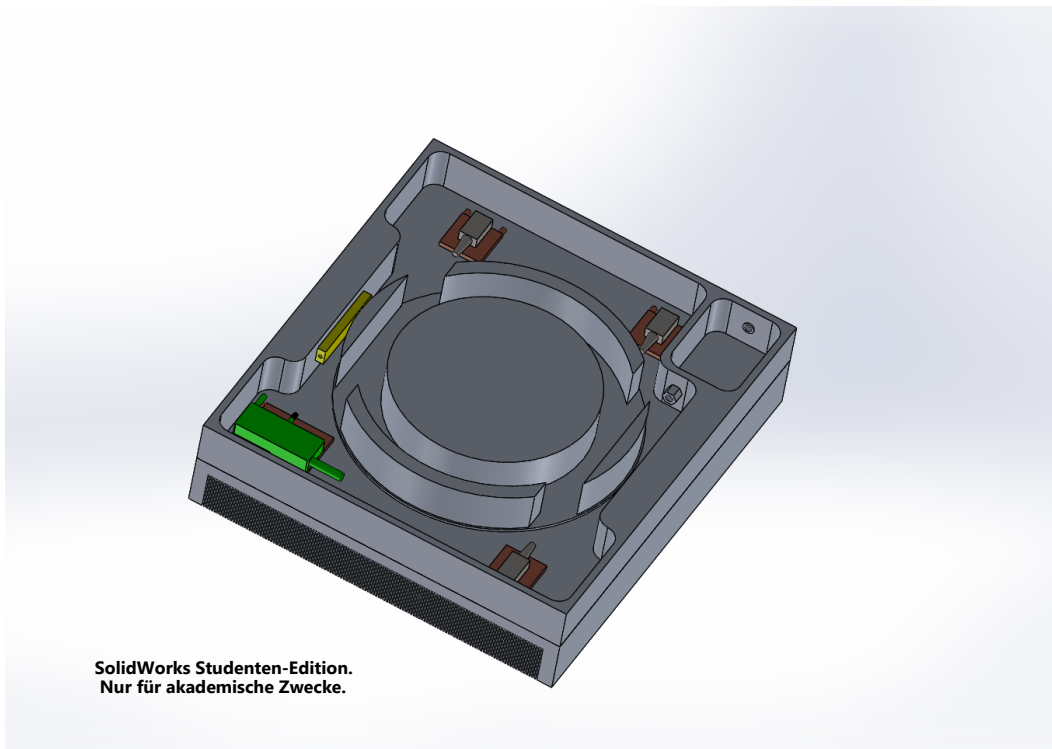


Figure A.6: Laser module assembly for the packaging, 2nd generation

In this picture the IPG-laser is marked green, while the initial lasers are marked brown. All lasers are mounted on peltier elements, also marked in brown. The coupler between the first and the second stage is coloured yellow in this drawing. Furthermore it has to be noticed that the fan placement is not final in this build.

A.6.2.2 Electronic module

As it can already be seen in fig. A.5 the power supplies for the laser are placed on one side. For this design two waterproof power supplies are used, both capable of delivering 600W at a voltage of 24V. While the first one is used for powering the lasers and electronics, the latter one will be used for powering the peltier elements. The electronics and the voltage converters used for regulating the operating voltage are placed in a compartment above the laser, which can be seen in fig. A.7.

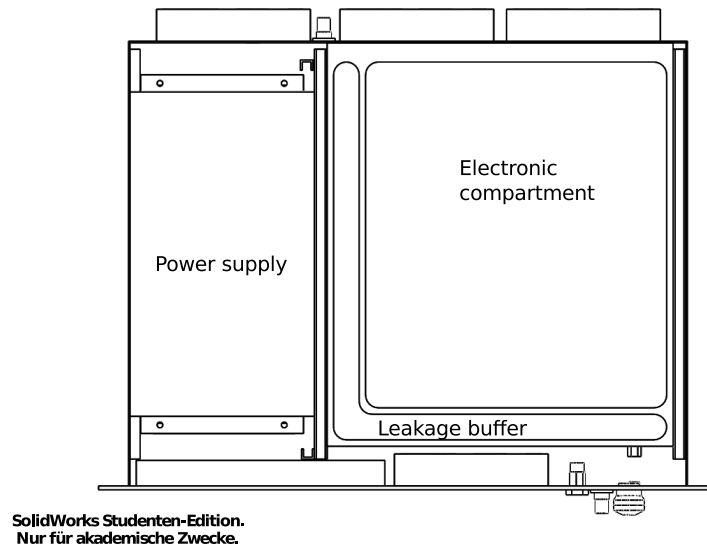


Figure A.7: Proposal for an improved build for the laser packaging, view including the electronic compartment

The electronics compartment is cut out of an aluminium block, providing $\approx 2.5\text{cm}$ space for the electronics, and sufficient cooling for the DC/DC-converters. This design can also be seen in fig. A.8.

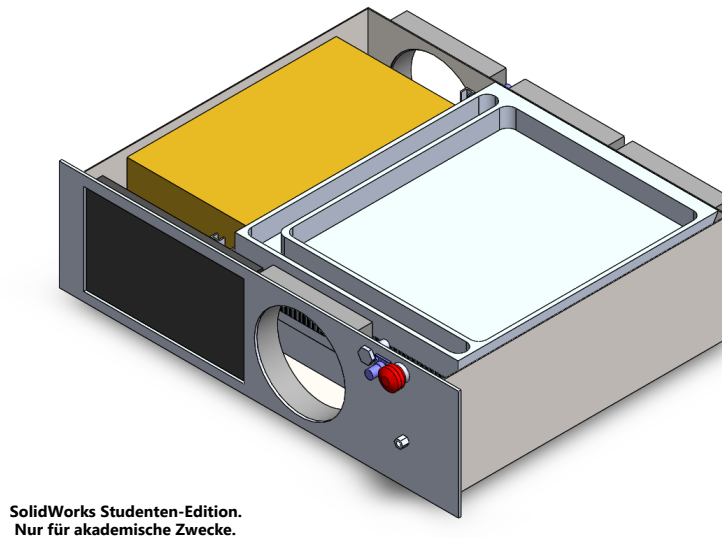


Figure A.8: 3d-model of the laser packaging, 2nd generation, including the electronic compartment

It is planned to use a raspberry pi as the main control station, but until now this is only a proposal. Nevertheless this would allow the user to use a range of different connection possibilities.

A.6.3 Further build options

In order to expand the possible packaging build options, a split design was also considered, housing a part of the laser in a separate package. This can be an advantage if the laser output has to be placed in an area without providing enough space for the controlling electronics and proper cooling. This design will consist out of a central coil, providing stability for the fiber, and a central cooling opening through the center of the coil. Due to the early design stage no models will be shown in this work, but it should be possible to mount either none, only the pump laser or all lasers directly onto the central coil. In each case the cooling system has to be fitted according to the emitted heat of the different lasers and fibers. One problem of having a hole with cooling fins in the centrum of the mounting cylinder is that it is quite difficult to manufacture. Nevertheless one possibility is the usage of a

3d-printer using laser-sintering. Furthermore they are not completely calculated with respect of cooling, but some approximations are shown in [67] and [68].

A.7 Derivation of the differential equation for the thermic network

A.7.1 General calculation

This derivation is based on [63], chapter 2.

If a homogeneous body gets heated by the heat power $P_1(t)$, the body gets the heat energy

$$\int_{t_1}^{t_2} P_1(t) dt \quad (\text{A.96})$$

within the time intervall $\Delta t = t_2 - t_1$. During this time the body gets heated by a temperature difference $\Delta\vartheta$ and stores a specific amount of heat

$$c_w \cdot m \Delta\vartheta \quad (\text{A.97})$$

Assuming the body was in equilibrium with the surrounding before the heating, according to the second law of thermodynamics it will emit a certain amount of heat energy in the same time Δt , based on its difference temperature $\vartheta = \vartheta_{body} - \vartheta_U$. The amount of energy can be calculated by

$$\int_{t_1}^{t_2} \alpha \cdot O_{eff} \vartheta(t) dt \quad (\text{A.98})$$

Those equations (A.96, A.97 and A.98) combined result in

$$\int_{t_1}^{t_2} P_1(t) dt = \int_{t_1}^{t_2} \alpha \cdot O_{eff} \cdot \vartheta(t) dt + c_w \cdot m \cdot \Delta\vartheta \quad (\text{A.99})$$

Following [63] we get by reducing $\Delta t \rightarrow dt$ and $\Delta\vartheta \rightarrow d\vartheta$ the differential equation

$$\frac{c_w \cdot m}{\alpha \cdot O_{eff}} \cdot \frac{d\vartheta}{dt} + \vartheta(t) = \frac{P_1(t)}{\alpha \cdot O_{eff}} \quad (\text{A.100})$$

To calculate this equation we can replace it with a electric replacement network which is displayed in figure A.9.

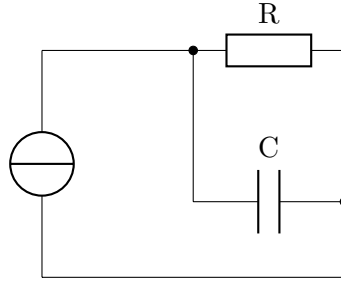


Figure A.9: Replacement circuit for simple thermal problem

The resulting differential equation of this circuit can be solved by the approach

$$R \cdot C \cdot \frac{d}{dt} u_1(t) + u_1(t) = R \cdot i_1(t) \quad (\text{A.101})$$

By comparing equation A.100 with equation A.101, we see that we can rewrite equation A.100 to

$$W_k \cdot C_k \cdot \frac{d}{dt} \vartheta(t) + \vartheta(t) = W_k \cdot P_1(t) \quad (\text{A.102})$$

This results in the following analogies:

$$\vartheta \leftrightarrow \text{electrical voltage} \quad (\text{A.103})$$

$$P_n(t) \leftrightarrow \text{electric current} \quad (\text{A.104})$$

$$W_k = \left(\frac{1}{\alpha \cdot O_{eff}} \right) \text{ (thermic resistance)} \quad (\text{A.105})$$

with α as heat transfer coefficient and
 O_{eff} as effective area

$$C_k = c_w \cdot m \text{ (heat capacity)} \quad (\text{A.106})$$

A.7.2 Steady state calculation

The equations above are useful if we are both interested into how the temperature of the different materials evolve, and in the result. If we are only interested into the result we can omit the capacitors, and take only a look at the resistor network:

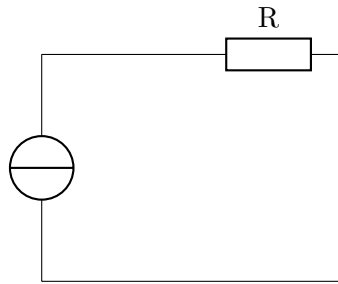


Figure A.10: Replacement circuit for simple thermal problem in steady state

This figure can now be solved by the much simpler equation

$$u_1(t) = R \cdot i_1(t) \quad (\text{A.107})$$

A.7.3 Derivation of the thermic formula

In order to calculate

$$\dot{Q} = k \cdot A \cdot (T_{\dot{Q}} - T_U) \quad (\text{A.108})$$

with a given λ , a given distance s and two given surfaces A_1 and A_2 , we have to do some assumptions first. We assume that the temperatures $T_{\dot{Q}}$ and T_U are constant, and the same is true for the thermal current

$$\dot{Q} = \dot{q}_{a_1} \cdot A_1 = \dot{q}_{a_2} \cdot A_2 \quad (\text{A.109})$$

Now the area depending on z , i.e. the position within the body, can be set as

$$A(z) = \frac{A_1 - A_2}{s} \cdot z + A_2 \quad (\text{A.110})$$

and combined with the formula for the temperature in dependance of the position within the body

$$\dot{Q} = -A(z) \cdot \lambda \frac{dT}{dz} \quad (\text{A.111})$$

\Rightarrow

$$\frac{dT}{dz} = -\frac{\dot{Q}}{A(z) \cdot \lambda} \quad (\text{A.112})$$

we obtain the equation series

$$\dot{Q} = k \cdot A_2 \cdot (T_{\dot{Q}} - T_U) \quad (\text{A.113})$$

$$\int_0^{T_{\dot{Q}} - T_U} dT = \int_0^s \frac{-\dot{Q}}{A(z) \cdot \lambda} dz \text{ from A.112} \quad (\text{A.114})$$

$$T_{\dot{Q}} - T_U = \frac{k \cdot A_1 \cdot (T_{\dot{Q}} - T_U)}{\lambda} \cdot \int_0^s \frac{dz}{\frac{A_1 - A_2}{s} \cdot z + A_2} \quad (\text{A.115})$$

$$T_{\dot{Q}} - T_U = k \cdot A_1 \cdot (T_{\dot{Q}} - T_U) \cdot \frac{s \cdot \ln\left(\frac{A_1}{A_2}\right)}{\lambda \cdot (A_1 - A_2)} \quad (\text{A.116})$$

$$\Rightarrow k \cdot A_1 = \frac{\lambda \cdot (A_1 - A_2)}{s \cdot \ln\left(\frac{A_1}{A_2}\right)} \quad (\text{A.117})$$

$$\Rightarrow \dot{Q} = \frac{\lambda \cdot (A_1 - A_2)}{s \cdot \ln\left(\frac{A_1}{A_2}\right)} \cdot (T_{\dot{Q}} - T_U) \quad (\text{A.118})$$

A.7.4 Derivation of heat flow from the inside to the outside of a fiber

Before we can start to derive the heat transfer formula for the fiber (which will be seen as ideal cylindrical shell in this case), we have to derive the formula for the shell itself. For that we start with the steady-state-condition for thermal heat flow:

$$\frac{d\dot{Q}(x)}{dx} = 0 \quad (\text{A.119})$$

$$\frac{d}{dx} \left(\lambda \cdot A \frac{dT}{dx} \right) = 0 \quad (\text{A.120})$$

For a cylinder this can be written as (if only depending on a single coordinate)

$$\lambda \frac{d}{dr} \left(A(r) \frac{dT}{dr} \right) = 0 \quad (\text{A.121})$$

or with the knowledge, that $A(r) = 2\pi \cdot r$:

$$\frac{d}{dr} \left(r \frac{dT}{dr} \right) = 0 \quad (\text{A.122})$$

Combined with the energy conservation law ($\dot{Q}_{in} = \dot{Q}_{out}$) we get

$$\frac{d\dot{Q}}{dr} = 0 \quad (\text{A.123})$$

The heat transfer rate per unit length is therefore given by

$$\dot{Q} = -\lambda \cdot 2\pi \cdot r \cdot \frac{dT}{dr} \quad (\text{A.124})$$

Now we can integrate equation A.122 once

$$r \frac{dT}{dr} = c \quad (\text{A.125})$$

with c as the integration constant. This equation A.125 can also be rewritten as

$$dT = c \cdot \frac{dr}{r} \quad (\text{A.126})$$

or in dimensionless variables

$$dT = c \cdot \frac{d\left(\frac{r}{r_1}\right)}{\left(\frac{r}{r_1}\right)} \quad (\text{A.127})$$

with r_1 as the inner radius. Integration of this leads to

$$T = c \cdot \ln\left(\frac{r}{r_1}\right) + d \quad (\text{A.128})$$

To find the constants c and d we have to find the boundary conditions. By setting $T = T_1$ at $r = r_1$ we obtain $d = T_1$. Setting $T = T_2$ at $r = r_2$ at the outer boundary we obtain

$$T_2 = c \cdot \ln\left(\frac{r_2}{r_1}\right) + T_1 \quad (\text{A.129})$$

$$c = \frac{T_2 - T_1}{\ln\left(\frac{r_2}{r_1}\right)} \quad (\text{A.130})$$

Thus we can get the temperature distribution by putting A.130 into A.128

$$T = (T_2 - T_1) \frac{\ln\left(\frac{r}{r_1}\right)}{\ln\left(\frac{r_2}{r_1}\right)} + T_1 \quad (\text{A.131})$$

or in the generalized form

$$\frac{T - T_1}{T_2 - T_1} = \frac{\ln\left(\frac{r}{r_1}\right)}{\ln\left(\frac{r_2}{r_1}\right)} \quad (\text{A.132})$$

Thus the heat transfer rate both for the cylindrical shell and the fiber is given by

$$\dot{Q} = 2\pi \cdot \frac{\lambda \cdot (T_1 - T_2)}{\ln\left(\frac{r_2}{r_1}\right)} \quad (\text{A.133})$$

A.7.5 Increasing the thermal situation for the coupler mount

In order to increase the thermal situation for the coupler one can either add fins directly on the mount or add a radiator to it. The first one is more effective, while the latter is cheaper and easier to fabricate. Therefore both situations shall be calculated. First the situation with the fins shall be calculated. For this situation it is assumed that the fins act like an additional radiator, but without temperature border between radiator and mount. Therefore we receive the following temperature network:

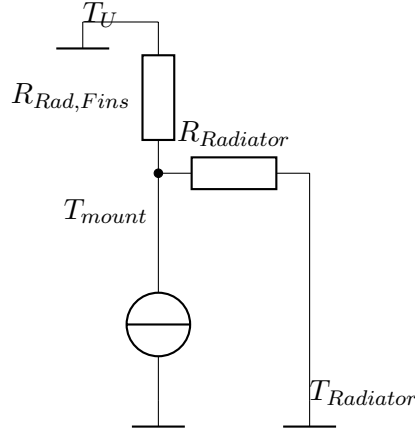


Figure A.11: Replacement circuit for coupler mount with attached fins

With this network one has to notice that $T_U < T_{Radiator}$, and therefore the heat flow is not equally distributed. The formula for $R_{Radiator}$ is already known from A.42, while for the first the formulas for the radiator (A.43 to A.69) are used.

$$\lambda_L = 0.0262 \frac{\text{W}}{\text{m} \cdot \text{K}} \quad (\text{A.134})$$

$$S_k = 1\text{mm} \quad (\text{A.135})$$

$$d_R = 1\text{mm} \quad (\text{A.136})$$

$$\begin{aligned} A_W &= 120 \cdot 59\text{mm}^2 \\ &= 7080\text{mm}^2 \end{aligned} \quad (\text{A.137})$$

$$t_k = 25\text{mm} \quad (\text{A.138})$$

$$N_k = 30 \quad (\text{A.139})$$

$$d_N = 2 \cdot S_k \quad (\text{A.140})$$

$$= 2\text{mm} \quad (\text{A.141})$$

$$\nu_L = 1.6 \cdot 10^{-5} \frac{\text{m}^2}{\text{s}} \quad (\text{A.142})$$

$$\bar{u} = \frac{\dot{V}}{N_k \cdot t_k \cdot S_k} \quad (\text{A.143})$$

$$= \frac{\dot{V}}{30 \cdot 25\text{mm} \cdot 1\text{mm}} \quad (\text{A.144})$$

$$= \frac{\dot{V}}{0.75 \cdot 10^{-3}} \frac{\text{m}}{\text{s}}$$

$$L = 120\text{mm} \quad (\text{A.145})$$

$$A_R = N_k \cdot L \cdot (2 \cdot t_k \cdot S_k) \quad (\text{A.146})$$

$$= 0.18\text{m}^2 \quad (\text{A.147})$$

$$Re(\dot{V}) = \frac{\bar{u} \cdot d_n}{\nu_L} \quad (\text{A.148})$$

$$= \dot{V} \cdot 166.7 \cdot 10^3 \quad (\text{A.149})$$

$$Nu(\dot{V}) = \sqrt[2]{4.364^2 + (0.018 \cdot Re(\dot{V})^{0.8})^2} \quad (\text{A.150})$$

$$h_0(\dot{V}) = \frac{\lambda_L \cdot Nu(\dot{V})}{d_n} \quad (\text{A.151})$$

$$\mu(\dot{V}) = \sqrt[2]{\frac{h_0(\dot{V}) \cdot t_k^2}{\lambda_{Al}} \cdot \frac{2 \cdot L_k \left(1 + \frac{d_r}{L_k}\right)}{t_k \cdot S_k}} \quad (\text{A.152})$$

$$\varepsilon_\lambda(\dot{V}) = \frac{\tanh(\mu(\dot{V}))}{\mu(\dot{V})} \quad (\text{A.153})$$

$$\dot{Q}(\dot{V}, \Delta T) = \varepsilon_\lambda(\dot{V}) \cdot h_0(\dot{V}) \cdot N_k \cdot A_R \cdot \Delta T \quad (\text{A.154})$$

Now we have the relations

$$\dot{Q}_T = \dot{Q}_{Radiator_2} + \dot{Q}_{Radiator} \quad (\text{A.155})$$

$$T_{mount} - T_U = \Delta T_{Radiator_2} \quad (\text{A.156})$$

$$= \Delta T_{Radiator} + \Delta T_{Mount, Rad} \quad (\text{A.157})$$

By putting all the equations together, we get

$$30\text{W} = \varepsilon_\lambda(\dot{V}) \cdot h_0(\dot{V}) \cdot N_k \cdot A_R \cdot \Delta T_{Radiator_2} + \quad (\text{A.158})$$

$$8500 \frac{\text{W}}{\text{m}^2 \cdot \text{K}} \cdot 2800\text{mm}^2 \cdot (\Delta T_{Mount, Rad} + \Delta T_{Radiator})$$

$$= \Delta T_{Radiator_2} \cdot \left(\varepsilon_\lambda(\dot{V}) \cdot h_0(\dot{V}) \cdot N_k \cdot A_R + 23.8 \frac{\text{W}}{\text{K}} \right) \quad (\text{A.159})$$

Now everything is depending on the available air flow. Some values have been calculated, and are displayed in figure A.12

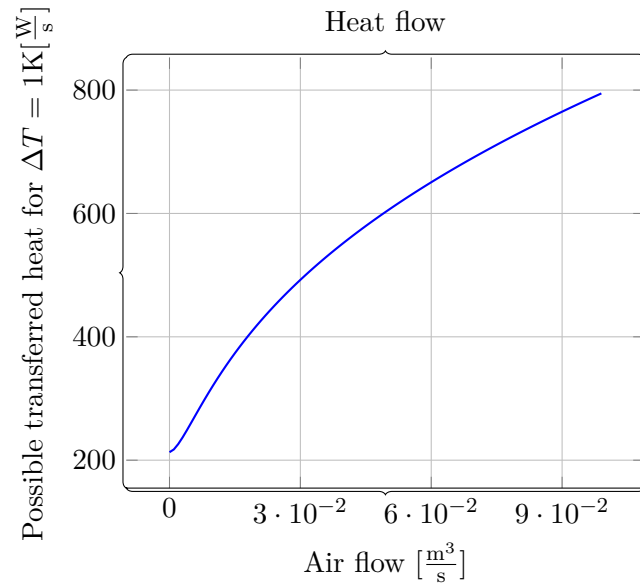


Figure A.12: Transported energy per time in dependance of the air flow

By rewriting A.159 we get

$$\Delta T_{Radiator_2} = \frac{30\text{W}}{\left(\varepsilon_\lambda(\dot{V}) \cdot h_0(\dot{V}) \cdot N_k \cdot A_R + 23.8 \frac{\text{W}}{\text{K}}\right)} \quad (\text{A.160})$$

This function can also be plotted using the values from figure A.12:

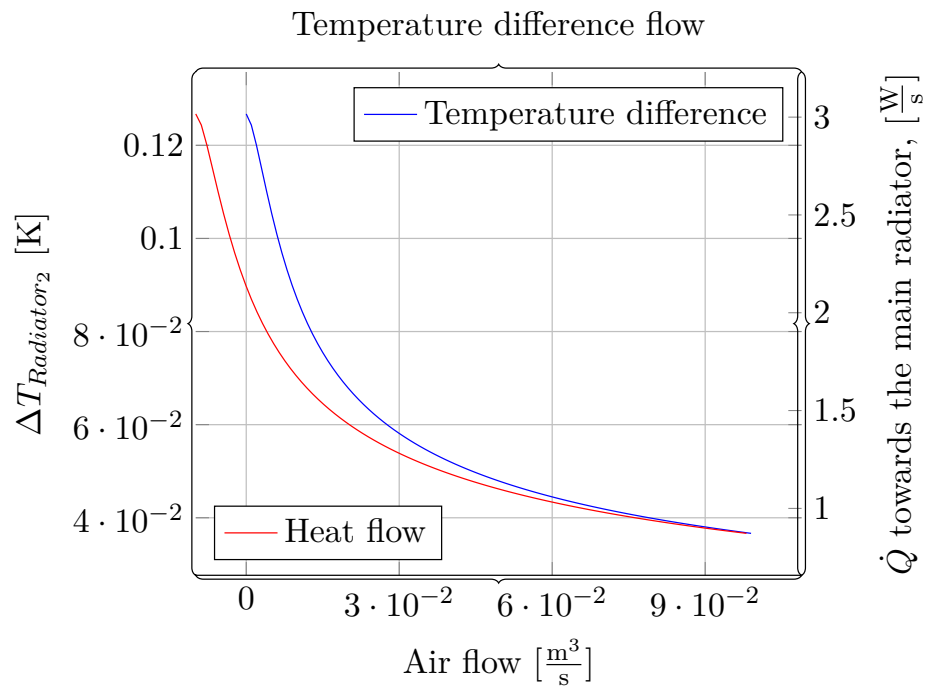


Figure A.13: Temperature difference of the radiator in comparison with the air flow

If we consider the second case, i.e. with an attached radiator, we can add another resistor in the network shown in figure A.11:

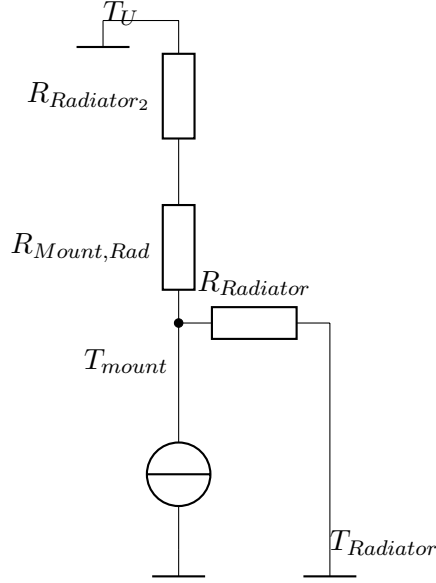


Figure A.14: Replacement circuit for coupler mount with attached radiator

While we can take the value for $R_{Radiator}$ from above (A.41) and for $R_{Radiator_2}$ (assuming it has the same value as calculated in A.154), we still have to calculate the temperature drop over the connection surface. We assume that the radiator is connected over the whole surface, i.e. $A = 120 \cdot 59\text{mm}^2$. Thus we receive the equations

$$\dot{Q} = k_W \cdot A \cdot \Delta T \quad (\text{A.161})$$

\Rightarrow

$$\begin{aligned} \dot{Q} &= 8500 \frac{\text{W}}{\text{m}^2 \cdot \text{K}} \cdot \Delta T_1 \cdot 7.08 \cdot 10^{-3} \text{m}^2 \\ &= 60.18 \frac{\text{W}}{\text{K}} \cdot \Delta T_1 \end{aligned} \quad (\text{A.162})$$

Here this equation can not solved yet, because we have to consider the relations

$$\dot{Q}_{Mount} = \dot{Q}_{Radiator_2} + \dot{Q}_{Radiator} \quad (\text{A.163})$$

$$T_{mount} - T_U = \Delta T_{Mount,Rad} + \Delta T_{Radiator_2} \quad (\text{A.164})$$

$$= \Delta T_{Radiator} + \Delta T_{Radiator,Air} \quad (\text{A.165})$$

This will result in the same result as shown in figure A.13 with a slight offset, after we are adding now a constant resistance. Therefore this calculation will not continued here.

A.7.6 Derivation of basic pressure difference function

In order to calculate the air flow through something it can be useful to know the pressure difference Δp between the pressure at the inlet p_1 and the pressure at the outlet p_2 of the body. To calculate this pressure difference one needs the resistance of the body towards the air flow:

$$\frac{\dot{m}_1^2}{\rho \cdot A} + p_1 \cdot A = \text{const.} \quad (\text{A.166})$$

\Rightarrow

$$\frac{\dot{m}_1^2}{\rho \cdot A} + p_1 \cdot A + F_R = \frac{\dot{m}_2^2}{\rho \cdot A} + p_2 \cdot A \quad (\text{A.167})$$

$$\frac{\dot{m}_1^2}{\rho \cdot A} = \frac{\dot{m}_2^2}{\rho \cdot A} \text{ because mass conservation} \quad (\text{A.168})$$

\Rightarrow

$$F_R = A \cdot (p_1 - p_2)$$

$$\frac{F_R}{A} = \Delta p_t \quad (\text{A.169})$$

This value can now be used in combination with the pressure curve from a fan which tells us the air flow volume the fan can produce with this amount of static pressure. Furthermore in [66] the resistance coefficients are given as ξ . The relation between ξ and the pressure difference is

$$\Delta p = \xi \rho \frac{v^2}{2} [\text{66}] \quad (\text{A.170})$$

$$\dot{m} = \rho \cdot A \cdot v \quad (\text{A.171})$$

$$v = \frac{\dot{m}}{\rho \cdot A} \quad (\text{A.172})$$

$$\Delta p = \xi \cdot \rho \frac{\dot{m}^2}{\rho^2 \cdot A^2 \cdot 2} \quad (\text{A.173})$$

$$\Delta p = \xi \cdot \frac{\dot{m}^2}{\rho \cdot A^2 \cdot 2} \quad (\text{A.174})$$

ξ is depending on the specific body, and is given in [66].

A.7.7 Calculation of the air flow velocity

In order to calculate the air velocity based on a fixed mass flow \dot{m} and a given area A we calculate

$$\dot{m} = \frac{dm}{dt} \quad (\text{A.175})$$

A.7 Derivation of the differential equation for the thermic network

$$= \frac{\varrho \cdot dV}{dt} \quad (\text{A.176})$$

$$= \varrho \cdot A \cdot \frac{dx}{dt} \quad (\text{A.177})$$

$$= \varrho \cdot A \cdot v \quad (\text{A.178})$$

\Rightarrow

$$v = \frac{\dot{m}}{\varrho \cdot A} \quad (\text{A.179})$$

A.8 Spectra

A.8.1 Supercontinuum spectrum, measurement

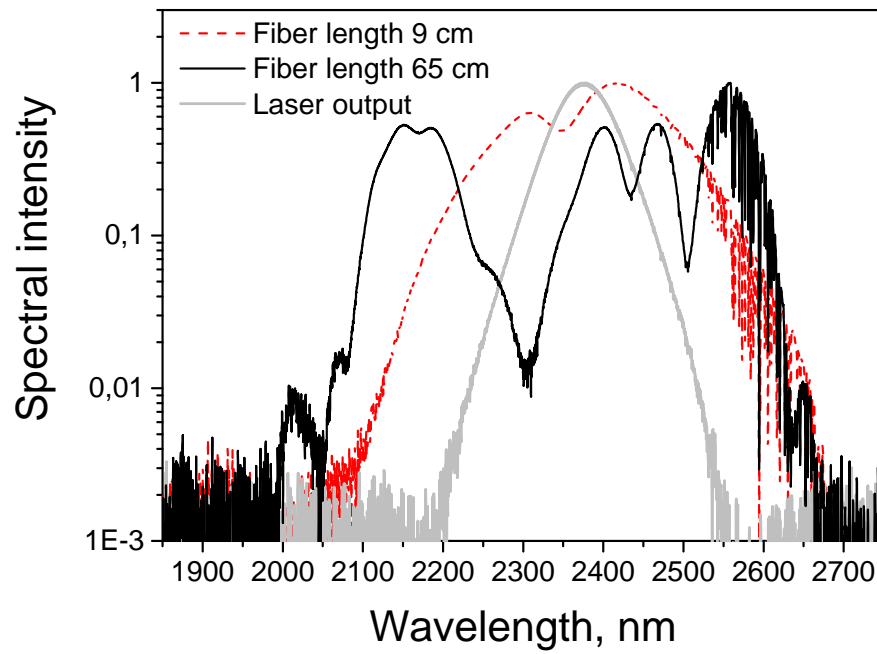


Figure A.15: Supercontinuum measurement of different fibers

A.9 Images

A.9.1 Cape I

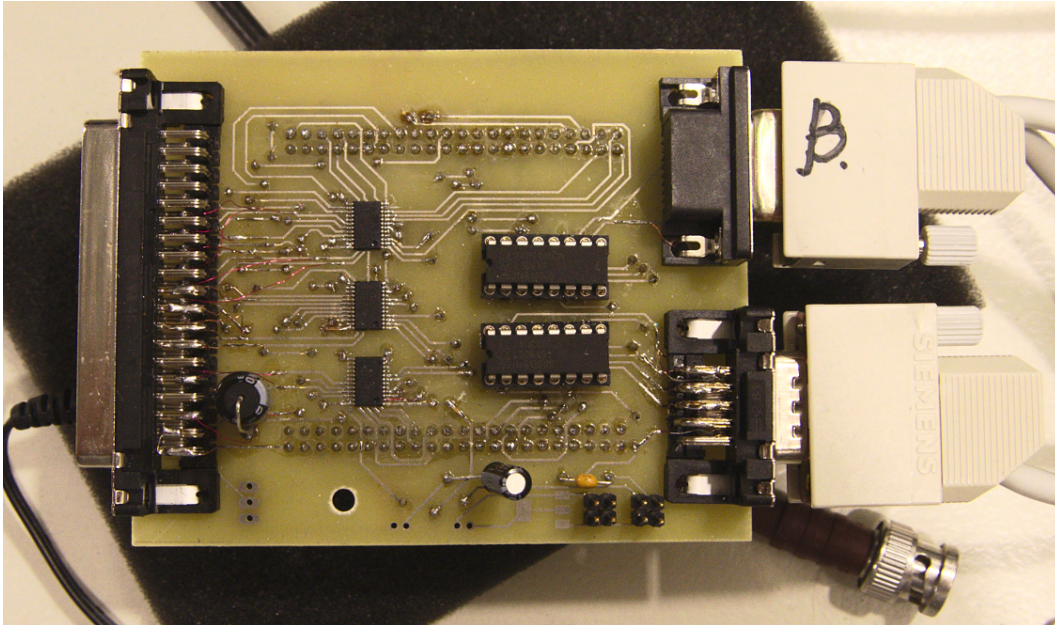


Figure A.16: Cape I, mounted onto the BeagleBone Black

A.9.2 Original ISA card

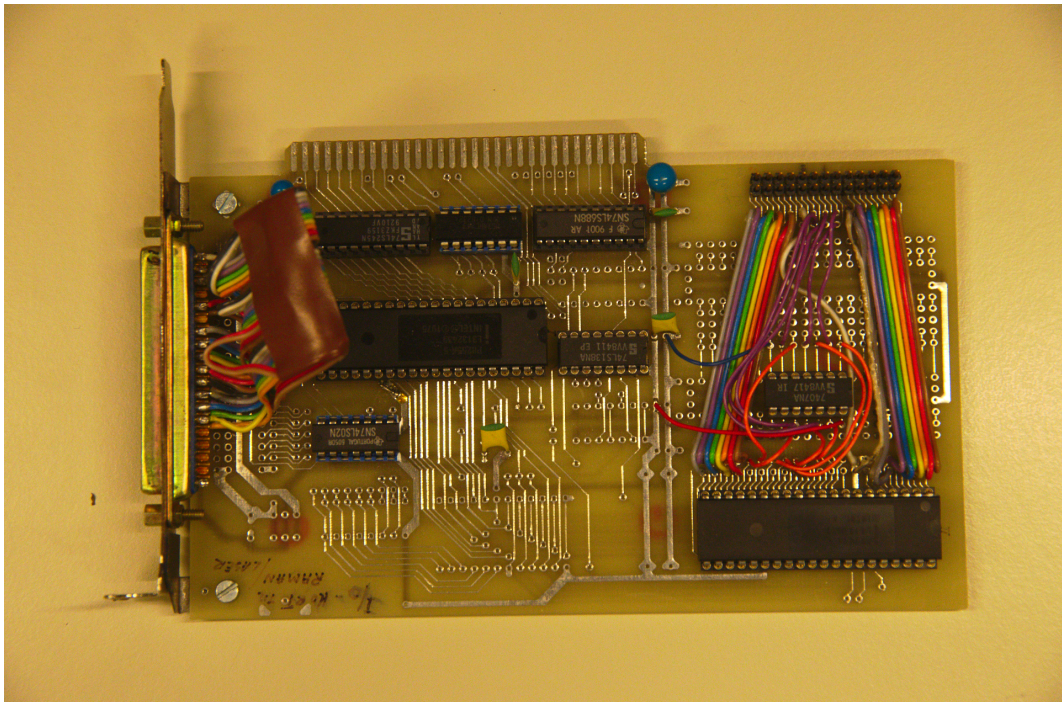


Figure A.17: Originally used ISA card

Bibliography

- [1] L. Brillouin. “Diffusion de la lumiere et des rayones X par un corps transparent homogene; influence del’agitation thermique”. In: *Annales de physique* 17 (1922), p. 88 (cit. on p. 5).
- [2] A. Smekal. “Zur Quantentheorie der Streuung und Dispersion”. German. In: *Zeitschrift für Physik* 32.1 (1925), pp. 241–244. ISSN: 0044-3328. DOI: 10.1007/BF01331666. URL: <http://dx.doi.org/10.1007/BF01331666> (cit. on p. 5).
- [3] C. V. Raman and F. R. S. “A new radiation”. In: *Indian Journal of Physics* 2 (1928), pp. 387–398 (cit. on p. 5).
- [4] S. P. S. Porto and D. L. Wood. “Ruby Optical Maser as a Raman Source”. In: *J. Opt. Soc. Am.* 52.3 (Mar. 1962), pp. 251–252. DOI: 10.1364/JOSA.52.000251. URL: <http://www.osapublishing.org/abstract.cfm?URI=josa-52-3-251> (cit. on p. 5).
- [5] R. H. Stolen and C. Lin. “Self-phase-modulation in silica optical fibers”. In: *Phys. Rev. A* 17 (4 Apr. 1978), pp. 1448–1453. DOI: 10.1103/PhysRevA.17.1448. URL: <http://link.aps.org/doi/10.1103/PhysRevA.17.1448> (cit. on p. 5).
- [6] R. H. Stolen, E. P. Ippen, and A. R. Tynes. “Raman Oscillation in Glass Optical Waveguide”. In: *Applied Physics Letters* 20.2 (1972), pp. 62–64. DOI: <http://dx.doi.org/10.1063/1.1654046>. URL: <http://scitation.aip.org/content/aip/journal/apl/20/2/10.1063/1.1654046> (cit. on p. 5).
- [7] G. Steinmeyer et al. “Frontiers in Ultrashort Pulse Generation: Pushing the Limits in Linear and Nonlinear Optics”. In: *Science* 286.5444 (1999), pp. 1507–1512. DOI: 10.1126/science.286.5444.1507. eprint: <http://www.sciencemag.org/content/286/5444/1507.full.pdf>. URL: <http://www.sciencemag.org/content/286/5444/1507.abstract> (cit. on p. 5).
- [8] R. H. Stolen, C. Lin, and R. K. Jain. “A time-dispersion-tuned fiber Raman oscillator”. In: *Applied Physics Letters* 30.7 (1977), pp. 340–342. DOI: <http://dx.doi.org/10.1063/1.89391>. URL: <http://scitation.aip.org/content/aip/journal/apl/30/7/10.1063/1.89391> (cit. on p. 5).

- [9] H. A. Haus, I. Sorokina, and E. Sorokin. “Raman-induced redshift of ultrashort mode-locked laser pulses”. In: *Journal of the Optical Society of America B* 15.1 (1998), p. 223 (cit. on p. 5).
- [10] V. L. Kalashnikov, E. Sorokin, and I. T. Sorokina. “Raman effects in the infrared supercontinuum generation in soft-glass PCFs”. In: *Journal of Applied Physics B* 87 (2007), pp. 37–44 (cit. on p. 5).
- [11] C. Lin and R. H. Stolen. “New nanosecond continuum for excited-state spectroscopy”. In: *Applied Physics Letters* 28, 216 (Feb. 1976), p. 216. DOI: 10.1063/1.88702 (cit. on p. 6).
- [12] R. H. Stolen, C. Lee, and R. K. Jain. “Development of the stimulated Raman spectrum in single-mode silica fibers”. In: *J. Opt. Soc. Am. B* 1.4 (Aug. 1984), pp. 652–657. DOI: 10.1364/JOSAB.1.000652. URL: <http://josab.osa.org/abstract.cfm?URI=josab-1-4-652> (cit. on p. 6).
- [13] A. Hasegawa and F. Tappert. “Transmission of stationary nonlinear optical pulses in dispersive dielectric fibers. I. Anomalous dispersion”. In: *Applied Physics Letters* 23.3 (1973), pp. 142–144. DOI: <http://dx.doi.org/10.1063/1.1654836>. URL: <http://scitation.aip.org/content/aip/journal/apl/23/3/10.1063/1.1654836> (cit. on p. 6).
- [14] L. F. Mollenauer et al. “Extreme picosecond pulse narrowing by means of soliton effect in single-mode optical fibers”. In: *Opt. Lett.* 8.5 (May 1983), pp. 289–291. DOI: 10.1364/OL.8.000289. URL: <http://ol.osa.org/abstract.cfm?URI=ol-8-5-289> (cit. on p. 6).
- [15] V. E. Zakharov and A. B. Shabat. “Exact theory of two-dimensional self-focussing and one-dimensional self-modulating waves in nonlinear media”. In: *Sov. Phys.-JETP (Engl. Transl.)* 34 (1972), p. 62 (cit. on p. 6).
- [16] J. Satsuma and N. Yajima. “B. Initial Value Problems of One-Dimensional Self-Modulation of Nonlinear Waves in Dispersive Media”. In: *Progress of Theoretical Physics Supplement* 55 (1974), pp. 284–306. DOI: 10.1143/PTPS.55.284. eprint: <http://ptps.oxfordjournals.org/content/55/284.full.pdf+html>. URL: <http://ptps.oxfordjournals.org/content/55/284.abstract> (cit. on p. 6).
- [17] J. M. Dudley, G. Genty, and S. Coen. “Supercontinuum generation in photonic crystal fiber”. In: *Rev. Mod. Phys.* 78 (4 Oct. 2006), pp. 1135–1184. DOI: 10.1103/RevModPhys.78.1135. URL: <http://link.aps.org/doi/10.1103/RevModPhys.78.1135> (cit. on pp. 6, 17).

-
- [18] G. P. Agrawal. “Preface”. In: *Nonlinear Fiber Optics (Fourth Edition)*. Ed. by G. P. Agrawal. Fourth Edition. Optics and Photonics. San Diego: Academic Press, 2006, pp. xv–xvi. DOI: <http://dx.doi.org/10.1016/B978-012369516-1/50000-5>. URL: <http://www.sciencedirect.com/science/article/pii/B9780123695161500005> (cit. on pp. 8, 9).
- [19] D. Hollenbeck and C. D. Cantrell. “Multiple-vibrational-mode model for fiber-optic Raman gain spectrum and response function”. In: *J. Opt. Soc. Am. B* 19.12 (Dec. 2002), pp. 2886–2892. DOI: 10.1364/JOSAB.19.002886. URL: <http://josab.osa.org/abstract.cfm?URI=josab-19-12-2886> (cit. on pp. 8, 22–24, 52).
- [20] G. P. Agrawal. “Chapter 2 - Pulse Propagation in Fibers”. In: *Nonlinear Fiber Optics (Fourth Edition)*. Ed. by G. P. Agrawal. Fourth Edition. Optics and Photonics. San Diego: Academic Press, 2006, pp. 25–50. DOI: <http://dx.doi.org/10.1016/B978-012369516-1/50002-9>. URL: <http://www.sciencedirect.com/science/article/pii/B9780123695161500029> (cit. on p. 9).
- [21] J. C. Travers, M. H. Frosz, and J. M. Dudley. “Nonlinear fibre optics overview”. In: *Supercontinuum Generation in Optical Fibers*. Ed. by J. M. Dudley and J. R. Taylor. Cambridge Books Online. Cambridge University Press, 2010, pp. 32–51. ISBN: 9780511750465. URL: <http://dx.doi.org/10.1017/CB09780511750465.004> (cit. on p. 9).
- [22] K. Rottwitt and P. Tidemand-Lichtenberg. *Nonlinear Optics: Principles and Applications*. Optical Sciences and Applications of Light. CRC Press, 2014. ISBN: 9781466565838. URL: <https://books.google.no/books?id=G1jSBQAAQBAJ> (cit. on p. 10).
- [23] V. Sigaev et al. “Raman and dielectric spectra of the glass and single crystal of Li₂Ge₇O₁₅ in the frequency range 3–1000 cm⁻¹: I. Comparison of the structures of the crystal and initial glass”. English. In: *Glass Physics and Chemistry* 32.3 (2006), pp. 296–303. ISSN: 1087-6596. DOI: 10.1134/S1087659606030072. URL: <http://dx.doi.org/10.1134/S1087659606030072> (cit. on p. 10).
- [24] J. Laegsgaard. “Mode profile dispersion in the generalised nonlinear Schrödinger equation”. In: *Opt. Express* 15.24 (Nov. 2007), pp. 16110–16123. DOI: 10.1364/OE.15.016110. URL: <http://www.opticsexpress.org/abstract.cfm?URI=oe-15-24-16110> (cit. on p. 10).
- [25] J. M. Dudley and J. R. Taylor. *Supercontinuum Generation in Optical Fibers*. Ed. by J. M. Dudley and J. R. Taylor. 1st ed. Cambridge University Press, 2010 (cit. on pp. 12, 15, 17, 26, 54).

- [26] A. Snyder and J. Love. *Optical Waveguide Theory*. Science paperbacks. Springer, 1983. ISBN: 9780412099502. URL: https://books.google.com/books?id=gIQB%5C_hzB0SMC (cit. on p. 12).
- [27] K. Okamoto. *Fundamentals of Optical Waveguides*. 2nd ed. Academic Press, 2006 (cit. on pp. 12, 13).
- [28] A. B. Fedotov et al. “Spectral compression of frequency-shifting solitons in a photonic-crystal fiber”. In: *Opt. Lett.* 34.5 (Mar. 2009), pp. 662–664. DOI: 10.1364/OL.34.000662. URL: <http://ol.osa.org/abstract.cfm?URI=ol-34-5-662> (cit. on p. 14).
- [29] G. P. Agrawal. “Chapter 5 - Optical Solitons”. In: *Nonlinear Fiber Optics (Fourth Edition)*. Ed. by G. P. Agrawal. Fourth Edition. Optics and Photonics. San Diego: Academic Press, 2006, pp. 120–176. DOI: <http://dx.doi.org/10.1016/B978-012369516-1/50005-4>. URL: <http://www.sciencedirect.com/science/article/pii/B9780123695161500054> (cit. on p. 16).
- [30] R. R. Alfano and S. L. Shapiro. “Emission in the Region 4000 to 7000 Å Via Four-Photon Coupling in Glass”. In: *Phys. Rev. Lett.* 24 (11 Mar. 1970), pp. 584–587. DOI: 10.1103/PhysRevLett.24.584. URL: <http://link.aps.org/doi/10.1103/PhysRevLett.24.584> (cit. on p. 16).
- [31] J. Hansryd et al. “Fiber-based optical parametric amplifiers and their applications”. In: *Selected Topics in Quantum Electronics, IEEE Journal of* 8.3 (May 2002), pp. 506–520. ISSN: 1077-260X. DOI: 10.1109/JSTQE.2002.1016354 (cit. on p. 17).
- [32] J. M. C. Boggio et al. “730-nm optical parametric conversion from near-to short-wave infrared band”. In: *Opt. Express* 16.8 (Apr. 2008), pp. 5435–5443. DOI: 10.1364/OE.16.005435. URL: <http://www.opticsexpress.org/abstract.cfm?URI=oe-16-8-5435> (cit. on p. 17).
- [33] W. H. Weber and R. Merlin, eds. *Raman Scattering in Materials Science*. Vol. 42. Springer-Verlag, 2000. DOI: 10.1007/978-3-662-04221-2 (cit. on p. 17).
- [34] C. Kittel. *Introduction to Solid State Physics*. 8th. New York: John Wiley & Sons, Inc., 2004 (cit. on pp. 18–20).
- [35] A. I. Chumakov et al. “Equivalence of the Boson Peak in Glasses to the Transverse Acoustic van Hove Singularity in Crystals”. In: *Phys. Rev. Lett.* 106 (22 May 2011), p. 225501. DOI: 10.1103/PhysRevLett.106.225501. URL: <http://link.aps.org/doi/10.1103/PhysRevLett.106.225501> (cit. on p. 19).

-
- [36] B. B. Laird and H. R. Schober. “Localized low-frequency vibrational modes in a simple model glass”. In: *Phys. Rev. Lett.* 66 (5 Feb. 1991), pp. 636–639. DOI: 10.1103/PhysRevLett.66.636. URL: <http://link.aps.org/doi/10.1103/PhysRevLett.66.636> (cit. on p. 19).
- [37] W. Schirmacher, G. Diezemann, and C. Ganter. “Harmonic Vibrational Excitations in Disordered Solids and the “Boson Peak””. In: *Phys. Rev. Lett.* 81 (1 July 1998), pp. 136–139. DOI: 10.1103/PhysRevLett.81.136. URL: <http://link.aps.org/doi/10.1103/PhysRevLett.81.136> (cit. on p. 19).
- [38] C. R. Brundle, C. A. Evans, and S. Wilson. *Encyclopedia of Materials Characterization*. Butterworth-Heinemann, 1992 (cit. on p. 19).
- [39] M. Cardona and G. Güntherodt. *Light Scattering in Solids*. Light Scattering in Solids Bd. 1. Springer-Verlag, 1975. ISBN: 9780387119137. URL: <https://books.google.com/books?id=MLVUNAEACAAJ> (cit. on pp. 20, 21).
- [40] W. Weber and R. Merlin. *Raman Scattering in Materials Science*. Springer Series in Materials Science. Springer Berlin Heidelberg, 2000. ISBN: 9783540672234. URL: <https://books.google.com/books?id=n19nicHCm08C> (cit. on p. 20).
- [41] R. Liboff. *Introductory Quantum Mechanics*. Addison-Wesley, 2003. ISBN: 9780805387148. URL: <https://books.google.com/books?id=oqZSQgAACAAJ> (cit. on p. 20).
- [42] K. Blow and D. Wood. “Theoretical description of transient stimulated Raman scattering in optical fibers”. In: *Quantum Electronics, IEEE Journal of* 25.12 (Dec. 1989), pp. 2665–2673. ISSN: 0018-9197. DOI: 10.1109/3.40655 (cit. on pp. 22, 24, 52).
- [43] R. H. Stolen et al. “Raman response function of silica-core fibers”. In: *J. Opt. Soc. Am. B* 6.6 (June 1989), pp. 1159–1166. DOI: 10.1364/JOSAB.6.001159. URL: <http://josab.osa.org/abstract.cfm?URI=josab-6-6-1159> (cit. on p. 22).
- [44] Q. Lin and G. P. Agrawal. “Raman response function for silica fibers”. In: *Opt. Lett.* 31.21 (Nov. 2006), pp. 3086–3088. DOI: 10.1364/OL.31.003086. URL: <http://ol.osa.org/abstract.cfm?URI=ol-31-21-3086> (cit. on pp. 22, 24, 26).
- [45] G. P. Agrawal. “Chapter 8 - Stimulated Raman Scattering”. In: *Nonlinear Fiber Optics (Fourth Edition)*. Ed. by G. P. Agrawal. Fourth Edition. Optics and Photonics. San Diego: Academic Press, 2006, pp. 274–328. DOI: <http://dx.doi.org/10.1016/B978-012369516-1/50008-X>. URL: <http://www.sciencedirect.com/science/article/pii/B978012369516150008X> (cit. on p. 25).

- [46] S. Balac and F. Mahé. “An embedded Split-Step method for solving the nonlinear Schrodinger equation in optics”. In: *Journal of Computational Physics* 280 (2015), pp. 295–305 (cit. on pp. 25, 62).
- [47] S. Balac and A. Fernandez. “Mathematical analysis of adaptive step-size techniques when solving the nonlinear Schrödinger equation for simulating light-wave propagation in optical fibers”. In: *HAL* (2014) (cit. on pp. 25, 62).
- [48] S. Balac and A. Fernandez. “Comparison of adaptive step-size control strategies for solving the Generalised Non-Linear Schrodinger Equation in optics by the Interaction Picture method”. In: *HAL* (2012) (cit. on pp. 25, 62).
- [49] online. URL: <http://scgbook.info/> (cit. on p. 25).
- [50] T. Hohage and F. Schmidt. *On the numerical solution of nonlinear Schrödinger type equations in fiber optics*. ZIB, 2002 (cit. on p. 27).
- [51] J. Hult. “A Fourth-Order Runge-Kutta in the Interaction Picture Method for Simulating Supercontinuum Generation in Optical Fibers”. In: *Lightwave Technology, Journal of* 25.12 (Dec. 2007), pp. 3770–3775. ISSN: 0733-8724. DOI: 10.1109/JLT.2007.909373 (cit. on p. 27).
- [52] A. Fernandez et al. “Numerical simulation of incoherent optical wave propagation in nonlinear fibers”. In: *The European Physical Journal Applied Physics* 64.02 (2013), p. 24506 (cit. on p. 28).
- [53] *BeagleBone Black Manual* (cit. on p. 30).
- [54] *BD 300 Manual* (cit. on p. 30).
- [55] S. Praver and R. J. Nemanich. “Raman spectroscopy of diamond and doped diamond”. In: *Philosophical Transactions of the Royal Society of London A: Mathematical, Physical and Engineering Sciences* 362.1824 (2004), pp. 2537–2565. ISSN: 1364-503X. DOI: 10.1098/rsta.2004.1451 (cit. on pp. 38, 39).
- [56] P. A. Temple and C. E. Hathaway. “Multiphonon Raman Spectrum of Silicon”. In: *Phys. Rev. B* 7 (8 Apr. 1973), pp. 3685–3697. DOI: 10.1103/PhysRevB.7.3685. URL: <http://link.aps.org/doi/10.1103/PhysRevB.7.3685> (cit. on p. 39).
- [57] D. Klimentov et al. “Broadband dispersion measurement of ZBLAN, germanate and silica fibers in MidIR”. In: *Journal of Lightwave Technology* 30.12 (2012), pp. 1943–1947 (cit. on p. 41).
- [58] URL: <http://www.ens-lyon.fr/LST/Raman/spectrum.php?nom=silica%20glass> (cit. on p. 47).

-
- [59] G. S. Henderson et al. “The structure of GeO₂–SiO₂ glasses and melts: A Raman spectroscopy study”. In: *Journal of Non-Crystalline Solids* 355.8 (2009), pp. 468–474. ISSN: 0022-3093. DOI: <http://dx.doi.org/10.1016/j.jnoncrysol.2009.01.024>. URL: <http://www.sciencedirect.com/science/article/pii/S0022309309000350> (cit. on p. 46).
- [60] *Python source code to GNLSE*. <https://github.com/xmhk/gnlse>. 2014 (cit. on p. 55).
- [61] C. Mahnke. “Optische Superkontinua in Glasfasern: Untersuchungen zu Mechanismen der Entstehung mit und ohne Rückkopplung”. PhD thesis. Universität Rostock, Sept. 2014. URL: <urn:nbn:de:gbv:28-diss2015-0082-7> (cit. on p. 55).
- [62] *Matlab source code to GNLSE RK4IP*. URL: <http://freeopticsproject.org/index.html> (cit. on p. 62).
- [63] B. Kipp. “Analytische Berechnung thermischer Vorgänge in permanentmagneterregten Synchronmaschinen”. PhD thesis. Helmut-Schmidt-Universität, Universität der Bundeswehr Hamburg, 2008 (cit. on pp. 98, 118).
- [64] *HTCP data sheet* (cit. on p. 104).
- [65] *Fan Data Sheet*. URL: <http://www.adda.com.tw/data/file/AG12025.pdf> (cit. on p. 109).
- [66] I. E. Idel’chick. *Handbook of hydraulic resistance*. Ed. by I. E. Idel’chick. 3rd ed. Begell House, 1996 (cit. on pp. 109, 128).
- [67] A. Islam and A. Mozumder. “Forced convection heat transfer performance of an internally finned tube”. In: *Journal of Mechanical Engineering* 40.1 (2009), pp. 54–62 (cit. on p. 118).
- [68] V. Jain. “Heat transfer and pressure drop in internally finned tubes”. MA thesis. School of graduate studies of the university of Ottawa, July 1977 (cit. on p. 118).
- [69] G. P. Agrawal. “Chapter 1 - Introduction”. In: *Nonlinear Fiber Optics (Fourth Edition)*. Ed. by G. P. Agrawal. Fourth Edition. Optics and Photonics. San Diego: Academic Press, 2006, pp. 1–24. DOI: <http://dx.doi.org/10.1016/B978-012369516-1/50001-7>. URL: <http://www.sciencedirect.com/science/article/pii/B9780123695161500017>.
- [70] G. P. Agrawal. “Chapter 6 - Polarization Effects”. In: *Nonlinear Fiber Optics (Fourth Edition)*. Ed. by G. P. Agrawal. Fourth Edition. Optics and Photonics. San Diego: Academic Press, 2006, pp. 177–225. DOI: <http://dx.doi.org/10.1016/B978-012369516-1/50006-6>. URL: <http://www.sciencedirect.com/science/article/pii/B9780123695161500066>.

- [71] G. P. Agrawal. “Chapter 7 - Cross-Phase Modulation”. In: *Nonlinear Fiber Optics (Fourth Edition)*. Ed. by G. P. Agrawal. Fourth Edition. Optics and Photonics. San Diego: Academic Press, 2006, pp. 226–273. DOI: <http://dx.doi.org/10.1016/B978-012369516-1/50007-8>. URL: <http://www.sciencedirect.com/science/article/pii/B9780123695161500078>.
- [72] G. P. Agrawal. “Chapter 9 - Stimulated Brillouin Scattering”. In: *Nonlinear Fiber Optics (Fourth Edition)*. Ed. by G. P. Agrawal. Fourth Edition. Optics and Photonics. San Diego: Academic Press, 2006, pp. 329–367. DOI: <http://dx.doi.org/10.1016/B978-012369516-1/50009-1>. URL: <http://www.sciencedirect.com/science/article/pii/B9780123695161500091>.
- [73] G. P. Agrawal. “Chapter 10 - Four-Wave Mixing”. In: *Nonlinear Fiber Optics (Fourth Edition)*. Ed. by G. P. Agrawal. Fourth Edition. Optics and Photonics. San Diego: Academic Press, 2006, pp. 368–423. DOI: <http://dx.doi.org/10.1016/B978-012369516-1/50010-8>. URL: <http://www.sciencedirect.com/science/article/pii/B9780123695161500108>.
- [74] G. P. Agrawal. “Chapter 11 - Highly Nonlinear Fibers”. In: *Nonlinear Fiber Optics (Fourth Edition)*. Ed. by G. P. Agrawal. Fourth Edition. Optics and Photonics. San Diego: Academic Press, 2006, pp. 424–452. DOI: <http://dx.doi.org/10.1016/B978-012369516-1/50011-X>. URL: <http://www.sciencedirect.com/science/article/pii/B978012369516150011X>.
- [75] G. P. Agrawal. “Chapter 12 - Novel Nonlinear Phenomena”. In: *Nonlinear Fiber Optics (Fourth Edition)*. Ed. by G. P. Agrawal. Fourth Edition. Optics and Photonics. San Diego: Academic Press, 2006, pp. 453–513. DOI: <http://dx.doi.org/10.1016/B978-012369516-1/50012-1>. URL: <http://www.sciencedirect.com/science/article/pii/B9780123695161500121>.
- [76] G. P. Agrawal. “Chapter 3 - Group-Velocity Dispersion”. In: *Nonlinear Fiber Optics (Fourth Edition)*. Ed. by G. P. Agrawal. Fourth Edition. Optics and Photonics. San Diego: Academic Press, 2006, pp. 51–78. DOI: <http://dx.doi.org/10.1016/B978-012369516-1/50003-0>. URL: <http://www.sciencedirect.com/science/article/pii/B9780123695161500030>.
- [77] G. P. Agrawal. “Chapter 4 - Self-Phase Modulation”. In: *Nonlinear Fiber Optics (Fourth Edition)*. Ed. by G. P. Agrawal. Fourth Edition. Optics and Photonics. San Diego: Academic Press, 2006, pp. 79–119. DOI: <http://dx.doi.org/10.1016/B978-012369516-1/50004-2>. URL: <http://www.sciencedirect.com/science/article/pii/B9780123695161500042>.
- [78] R. R. Alfano and S. L. Shapiro. “Observation of Self-Phase Modulation and Small-Scale Filaments in Crystals and Glasses”. In: *Phys. Rev. Lett.* 24 (11 Mar. 1970), pp. 592–594. DOI: [10.1103/PhysRevLett.24.592](https://doi.org/10.1103/PhysRevLett.24.592). URL: <http://link.aps.org/doi/10.1103/PhysRevLett.24.592>.

-
- [79] W. K. Bischel and M. J. Dyer. “Wavelength dependence of the absolute Raman gain coefficient for the Q(1) transition in H₂”. In: *Journal of the Optical Society of America B* 3.5 (May 1986).
- [80] L. de la Cruz May et al. “Raman gain calculation by Raman threshold study in telecom fibers”. In: *Proceedings of SPIE* 8011 (2011).
- [81] A. J. DeMaria, C. M. Ferrar, and G. E. D. Jr. “Mode Locking of a Nd³⁺-doped glass laser”. In: *Applied Physics Letters* 8.22 (1966).
- [82] J. M. Fini et al. “Distributed suppression of stimulated Raman scattering in an Yb-doped filter-fiber amplifier”. In: *Optics Letters* 31.17 (Sept. 2006).
- [83] Y. Fujii et al. “Sum-frequency light generation in optical fibers”. In: *Opt. Lett.* 5.2 (Feb. 1980), pp. 48–50. DOI: 10.1364/OL.5.000048. URL: <http://ol.osa.org/abstract.cfm?URI=ol-5-2-48>.
- [84] J. P. Gordon. “Theory of the soliton self-frequency shift”. In: *Optics Letters* 11.10 (Oct. 1986).
- [85] G. Gotter. *Erwärmung und Kühlung elektrischer Maschinen*. Springer-Verlag, 1954.
- [86] B. Gross and J. T. Manassah. “Supercontinuum in the anomalous group-velocity dispersion region”. In: *J. Opt. Soc. Am. B* 9.10 (Oct. 1992), pp. 1813–1818. DOI: 10.1364/JOSAB.9.001813. URL: <http://josab.osa.org/abstract.cfm?URI=josab-9-10-1813>.
- [87] H. A. Haus. “Parameter Ranges for CW passive Mode”. In: *IEEE Journal of Quantum Electronics* 12.3 (Mar. 1976).
- [88] J. Hu et al. “Maximizing the bandwidth of supercontinuum generation in As₂Se₃ chalcogenide fibers”. In: *Optics Express* 18.7 (Mar. 2010).
- [89] M. N. Islam. “Raman Amplifiers for Telecommunication”. In: *IEEE Journal of Selected Topics in Quantum Electronics* 8 (May 2002).
- [90] J. Jackson et al. “Estimation of peak Raman gain coefficients for Barium-Bismuth-Tellurite glasses from spontaneous Raman cross-section experiments”. In: *Optics Express* 17.11 (May 2009).
- [91] B. Jalali et al. “Raman-Based Silicon Photonics”. In: *IEEE Journal of Selected Topics in Quantum Electronics* 12 (May 2006).
- [92] Y. Kang. “Calculations and Measurements of Raman Gain Coefficients of Different Fiber Types”. MA thesis. Virginia Polytechnic Institute and State University, 2002.
- [93] R. Khakimov et al. “Numerical solver for supercontinuum generation in multimode optical fibers”. In: *Optics Express* 21.12 (June 2013).

- [94] B. Kibler, J. Dudley, and S. Coen. “Supercontinuum generation and nonlinear pulse propagation in photonic crystal fiber: influence of the frequency-dependent effective mode area”. English. In: *Applied Physics B* 81.2-3 (2005), pp. 337–342. ISSN: 0946-2171. DOI: 10.1007/s00340-005-1844-z. URL: <http://dx.doi.org/10.1007/s00340-005-1844-z>.
- [95] R. Kitamura, L. Pilon, and M. Jonasz. “Optical constants of silica glass from extreme ultraviolet to far infrared at near room temperature”. In: *Appl. Opt.* 46.33 (Nov. 2007), pp. 8118–8133. DOI: 10.1364/AO.46.008118. URL: <http://ao.osa.org/abstract.cfm?URI=ao-46-33-8118>.
- [96] C. Lin, V. T. Nguyen, and W. G. French. “Wideband near-I.R. continuum /0.7-2.1 microns/ generated in low-loss optical fibres”. In: *Electronics Letters* 14 (Dec. 1978), p. 822.
- [97] V. Malinovsky and A. Sokolov. “The nature of boson peak in Raman scattering in glasses”. In: *Solid State Communications* 57.9 (1986), pp. 757–761. ISSN: 0038-1098. DOI: [http://dx.doi.org/10.1016/0038-1098\(86\)90854-9](http://dx.doi.org/10.1016/0038-1098(86)90854-9). URL: <http://www.sciencedirect.com/science/article/pii/0038109886908549>.
- [98] M. Nakazawa and M. Tokuda. “Continuum Spectrum Generation in a Multimode Fiber Using Two Pump Beams at 1.3 μm Wavelength Region”. In: *Japanese Journal of Applied Physics* 22 (Apr. 1983), pp. L239–L241. DOI: 10.1143/JJAP.22.L239.
- [99] F. Poletti and P. Horak. “Description of ultrashort pulse propagation in multimode optical fibers”. In: *Journal of the Optical Society of America B: Optical Physics* 25.10 (Oct. 2008).
- [100] L. A. Rahn. “Time-resolved inverse Raman spectroscopy”. In: *Opt. Lett.* 7.2 (Feb. 1982), pp. 66–68. DOI: 10.1364/OL.7.000066. URL: <http://ol.osa.org/abstract.cfm?URI=ol-7-2-66>.
- [101] R. Richter. *Tip enhanced Raman Scattering*. Bachelorthesis. 2013.
- [102] L. Shaw et al. “IR supercontinuum generation in As-Se photonic crystal fiber”. In: *Optical Society of America* (2005).
- [103] I. T. Sorokina et al. “14-fs pulse generation in Kerr-lens mode-locked prismless Cr:LiSGaF and Cr:LiSAF lasers: observation of pulse self-frequency shift”. In: *Optics Letters* 22.22 (Nov. 1997).
- [104] R. Stolen et al. “Raman response function of silica-core fibers”. In: *Optical Society of America* 6.6 (June 1989).
- [105] O. Vanvincq et al. “Spontaneous and delayed nonlinear responses for the propagation of ultrashort solitons in optical fibers”. In: *Physical Review A: Atomic, Molecular, and Optical Physics* (2012).

- [106] X. Yan et al. “Raman transient response and enhanced soliton self-frequency shift in ZBLAN fiber”. In: *Journal of the Optical Society of America* 29.2 (Feb. 2012).

Independence statement

Hereby I confirm that I wrote this thesis on my own and without the usage of other materials than listed. All used resources are listed in the bibliography.

Trondheim,

Acknowledgements

I want to thank all persons which made it possible for me to write this thesis. Especially I want to thank **Prof. Irina Sorokina** for making it possible that I could write my thesis at the NTNU, and for supporting me in every other possible way.

I want to thank **my parents** and **my whole family** very much for supporting me in every possible way while I was here in Norway and wrote this thesis.

Furthermore I want to thank **Nikolai Tolstik** for supporting me with all physics-related questions and optic-related designs.

I also want to thank **Dmitry Klimentov** for supporting me with all problems related to fibers and fiber-lasers.

Likewise I want to thank **Prof. Reinhard Kienberger** for supervising my thesis for the TU München.

Additionally I want to thank **the electronic workshop** for the help with the electrical parts of my thesis, and especially **Jürgen Gaßner** and **Marc Lauter** for their support while designing the different capes for the Beaglebone.

Finally I want to thank all un-cited persons which helped me with my thesis. Without you it would not have been possible for me to do all experiments and calculations.